On the self-consistent response of tokamak microinstabilities to plasma profile evolution

Arkaprava Bokshi

Doctor of Philosophy

University of York
Physics

September 2016

Abstract

Operating with an edge transport barrier (ETB) is central to ITER's goal of attaining a fusion energy gain of ten. The evolution and stability of this ETB is governed through the interplay of MHD modes and microinstabilities. The ballooning formalism is a mathematical framework that can be utilised to understand the characteristics of these modes in the linear regime.

When applied to toroidal drift microinstabilities (e.g. ITG), the ballooning formalism predicts two distinct classes of global eigenmodes: the strongly growing Isolated Mode (IM) that exists under special conditions, and the relatively benign General Mode (GM) that is more generally accessible. Here we present findings from a new initial-value code, developed to study the dynamics of these linear branches in the presence of a time-evolving equilibrium toroidal flow-shear. The code has been further extended to incorporate the (quasi-linear) effect of intrinsic flow generated by these global structures on the modes themselves. The IM/GM dynamics could provide physical insights into understanding small-ELM regimes and intrinsic rotation - two unresolved physics issues that are of great significance to ITER.

Firstly, the IM is seen to form more rapidly than the GM. For our chosen fluid-ITG model, even though both structures are likely to form deep into the nonlinear regime, there is indication that close to marginal stability, these global modes might form much sooner to subsequently influence the nonlinear evolution. Secondly, in the presence of a critical flow-shear, a GM-IM-GM transition can take place to trigger a burst in the growth rate as the IM is accessed. These dynamics can occur on the right time-scale and form the basis of a new model for small-ELMs outlined in this work. Transient bursts are seen in the linear growth rate at high flow-shears, which may provide an alternative trigger for small-ELMs. Certain other seemingly robust features are reported, which could guide experimental efforts to test this theory. Finally, allowing for the feedback of the intrinsic flow on the mode structure, the IM seems to be a stable equilibrium when the external flow-shear is weak, whereas when strong equilibrium flow-shears dominate over the intrinsic flow, the GM solution is more likely. An approach to model the intrinsic flow profile from these global structures is suggested.

Contents

List of Tables

List of Figures

Acknowledgements

Foremost, I am grateful to my supervisor, Prof. Howard Wilson, for the opportunity to work with him, and for the continued patience (and occasional stick) while I was distracted. I am especially thankful for the many exciting areas and questions he has introduced me to, but more importantly, for teaching me how to think critically and carefully. I am extremely thankful to Dr. David Dickinson for his steady guidance. I consider him nothing short of my mentor. Sincere thanks are also due to Prof. Jack Connor and Dr. Colin Roach for their many comments that have helped refine this work. I am very thankful to Dr. Koki Imada for proof-reading this document and teaching me how to improve the presentation of my work. I must thank Prof. Thomas Krauss for the tough interrogations during our thesis advisory panel meetings. I think most of my research happened in the months leading up to those sessions!

My PhD would have been a lot less exciting without friends with whom I could discuss my work. Gaurav Dhariwal, Jonathan Skipp and Jarrod Leddy have been my first contact points every time I was stuck with a mathematical calculation, needed a physics insight, or had given up after wrestling with my code. They deserve a special mention. Of course, there are several other academic colleagues and friends who have frequently helped with my work over these years. I will endeavour to thank them personally.

Finally, my family, who I dedicate this thesis to: my father, for introducing me to fusion; my mother, for being my biggest source of encouragement; and my brother, who I am positive will produce a much better thesis than this in his chosen area.

Declaration

This work has not previously been presented for an award at this, or any other, University. All sources are acknowledged as References. The research was undertaken at the University of York under the supervision of Prof. H. R. Wilson, and appears in the following conference proceedings/journal:

(a) A. Bokshi, D. Dickinson, C. M. Roach and H. R. Wilson, *Response of toroidal drift modes to profile evolution: a small-ELM model?*, 42$^{\text{nd}}$ EPS Conference on Plasma Physics, Lisbon 2015 [1]

(b) A. Bokshi, J. W. Connor, D. Dickinson, C. M. Roach and H. R. Wilson, *The self-consistent response of linear microinstabilities to profile evolution*, 43$^{\text{rd}}$ EPS Conference on Plasma Physics, Leuven 2016 [2]

(c) A. Bokshi, D. Dickinson, C. M. Roach and H. R. Wilson, *The response of toroidal drift modes to profile evolution: a model for small-ELMs in tokamak plasmas?*, Plasma Phys. Control. Fusion **58** (2016), 075011 [3]

The analytical calculations in Chapter 6, Section 6.2 (including the subsections beginning with this labelling), have been performed by H. R. Wilson.

Chapter 1

Energy outlook

1.1 A rising need for energy and de-carbonisation

With the global energy demand projected to grow by 37% by 2040, in its World Energy Outlook 2014, the International Energy Agency (IEA) concludes that "the global energy system is in danger of falling short of the hopes and expectations placed upon it" [4]. In absolute terms, more than 0.5 billion people in sub-Saharan Africa alone could be living without access to electricity beyond 2040. While such figures paint a bleak scenario, some global energy trends are encouraging:

(a) Significant increase in the share of natural gas to the energy mix (as opposed to increased dependence on coal, which emits much more CO_2/BTU[1]) helped by, for example, new regulations in the United States limiting power sector emissions[2] and increasingly flexible global trade in liquefied natural gas offering protection against supply disruption [4, 7].

(b) Around 2035-40, the world's energy mix is projected to divide into four almost equal parts (oil, coal, gas and low-carbon sources; see Fig. 1.1) with renewables' (including biofuels) contribution rising steadily to 8% from the current 3% [6].

Despite this, fossil fuels are predicted to contribute about 81% of the energy produced in 2035. At this rate, the world would exhaust its 1000 gigatonnes CO_2 budget[3] by 2040 [4], putting itself on a path consistent with a long-term global temperature rise of 3.6 °C, well above the internationally agreed 2.0 °C pre-industrial level to avert the most severe implications of climate change [8]. With just over half this budget spent, we are already experiencing extreme weather events: sea levels have risen twice as fast between 1993-2010 than 1901-2010 and large-scale wildfires in the western US have

[1] Natural gas emits 117 pounds of CO_2 per million British thermal units (BTU) of energy, whereas coal emits around 216 pounds of CO_2 per million BTU [5] (1 BTU = 1055 Joules).

[2] The power sector is expected to account for a significant 47% of the total primary energy consumption in 2035 [6].

[3] The maximum amount of CO_2 that can be released into the atmosphere without exceeding a given temperature threshold.

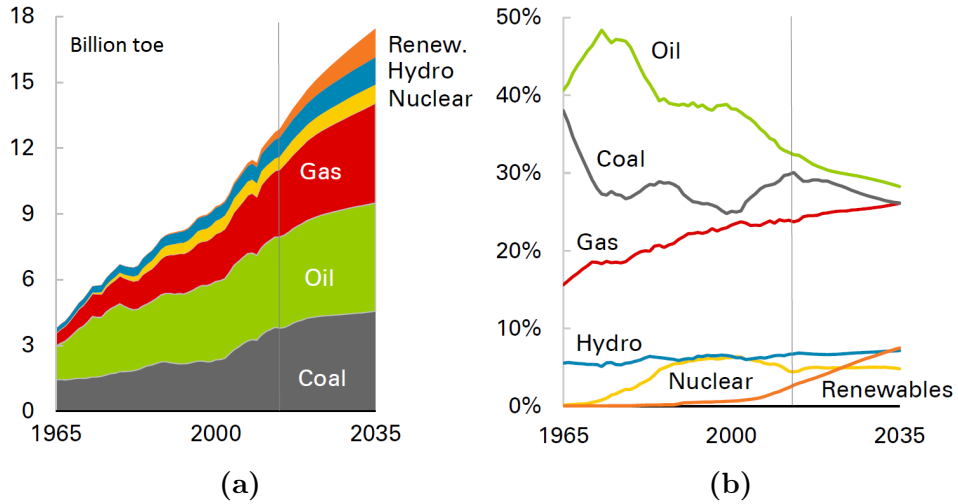

Figure 1.1: (a) Contribution of the various primary energy sources to the global energy consumption [1 billion toe ≃ 1.33 TWyear] and (b) their percentage share [6].

been seven times more frequent than they were in the 1970s [8]. There is substantial evidence linking temperature changes to CO_2 emissions (Fig. 1.2) and the cause of climate change to anthropogenic factors (Fig. 1.3). It is therefore of concern that despite its capacity to displace carbon-intensive baseload generation facilities[4], the *readily available* nuclear power technology has not been deployed more widely (see Nuclear trend in Fig. 1.1b) or been developed with more urgency. No doubt that other low-carbon sources are important to a long-term energy solution, but as will be discussed, a more central role is envisaged for fission energy in the short-medium term (~ decades).

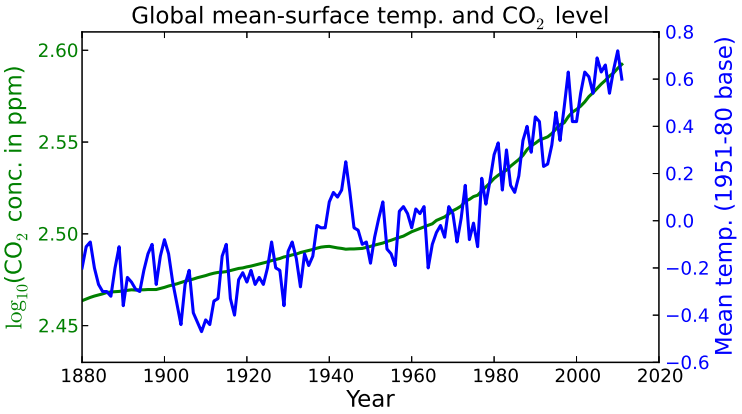

Figure 1.2: CO_2 concentration in atmosphere and global mean (ocean-land) temperature. (Data obtained from NASA GISS [10, 11].)

[4]Since 1971, nuclear power has avoided the release of an estimated 1.5 years of CO_2 at the current rate of 35.9 gigatonnes/year [9].

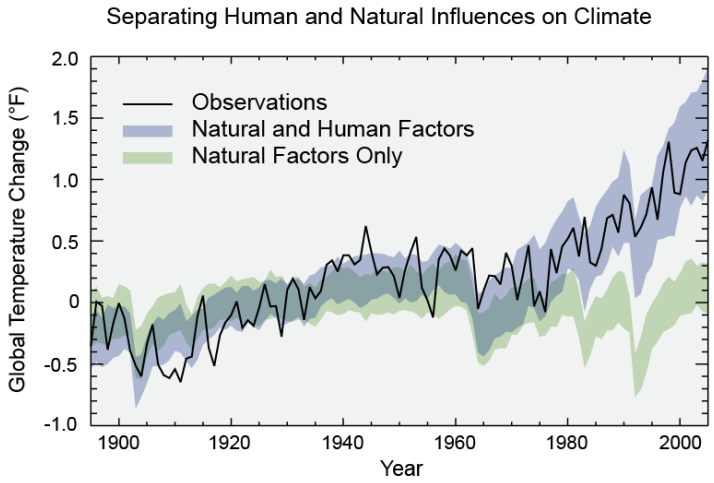

Figure 1.3: Models that only account for natural processes and not the greenhouse gases emitted by humans fail to explain the observed temperature change. (Adapted from [12] and courtesy of [13]; permission to publish obtained from the Nature Publishing Group.)

1.2 A case for fission energy

The need to decarbonise is immediate; global warming is only one of the concerns[5] - the adverse health effects and risks associated with energy production are issues that are oft-overlooked.

1.2.1 The energy deathprint

The 'energy deathprint' is defined as the number of people killed per kWh of energy produced, summarised in Table 1.1 for the various energy sources. For fossil fuels and biomass, upper respiratory distress due to carbon particulates is the main killer, whereas wind and solar are more associated with installation and maintenance related fatalities [15]. The figures for hydro-electricity are dominated by the failures of a few large dams, such as the Banqiao Reservoir Dam, which is estimated to have killed 171,000 people. Nuclear fission energy has the lowest deathprint, despite including the worst-case Chernobyl numbers and Fukushima projections. The UN Chernobyl Forum in its report [16] caps the number of *eventual* deaths among the most-exposed residents, evacuees and emergency workers to 4000. Compare this to the estimated 2.6-4.3 million annual deaths from indoor pollution due to burning solid fuels (e.g. coal, biomass in cooking) [17, 18, 19] or the 2.1-2.9 million deaths in 2013 alone from outdoor pollution [18, 19, 20].

[5]It is crucial that we note the efficacy and role of other greenhouse gases such as CH_4 and N_2O in causing global warming. Methane has a Global Warming Potential (GWP) of 25, i.e. will cause 25 times as much warming as an equivalent mass of CO_2 over a 100-year period, though only stays in the atmosphere 12 years, whereas nitrous-oxide has a GWP of 298 and stays in the atmosphere for 114 years. The agriculture sector is the major contributor to the release of methane (from livestock) and nitrous-oxide (from the use of synthetic fertilisers). These gases made up 11% and 6% of all U.S. greenhouse gas emissions from human activities in 2014 [14].

Table 1.1: Deaths per trillion kWh from various energy production sources (calculations and further references in [15]).

Energy source	Mortality rate (per Trillion kWhr)
Coal	170,000
Oil	36,000
Natural gas	4,000
Solar (rooftop)	440
Wind	150
Hydro	1,400
Nuclear	90

1.2.2 Scalability

In 20-30 years time, the global power demand allowing for a two-fold improvement in the overall efficiency is projected to be around 10-12 TW [6, 21]. Table 1.2 presents a possible low-carbon solution. Few things should be noted:

Table 1.2: A possible energy mix in 2040 (reproduced with permission from [21])

Low-carbon energy source	Peak power (TW)	Target power (TW)	Share in mix %	Required scaling from today
Wind	0.02	1.5	15	75
Solar PV	0.0013	0.5	5	384
Solar conc.	0.00046	0.5	5	1090
Hydro	0.32	1.6	16	5
Nuclear	0.4	4.9	49	12

(a) Biomass has not been kept central to this scenario due to questions surrounding its sustainability and the adverse health-effects of burning biofuels [22].

(b) Hydro will be close to its ~ 2 TW capacity [23].

(c) Wind, like hydro, is very geographically limited (the UK, for instance, has 40% of Europe's wind potential [23]).

(d) Both forms of solar need at least 2 orders of magnitude scale-up and, much like wind, needs the development of large-scale storage.

It is here that fission energy offers tremendous possibilities: it has a much lower deathprint than fossil-based energy (section 1.2.1), the fuel is abundant[6] and in principle can be rapidly scaled up. To exemplify, since its first operating nuclear power plant at Shippingport, the USA rapidly deployed fission power, providing

[6]Light Water Reactors (LWRs) could run for 230 years at today's consumption rate, uranium extracted from sea-water would allow 4000 years of operation at 10 TW [21] and Breeder Reactors operating in a closed fuel cycle could provide thousands of years worth of power with current output and reserves [24].

about 20% of the nation's energy within the first 30 years (supplying a steady 62.7 GW of power in 1990 - Fig. 1.4). This is possible due to the large power-densities intrinsic to nuclear reactions.

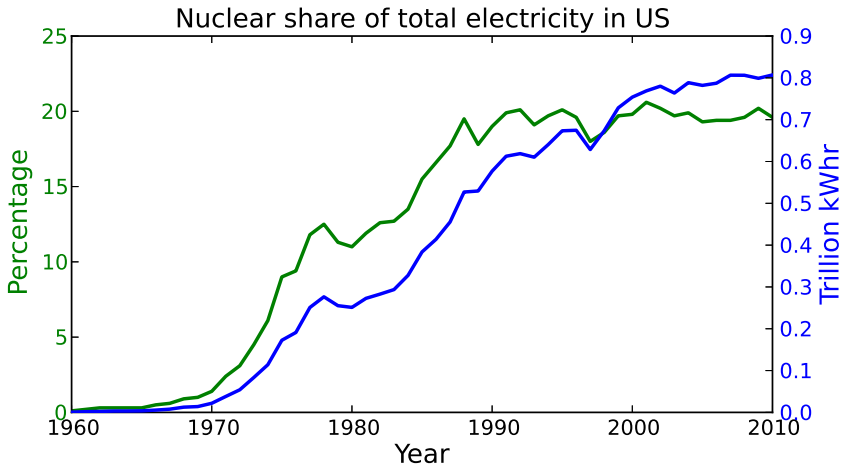

Figure 1.4: Nuclear energy's contribution to total electricity production in US. (Data derived from [25].)

1.3 Concerns with fission energy

It is imperative that we move towards a low-carbon energy mix, though the transition will be challenging with all known sources requiring a 10-1000× scale-up. Intermittent sources such as solar and wind would benefit hugely from the development of grid-scale storage or smart-grids. Carbon Capture and Storage (CCS)[7] and adopting more efficient energy technologies would no doubt help reduce the carbon footprint in our atmosphere. Ultimately, we need a diverse energy portfolio, of which fission needs to be an integral part. However, a number of factors seem to impede the acceptance of fission energy in the public and political domains:

(a) *Disagreement and uncertainty surrounding the true damage extent of nuclear accidents:* Greenpeace [26] for instance, challenges the UN Chernobyl Forum estimate of 4000 eventual deaths and puts this number around 100,000 – in close proximity with an earlier estimate in ref. [27].

(b) *Misrepresentation of information:* One blog [28] states that "A big risk is involved in operating a nuclear power plant. The energy that is generated can easily be harnessed to make devastating weapons, such as the nuclear bomb." While fission bombs exploit the same fundamental principle, not making clear the technological differences between civilian and military establishments puts nuclear power in bad light.

[7] CCS has the potential to sequester up to 85% of CO_2 from power stations and large industrial plants [23].

(c) *Concerns surrounding weapons proliferation:* While the fuel and by-product of LWRs - enriched Uranium and Plutonium - could potentially be used in nuclear weapons, ref. [29] notes that we lack robust knowledge to correlate civilian nuclear programmes with weapons acquisition. That said, and despite stringent checks and safeguards, IAEA does report a small number of incidents between 1993-2015 involving international trafficking of potentially weapons-usable material [30].

(d) *Radioactive high-level waste (HLW) management:* IAEA [31] notes that technologies and concepts to dispose spent-fuel and HLW *have been* developed but are yet to be implemented. Storing the waste on-site under water for 40-50 years allows the radiation level to drop below 0.1%, making it technically simpler to develop reprocessing and handling tools and retrieving the valuable Uranium before permanent disposal [32].

Fission energy clearly has many benefits over conventional non-renewables, but it seems to be losing support of people due to uncertainties over its connections with weapons programmes and concerns involving health-and-safety. In a global survey that followed Fukushima, 62% of citizens in 24 countries opposed the use of nuclear energy, with only India (61%), Poland (57%) and US (52%) receiving a majority public support [33]. Public faith in nuclear energy could conjure the political will necessary to attract more investment and relax the regulatory framework that is hindering the development of nuclear energy [34]. But with no indication that this trend will reverse, we must work towards harnessing an energy source that can deliver clean, safe, abundant and rapidly scalable energy: nuclear fusion.

1.4 Nuclear fusion

Nuclear fusion in nature occurs at the cores of stars: light nuclei like hydrogen collide and fuse into heavier nuclei, releasing tremendous amounts of energy in the process. The first terrestrial reactors envisage fusing Deuterium (D) and Tritium (T) to release a neutron (n) and 'fusion alpha' i.e. Helium (He):

$$ {}^{2}_{1}\mathrm{D} + {}^{3}_{1}\mathrm{T} \longrightarrow {}^{4}_{2}\mathrm{He} + {}^{1}_{0}\mathrm{n} + 17.6 \ \mathrm{MeV} \, . \tag{1.1} $$

This reaction requires typical temperatures of 10-20 KeV, but is still the simplest to realise among all possible fusion reactions [35]. Deuterium can easily be extracted from water and tritium can be produced in-situ[8] when a fusion-generated neutron

[8]Tritium decays with a half-life of 12.3 years and is therefore only found naturally in trace amounts.

interacts with the Lithium (Li) blanket surrounding the D-T reaction chamber:

$$^{6}_{3}\mathrm{Li} + ^{1}_{0}\mathrm{n} \longrightarrow ^{3}_{1}\mathrm{T} + ^{4}_{2}\mathrm{He} + 4.8\,\mathrm{MeV}\ , \tag{1.2}$$

$$^{7}_{3}\mathrm{Li} + ^{1}_{0}\mathrm{n} \longrightarrow ^{3}_{1}\mathrm{T} + ^{4}_{2}\mathrm{He} + ^{1}_{0}\mathrm{n}\ (\mathrm{slow})\ . \tag{1.3}$$

The neutron reaction with the more abundant $^{7}_{3}$Li isotope (92.5%) is endothermic, but yields a (slow) neutron. This additional neutron can be captured by another Li atom to produce more tritium than is being consumed. Nuclear fusion has several advantages:

(a) *Abundant:* It is estimated that 9.3 g of D (contained in a typical shower) and 0.25 g of Li is enough to meet an individual's annual energy demand [36]. Water is practically inexhaustible and based on the US Geological Survey data [37], the current economically recoverable Li reserves would be sufficient to power fusion reactors for ~ 9000 years (at 1500 tons consumed annually for fusion, which is 5% of the global production). By switching to D-D reactions in the future, fusion can supply energy for billions of years.

(b) *Clean:* Fusion does not emit any greenhouse gas; its major by-product is He, an inert, non-toxic gas.

(c) *No long-lived radioactive waste:* The only waste would be from the fusion-born neutrons activating the surrounding structural components. But these components will be safe to recycle/dispose within a 100 year period [38]. Choice of structural materials [39] and optimising the neutron fluence (by tuning the ^{7}Li/^{6}Li mix) could further reduce this period.

(d) *Safe:* Unlike in fission reactors, whereby a chain-reaction needs to be controlled, a fusion system like a tokamak needs to be continuously heated and maintained under optimum conditions. These requirements (discussed in more detail in section 2.3) further restrict the amount of fuel at any time inside the reactor with a volume of several 100 m^3 to weigh about a postage stamp [38]. Any deviation from normal operation would rapidly cool the reactor core and stop the process.

(e) *Low risk of proliferation:* Fusion does not employ fissile materials. Reference [40] further concludes that with appropriate safeguards like in fission, proliferation risks associated with fusion are much lower than fission and gives the global community the added option of safely disabling the plant without concerns of radioactive material dispersal.

1.5 Summary

Energy consumption and economic growth (and development) are tied [41]. But reliance on fossil-based energy continues to cause major damage to the human and planetary health through pollution and global warming. Renewables such as solar and wind have tremendous potential but need development of smart grids and storage technologies. However, sparse power-densities and the unpredictable nature of weather, makes reliance on them for baseload power generation limited. These problems are overcome by nuclear energy, although concerns surrounding safety of reactors and links with weapons proliferation have hindered the deployment of the available fission energy. Fusion on the other hand can safely navigate around the issues plaguing fission. Provided of course the scientific and technological hurdles are overcome, fusion energy has the potential to completely replace fossil-fuel. Chapter 2 discusses some approaches to fusion energy, in particular magnetic confinement fusion (MCF) - the concept underpinning the first terrestrial reactor being built to demonstrate self-sustaining fusion.

Chapter 2

Magnetic confinement fusion

There are many routes to achieving fusion. In stars, the enormous inwardly directed gravitational pressure balances the (fusing) plasma pressure, preventing the plasma from dispersing - ensuring a sustained 'burn'. Under terrestrial conditions however, such 'gravitational confinement' is no longer possible, and we must resort to alternative approaches to confine the fusion fuel:

(a) *Inertial Confinement Fusion:* This approach involves heating a multi-layered spherical pellet of D-T fuel using incident lasers/ion beams [42, 43]. Energy is rapidly deposited onto the outer 'ablator' shell of the pellet, which explodes, sending an inwardly directed momentum pulse and compressing the inner fuel layers. Fusion is initiated in the hot, high-density core, and the inertia is expected to keep the burning fuel together for a sufficiently long period of time to yield an *energy gain* before disassembly, i.e. $Q = P_{\text{fus}}/P_{\text{in}} > 1$. This approach has demonstrated that more energy can be generated by the D-T fuel than is *deposited* [44], but significant laser-target coupling inefficiencies[1] and the inherent pulsed nature of ICF, makes its commercialisation as a source of electricity extremely challenging.

(b) *Magnetic Confinement Fusion:* Arguably the more promising route to realising terrestrial fusion energy, magnetic confinement fusion (MCF) involves containing charged ions using magnetic fields. This approach can be made steady-state, making it attractive for power generation.

In the following sections we discuss some key physics principles that underpin the development of MCF-based reactors, with particular focus on the 'tokamak' concept. Different routes of optimising the performance of tokamaks are subsequently discussed.

[1] Of the 1.8 MJ laser energy, only ~ 150 KJ was coupled to the ablator. Roughly a tenth of this ablator energy was ultimately transferred to the D-T fuel.

2.1 Magnetic fields and charged particle orbits

2.1.1 Parallel and perpendicular field-line motion

Consider the Lorentz force on a charged particle:

$$m\frac{\mathrm{d}\mathbf{v}}{\mathrm{d}t} = Ze\left(\mathbf{E} + \mathbf{v}\times\mathbf{B}\right). \tag{2.1}$$

Following [45], in the absence of any electric field and for a uniform magnetic field $\mathbf{B} = B\hat{\mathbf{k}}$, we may decompose eqn. 2.1 into its Cartesian coordinates:

$$\frac{\mathrm{d}v_x}{\mathrm{d}t} = \Omega v_y\,, \qquad \frac{\mathrm{d}v_y}{\mathrm{d}t} = -\Omega v_x \quad \text{and} \quad \frac{\mathrm{d}v_z}{\mathrm{d}t} = 0\,. \tag{2.2}$$

Here $\Omega = ZeB/m$ and Z is the charge state (-1/+1 for electrons/singly-charged ions). The velocities in the plane perpendicular to the magnetic-field (x, y) form a coupled system, which is solved by differentiating either equation and substituting the result into the other, yielding

$$\frac{\mathrm{d}^2 v_{x,y}}{\mathrm{d}t^2} = -\Omega^2\, v_{x,y}\,. \tag{2.3}$$

We straightforwardly write $v_x = A\cos\Omega t + C\sin\Omega t$ and $v_y = \Omega^{-1}\left(\mathrm{d}v_x/\mathrm{d}t\right) = -A\sin\Omega t + C\cos\Omega t$. Using the initial conditions $v_x(t=0) = 0$ and $v_y(t=0) = v_\perp$, we find $v_x = v_\perp\sin\Omega t$ and $v_y = v_\perp\cos\Omega t$. Integrating once again with the initial conditions x_0, y_0, z_0 and $v_\parallel$:

$$x(t) - x_0 = \rho_L - \rho_L\cos\Omega t\,, \tag{2.4}$$

$$y(t) - y_0 = \rho_L\sin\Omega t\,, \tag{2.5}$$

$$z(t) - z_0 = v_\parallel t\,, \tag{2.6}$$

$$\text{and} \quad \left[x(t) - (x_0 + \rho_L)\right]^2 + \left[y(t) - y_0\right]^2 = \rho_L^2\,. \tag{2.7}$$

Here $\rho_L = v_\perp/\Omega$ is the Larmor radius. The net effect is a helical motion (Fig. 2.1):

(a) Along the field line, the charged particle motion is unaffected ($\mathrm{d}v_z/\mathrm{d}t = 0$).

(b) Perpendicular to the plane of the applied magnetic field, the particle is 'confined' to gyrate in circular orbits with radius ρ_L about the position $(x_0+\rho_L, y_0)$.

2.1.2 Particle drifts

Next, let us consider the Lorentz force equation of 2.1, but now in the presence of an additional generalised force $\mathbf{F}$. The velocity vector is separated into the gyro-motion about a centre $\mathbf{v}_g$, and the motion of this 'guiding' centre $\mathbf{v}_{gc}$. Since $m\,\mathrm{d}\mathbf{v}_g/\mathrm{d}t =$

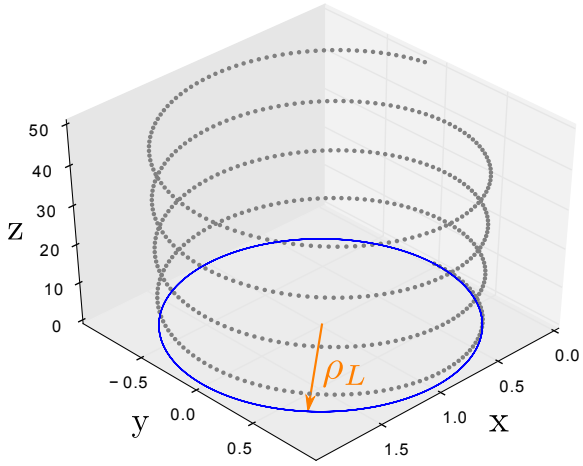

Figure 2.1: The motion of a positively charged particle in a uniform magnetic field as described by the eqns. 2.4-2.6. We choose $x_0 = y_0 = z_0 = 0.0$, $v_\parallel = 1.0$, $\rho_L = 1.0$ and $\Omega = 0.5$.

$Ze\,(\mathbf{v}_g \times \mathbf{B})$, the equation of motion reduces to

$$m\frac{\mathrm{d}\mathbf{v}_{gc}}{\mathrm{d}t} = \mathbf{F} + Ze\,(\mathbf{v}_{gc} \times \mathbf{B})\,. \tag{2.8}$$

Assuming a time-independent drift, $\mathbf{F}+Ze(\mathbf{v}_{gc}\times\mathbf{B}) = 0$. Next taking its cross-product with $\mathbf{B}=B\hat{\mathbf{k}}$, and noting that $\mathbf{v}_\perp = \mathbf{v} - \hat{\mathbf{k}}(\mathbf{v}.\hat{\mathbf{k}})$, it is straightforwardly seen that

$$\mathbf{v}_{gc,\perp} = \frac{\mathbf{F}\times\mathbf{B}}{ZeB^2}\,. \tag{2.9}$$

This is the drift of the guiding centre - perpendicular to both the background magnetic field and the direction of the applied force. A number of forces can arise in a plasma; the resulting drifts are described in Table 2.1. Note some of them are due to inhomogeneous and time-varying fields.

Table 2.1: Guiding centre drifts

Drift	Origin	Velocity	Remarks
∇B	Bunching of field-lines	$\frac{v_\perp^2}{2\Omega}\frac{\mathbf{B}\times\nabla B}{B^2}$	Comparable for electrons and ions, but in the opposite direction leading to current generation
Curvature	Centrifugal force from particles following curved field-lines	$\frac{v_\parallel^2}{\Omega}\frac{\mathbf{R}\times\mathbf{B}}{R^2B}$	Same as ∇B
$E\times B$	Electric field	$\frac{\mathbf{E}\times\mathbf{B}}{B^2}$	Electrons and ions drift at the same speed and in the same direction, so no current generated
Polarisation	Slowly varying electric field	$\frac{1}{\Omega B}\frac{\mathrm{d}\mathbf{E}}{\mathrm{d}t}$	Depends on charge and is greater for ions leading to a polarisation current

2.1.3 The magnetic mirror effect

The reflection of particles in a spatially varying magnetic field, or the so-called "magnetic mirror effect", can be understood by referring to Fig. 2.2. In the homogeneous magnetic field region (a) the Lorentz force F_L experienced by the particle, averaged over a gyro-orbit, is zero. However in region (b), there is clearly a force along $-\hat{z}$. If the initial velocity along $\hat{z}$ is small in relation to the deceleration caused by this force, the particle is ultimately reflected. In a rigorous calculation, this behaviour can be derived from two conserved quantities in a plasma - the particle's energy ε and its magnetic moment μ.

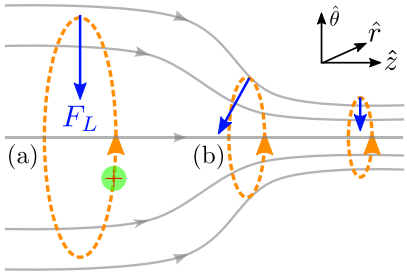

Figure 2.2: The magnetic mirror effect (see text for discussion).

2.1.3.1 Energy conservation

We take the scalar product of eqn. 2.1 with velocity; then noting $\mathbf{v}.\nabla\phi = \mathrm{d}\phi/\mathrm{d}t$ and $\mathbf{v}.\mathrm{d}\mathbf{v}/\mathrm{d}t = 0.5\,\mathrm{d}v^2/\mathrm{d}t$ we derive

$$m\mathbf{v}.\frac{\mathrm{d}\mathbf{v}}{\mathrm{d}t} = Ze\,(\mathbf{v}.\mathbf{E}) = -Ze\frac{\mathrm{d}\phi}{\mathrm{d}t}\,. \tag{2.10}$$

Thereby $\mathrm{d}\varepsilon/\mathrm{d}t = 0$, where $\varepsilon = mv^2/2 + Ze\phi$.

2.1.3.2 Magnetic moment conservation

The magnetic moment μ of a circular loop carrying a current I with a cross-sectional area A is defined as $\mu = IA$. For a gyrating charged particle, $A = \pi\rho_L^2$ and $I = Ze(2\pi/\Omega)^{-1}$, implying that

$$\mu = \frac{Ze\rho_L v_\perp}{2} = \frac{mv_\perp^2}{2B}\,. \tag{2.11}$$

We are interested in the component of the velocity along the magnetic field, i.e. v_z. Consider $\nabla.\mathbf{B} = 0$ in cylindrical coordinates and assume azimuthal (θ) symmetry[2]. Further taking $\partial B_z/\partial z$ to be constant over the Larmor radius scale-length of interest, we derive $B_r = -(\rho_L/2)(\partial B_z/\partial z)$. Using the Lorentz force equation and setting $B_\theta = 0$

[2]These assumptions have been made for simplicity and are easily relaxed following ref. [35].

for simplicity:

$$m\frac{\mathrm{d}v_z}{\mathrm{d}t} = Zev_\perp\left(-\frac{\rho_L}{2}\frac{\partial B_z}{\partial z}\right) = -\mu\frac{\partial B_z}{\partial z}\ . \tag{2.12}$$

Noting $\mathrm{d}\varepsilon/\mathrm{d}t = 0$ and $v_z(\mathrm{d}v_z/\mathrm{d}t) = -(\mu/m)(\mathrm{d}B_z/\mathrm{d}t)$, we derive $\mathrm{d}\mu/\mathrm{d}t = 0$ (here $\phi = 0$, though this assumption can be relaxed). Next from the conservation relations for magnetic moment and kinetic energy, it is straightforward to see

$$v_z^2 = v_0^2\left(1 - \frac{B}{B_0}\sin^2\Theta\right)\ , \tag{2.13}$$

where v_0 and B_0 are the velocity and field at the initial position and $\sin\Theta = v_{\perp,0}/v_0$. The particle is *reflected* when $v_z^2 < 0$. This is possible if

(a) the particle moves into a high field region such that $B > B_0/\sin^2\Theta$, or

(b) for a given maximum B, $\sin^2\Theta > B_0/B$, i.e. the particle has a high $v_{\perp,0}/v_0$, which means a relatively weak velocity component along the magnetic field.

2.2 The MCF reactor concept

A current-carrying solenoid provides the simplest way to confine charged particles by producing a homogeneous axial magnetic field. But open ends imply that particles are free to escape the system. This end-leakage problem is (partially) circumvented by establishing stronger magnetic fields at both ends of the solenoid (similar to Fig. 2.2) and reflecting particles back as they approach the throat of this "magnetic bottle". Over time, collisions however scatter particles in the $v_\perp - v_\parallel$ velocity space, with particles gaining a high $v_\parallel$ able to leave the magnetic-mirror trap. This end-loss problem is ultimately solved by eliminating the ends altogether: the solenoid is deformed into an axisymmetric torus. The first experimental fusion reactor being built with the capability of sustaining a self-heated plasma (for up to an hour [46]), ITER, is based on the 'tokamak' design (Fig. 2.3). This concept is discussed in the following sections.

2.2.1 Toroidal field coils

The toroidal magnetic field B_ϕ is produced by passing currents through the toroidal field coils. The close packing of coils at the inboard side leads to a radial variation in the magnetic field, $B_\phi \propto 1/R$, with ∇B pointing radially inwards. This causes the electrons and ions to drift in opposite directions, inducing an electric field as illustrated in Fig. 2.4. The effect of the curvature-drift is similar to the ∇B drift, enhancing this vertical electric field and the associated $E \times B$ drift. The net effect is that both electrons and ions drift radially outwards and confinement is lost.

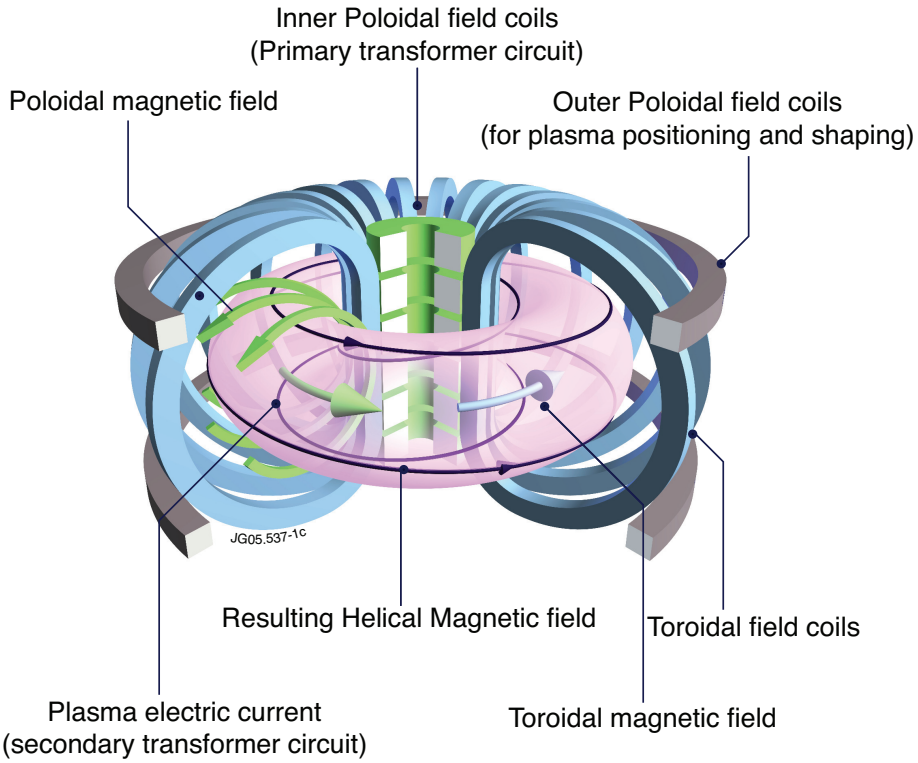

Figure 2.3: The tokamak design: The inner poloidal field coils generate a plasma current, which together with the toroidal field coils provide a helical magnetic configuration to confine the plasma. The outer poloidal field coils provide additional stability and help channel the exhaust plasma to special targets designed to handle high heat fluxes. (Reproduced with permission from [47].)

2.2.2 Inner poloidal field coils

To minimise the outward drift resulting from charge polarisation, a poloidal field B_θ is imposed. This field is generated by driving a plasma current in the toroidal direction through a transformer action: the inner poloidal coils (Fig. 2.3) act as the primary windings and the plasma itself acts as the secondary (the current drive in a tokamak is not necessarily inductive; see section 2.2.4.1). The current also ohmically heats the plasma. The resulting helical field 'shorts' the top and bottom of the poloidal plane, substantially reducing the undesired charge separation. Note that the particles are still drifting vertically, but sampling the full poloidal plane cancels this effect (see Fig. 2.8b for explanation). However, there is a limit on the strength of this poloidal field that is generated by the equilibrium current I_p: there is a B_θ pressure difference due to I_p following the toroidal curvature, which would amplify any perturbation to the equilibrium current. A strong axial field B_ϕ is essential to the stability of such systems, since the perturbations must first expend their energy bending this imposed field. Formally, such 'kink' perturbations are completely stabilised when

$$q(r) = \oint \frac{r}{R}\frac{B_\phi}{B_\theta}\mathrm{d}\theta > 1\,. \tag{2.14}$$

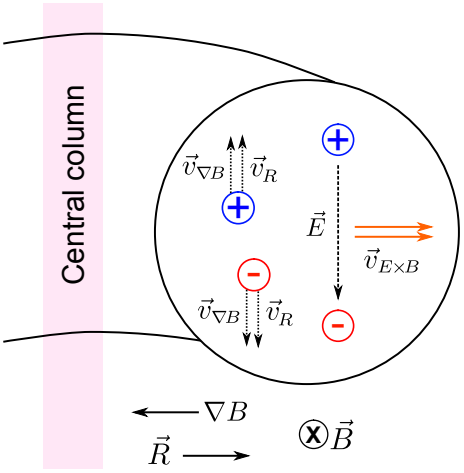

Figure 2.4: Ions and electrons drift vertically in opposite directions due to ∇B and curvature drifts. The resulting polarisation induced $E \times B$ drift causes both species to drift radially outwards.

This is the Kruskal-Shafranov criterion [48, 49] and limits the maximum current ($\propto B_\theta$) that can be carried by the plasma for an available B_ϕ. The appearance of $q \leq 1$ surfaces[3] in tokamaks lead to periodic collapses in the temperature/density/current profiles, termed 'sawtooth-oscillations' [50].

Flux surfaces

The combination of toroidal and poloidal fields leads to the formation of magnetic flux surfaces (Fig. 2.5a). As noted in Appendix A, these surfaces are contours of constant pressure. Special surfaces on which the 'safety-factor' $q(r)$ is rational, magnetic field lines map back onto themselves - these have important implications for stability and shall be discussed in detail later. Now due to their bending in a torus, the flux surface area on the outboard side is more than that on the inboard side. This leads to an outward 'Hoop-force' and the centre of these surfaces get shifted by an amount Δ, referred to as the 'Shafranov shift' (Fig. 2.5b). The minimisation of the flux-surface separation leads to increased magnetic- and flow-shears, and these have stabilising influences on a number of instabilities responsible for degrading the confinement in a tokamak (discussed in Chapter 3). The pressure can then build-up, increasing the Shafranov shift and this positive cycle ensues until the shear can no longer stabilise the dominant class of plasma instabilities.

2.2.3 Outer poloidal field coils

The outer poloidal field coils are typically employed to create a vertical magnetic field B_v, such that an inwardly directed $\mathbf{J} \times \mathbf{B_v}$ force stabilises the plasma expansion (here $\mathbf{J}$ is the plasma current density). Since the plasma current is generally very

[3]The safety-factor $q(r)$ is also the number of toroidal turns a magnetic field must make in order to complete a single poloidal turn.

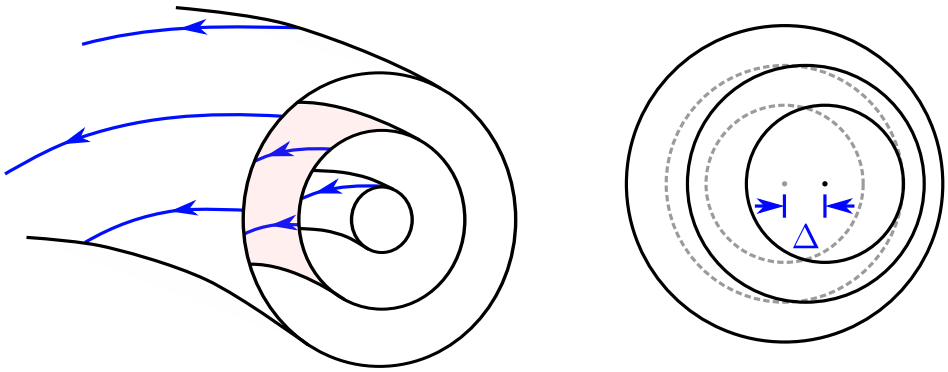

Figure 2.5: Schematics of (a) magnetic field lines (blue) spiralling around flux surfaces (middle surface highlighted) forming a set of nested tori, and (b) the Shafranov shift of these surfaces as visualised on the poloidal plane.

high, a small B_v is sufficient to stabilise the plasma and the magnetic fields follow the typical ordering $B_\phi > B_\theta > B_v$ [51]. Going beyond this, TCV (Tokamak à Configuration Variable), for example, uses up to 16 poloidal coils [52] to optimise the plasma geometry for stability [53, 54] and developing novel heat handling techniques such as the Snowflake divertor [55].

2.2.4 Alternative designs and scenarios

Before proceeding further, it is useful to comment on one key challenge the tokamak design faces en-route to delivering commercial fusion energy. In order to generate the plasma current that produces B_θ, current through the inner poloidal coils must be ramped up (or down). The current cannot be varied indefinitely, highlighting the pulsed nature of such a scenario.

2.2.4.1 Non-inductive current drive and heating

The transformer action not only drives a toroidal current, but also provides resistive heating, with a power/volume of $P_{\mathrm{OH}} = \eta j^2$ deposited in the plasma (here $\eta \propto T^{-3/2}$ is the plasma resistivity and j the current density). Above 3 keV ohmic heating is no longer effective and supplementary heating is required to reach the 10 keV temperature range to maximise the fusion cross-section and get significant self-heating (see section 2.3). The additional heating can either be provided by injecting neutral beams into the plasma or by launching radio frequency (RF) waves. Neutral Beam Injection (NBI) can not only heat the plasma, but tangentially directed beams can impart significant torque (the sizeable benefits of this are discussed in Chapter 3). Because the beams ions transfer their energy to plasma ions and electrons at different rates (see ref. [51], section 8.2), this approach can also be used to drive a current. RF waves can be launched at ion (30-120 MHz) and electron (28-140 GHz) cyclotron

frequencies and their harmonics to resonantly heat a particular species. Since the cyclotron frequency varies with B, and B with the radius, tuning the frequency allows heating of specific locations in the plasma. Finally, RF waves can be launched at the intermediate Lower Hybrid frequency (1-8 GHz) parallel to the magnetic field. The phased array antenna couples preferentially with electrons travelling in one direction; wave to electron energy transfer through Landau damping then results in a net current. Reference [56] reviews methods to generate a continuous plasma current.

2.2.4.2 Stellarators

By employing a complex set of coils, stellarators can generate the helical fields necessary for confinement without the need for plasma current. This makes them intrinsically steady-state and also removes a whole class of current-driven plasma instabilities (such as the sawteeth). While these are key advantages over the tokamak design, stellarators are extremely complicated to build, and once constructed, lack the flexibility of tokamaks to experiment with varied plasma configurations. Reference [57] compares the plasma operation in both devices.

2.3 Fusion triple product

The fusion triple product is a figure of merit used in nuclear fusion research and simply gives the condition to create sufficient power to sustain a self-heated fusion plasma, i.e. ignition. This can be derived from simple power balance arguments. The energy content of a D-T plasma is

$$W = \oint \frac{3}{2} n \left(T_e + T_i\right) \mathrm{d}V = \oint 3nT \, \mathrm{d}V \, . \tag{2.15}$$

But this energy leaks out at a rate characterised by τ_E (the energy confinement time) and the resulting power loss $P_L = W/\tau_E$ must be compensated either by external heating P_H or via self-heating through fusion-born alphas P_α. Ignition is when

$$P_\alpha = \oint \frac{1}{4} n^2 \langle \sigma v \rangle E_\alpha \, \mathrm{d}V \; > \; P_L \, , \tag{2.16}$$

$$\text{i.e.} \quad n\tau_E \geq \frac{12T}{\langle \sigma v \rangle E_\alpha} \, . \tag{2.17}$$

Here E_α is the energy carried by the fusion-born alphas and $\langle \sigma v \rangle$ characterises the D-T reaction rate. In the temperature range of 10-20 keV where this cross-section is maximised, $\langle \sigma v \rangle \approx 1.1 \times 10^{-24} T^2$ m^{-3}s^{-1} (with T in keV). These numbers give the condition $nT\tau_E \geq 3 \times 10^{21}$ m^{-3}keVs. A more accurate treatment with parabolic (instead of flat) temperature and density profiles yield a slightly higher requirement

on the fusion triple product [35]

$$nT\tau_E \geq 5 \times 10^{21} \text{ m}^{-3}\text{keVs} . \tag{2.18}$$

Figure 2.6 shows the steady progress that has happened over the years towards the attainment of this condition. Consider the three parameters that appear in the triple-product:

(a) The temperature T indicates the energy needed to overcome the Coulomb repulsion for fusion. If the particles are too energetic, the time-window for interaction decreases, making fusion less probable. The optimum temperature window of 10-20 keV is routinely accessed in most tokamaks (Fig. 2.6).

(b) In present day devices, the maximum attainable line-averaged electron density is set by the empirical Greenwald scaling $\overline{n}_{e,G} = \kappa\overline{j}$, where κ is the plasma elongation and $\overline{j}$ is the poloidally-averaged current density [58, 59]. The optimum value of n is $\sim 10^{-6}$ times the atmospheric density[4].

(c) τ_E, or the energy confinement time, has been the most challenging to maximise. It is here that the biggest advances have been, and need to be made.

2.3.1 Optimising the confinement time

Using $T \sim 10$ keV and $n \sim 10^{20}$ m^{-3} we find that $\tau_E \sim$ seconds for ignition. ITER, which will have twice JET's major radius, be 30% hotter and have a 50% stronger toroidal magnetic field on axis, hopes to ignite by improving from the $\tau_E \sim 0.5 - 1$ s observed on JET [60] to ~ 5 s. This can be inferred from the scaling $\tau_E \propto L^3B^2T^{-3/2}$ [62]. Expressed another way, the triple-product $nT\tau_E \propto (\beta_N H_{98}/q_{95}^2)R^{1.3}B^3$ [63], can be optimised using three distinct approaches:

(a) Make the device bigger, i.e. increase the radius R, so that it takes longer for the energy to escape. This is the reason why the current generation of tokamaks, including ITER, need to be so large. But the strong cost scaling with device size ($\propto R^3$) implies that this may not be the most economical route to commercialising fusion energy.

(b) Technological innovations such as high field, high temperature superconductors allowing powerful magnetic fields B [64], would allow a strong increase in the triple-product while allowing the device to become smaller. The conceptual ARC reactor, a JET-scale device with an ITER-like performance, is based on such a technological advance [65].

[4] An alternate constraint on the density comes from the maximum achievable magnetic field pressure $B^2/2\mu_0$ which must balance the plasma pressure $3nT$. For $B \sim 1$ Tesla and $T \sim 10$ keV, $n \sim 10^{20}$ m^{-3}.

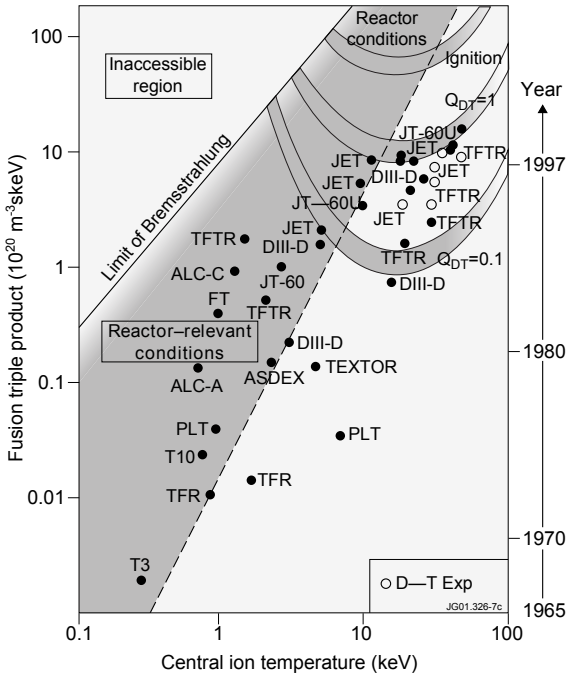

Figure 2.6: Plot showing the improvements made in the fusion triple product by various reactors over time. JET holds the record in fusion performance, producing 16 MW of alpha power and $Q = P_{\text{fus}}/P_{\text{in}} = 0.62$ [60]. Reference [61] however reports achievement of the equivalent reactivity of 'break-even' $Q > 1$ on JT-60U, assuming their D-D fuel could be replaced with D-T. (Reproduced with permission from [47].)

(c) Finally, if we could minimise transport, the confinement time improvement, quantified directly by H_{98} (see section 3.3.1) and β_N[5], would enable the plasma to achieve ignition conditions.

It is only because we can access regimes where transport is substantially reduced, does ITER not have to be twice as large to achieve its $Q = 10$ goal [66]. It is important therefore that we try and understand the mechanisms driving transport and get a better handle on the factors that could minimise the associated losses.

2.4 Particle losses and transport

Let us begin by considering the fluid equation of motion for either species in a plasma [67], in the absence of a magnetic field:

$$mn\left[\frac{\partial \mathbf{v}}{\partial t} + (\mathbf{v}.\nabla)\mathbf{v}\right] = Zen\mathbf{E} - \nabla p - mn\nu\mathbf{v}\,. \tag{2.19}$$

[5] $\beta_N = \beta/(aB/I_p)$, where a is the minor radius and β is the plasma pressure normalised by the magnetic field pressure.

In steady state $\partial\mathbf{v}/\partial t = 0$, and if the collision frequency[6] ν is large or $\mathbf{v}$ is small, the fluid element does not move into regions of different $\mathbf{E}$ and ∇p. Therefore the convective derivative can also be neglected. The flux for either species in an isothermal plasma can be written as

$$\mathbf{\Gamma} = n\mathbf{v} = \mu n\mathbf{E} - D\nabla n \,. \tag{2.20}$$

Here $\mu = Ze/m\nu$ and $D = KT/m\nu$ are referred to as the mobility and diffusion coefficients. For neutrals, or in the absence of electric fields[7], eqn. 2.20 reduces to Fick's first law of diffusion: $\mathbf{\Gamma} = -D\nabla n$. In plasmas however, with the possibility of organised motion (e.g. waves), this diffusive behaviour may not be strictly obeyed.

Particles are confined in a torus as long as they follow the magnetic field lines, but collisions in the perpendicular direction of motion could lead to radial excursions and ultimately loss from the torus. Such a process can be regarded as diffusive and, to estimate the distance a particle would travel in the radial direction, we invoke a simple 1D model of the classic random-walk problem. Then the squared-distance travelled after N steps, with step-length δ is

$$\begin{aligned}\left\langle x^2(N)\right\rangle &= \left\langle \left[x(N-1) \pm \delta\right]^2\right\rangle \\ &= \left\langle x^2(N-1)\right\rangle + \delta^2 \\ &= N\delta^2 \,.\end{aligned}$$

The motivation for summing over $x^2(N)$ as opposed to $x(N)$ is physical, since systems that perform random-walks (e.g. a "drunken sailor"), are likely to cover more ground with time [68], whereas $\langle x(N)\rangle = 0$. If each step takes a characteristic time τ, the total time $t = N\tau$. This allows us to define the diffusion coefficient $D = \delta^2/\tau$. Clearly, the distance d covered after N random-walk steps is

$$d = \sqrt{N}\delta = \sqrt{\frac{t}{\tau}}\delta \,. \tag{2.21}$$

2.4.1 Classical theory

It is evident from Fig. 2.7 that collisions between like particles do not lead to a net particle transport, whereas collisions between unlike particles leads to a net diffusion. Of the terms in eqn. 2.21, δ is determined by the electron/ion Larmor

[6]The collision frequency $\nu = n\overline{\sigma v}$ (σ is the interaction cross-section) is obtained by averaging over all the particle velocities v, and is defined such that eqn. 2.19 is correct. For illustration, here ν is approximated as a constant [67].

[7]In a tokamak, for trapped particles, the bounce-averaged toroidal equation of motion yields $v_\perp = -E_\phi/B_\theta$. Noting that the fraction of trapped particles is $\sim \varepsilon^{1/2}$ [35], the convective particle flux (Ware pinch) is found to be $\sim -\varepsilon^{1/2} nE_\phi/B_\theta$.

radius and τ is governed by the time-scale that causes the electron/ion velocity to change considerably upon collision[8] with the opposite species. For typical tokamak

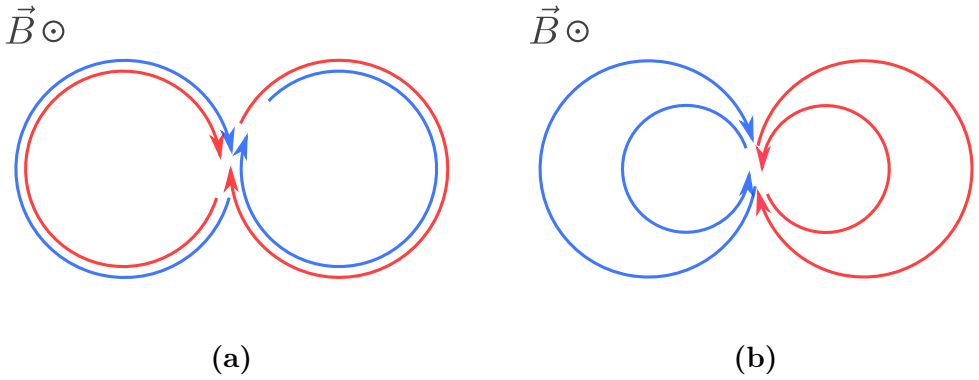

Figure 2.7: Particle trajectories before (blue) and after (red) collision for like (a) and unlike (b) particles.

parameters of $T_e = 10$ keV, $n = 10^{20}$ m^{-3} and $B = 1$ T, in 1 second an electron would have diffused $d_e = \rho_e/\sqrt{\tau_{ei}} = 1.8$ cm. As the ions begin to diffuse out quickly due to their larger Larmor radii, an electric field is set up to accelerate the electrons and retard the ion motion. This is known as 'ambipolarity' and ensures $d_e = d_i$ [67]. However, heat transport may occur when like-particles collide if they have different thermal velocities (e.g. in the presence of a temperature gradient). It turns out that due to the much larger step-length, ion-ion collisions are the dominant heat transport mechanisms. Note now $\tau = \tau_{ii} = \tau_{ei}\sqrt{(m_i/m_e)}/Z^2$ [69]. For the same parameters, in a second the energy diffuses a distance $d_E = 14$ cm. The discussion in section 2.3.1 then suggests that a machine with a minor radius of few 10s of cm should ignite.

2.4.2 Neoclassical theory

In tokamaks, the dominant toroidal magnetic field varies with major radius as $B_\phi \propto 1/R$. Particles starting off at the outboard side move into regions of stronger magnetic field as they follow the field lines. As discussed in section 2.1.3, this could lead to particle trapping. Neoclassical theory incorporates the effect of such trapped particles and describes the resulting transport. Following [69], for a large aspect-ratio circular cross-section tokamak (Fig. 2.8a), we can define the toroidal field variation as $B = B_0(1 - \varepsilon\cos\theta)$, where $\varepsilon = r/R_0 \ll 1$ is the inverse aspect-ratio and $B_0 \propto 1/R_0$. Following the procedure in section 2.1.3, we can write

$$v_\parallel^2 = v^2\left(1 - \frac{v_{\perp 0}^2}{v^2}\left[1 + 2\varepsilon\sin^2(\theta/2)\right]\right). \tag{2.22}$$

[8]The time it takes for an electron to deflect by 90° upon collision with an ion is given by the formula $\tau_{ei} = 3.44\times10^{11}T_e^{3/2}(n_e Z\ln\Lambda)^{-1}$. Here n_e is in m^{-3}, T_e is in eV and $\ln\Lambda \sim 10-20$ for fusion plasmas. The much more massive ions take considerably longer to be deflected by the electrons: $\tau_{ie} = (m_i/m_e)\tau_{ei}$ [69].

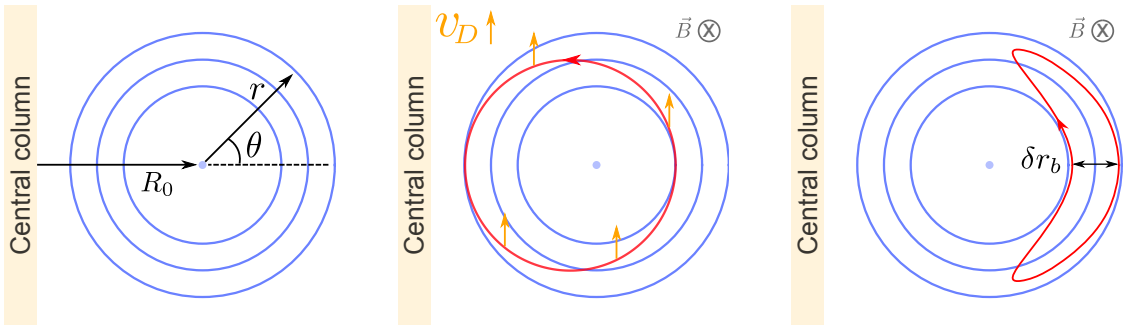

Figure 2.8: Schematics of the (a) poloidal cross-section of circular flux-surfaces (in blue), (b) passing particle dynamics (in red) and (c) the characteristic banana orbit of trapped particles. The vertical drift v_D is always upwards for ions in this geometry.

Here $v_{\perp 0}$ represents the perpendicular velocity at the outboard side. The maximum field is at $\theta = \pi$ and this gives the condition

$$\frac{v_{\perp 0}}{v_{\parallel 0}} \geq \frac{1}{\sqrt{2\varepsilon}} \tag{2.23}$$

(note that $\sqrt{2\varepsilon}$ is the trapped-particle fraction). Because of the curvature and ∇B drifts in the vertical direction, the particles do not stay on their starting flux surface. This leads to the characteristic 'banana orbit' (Fig. 2.8c) and the parameter δr_b sets the diffusive step length. For barely trapped particles, bouncing between $\theta = \pm\pi$, $v_\parallel = \sqrt{2\varepsilon} v_{th}$ and the distance travelled along the field line to complete half the orbit is $2\pi Rq$. The time to complete this is $t_b = (2\pi Rq)(\sqrt{2\varepsilon} v_{th})^{-1}$ and the width δr_b is therefore given by

$$\delta r_b = \frac{2\pi Rq}{\sqrt{2\varepsilon} v_{th}} \left(v_{\nabla B} + v_R\right) \ . \tag{2.24}$$

Noting $\mathbf{B} = (c/R)\hat{\mathbf{e}}_\phi$ and $\mathbf{R} = R\,\nabla R$ (where c is a constant), and using the relations from Table 2.1, we can straightforwardly write

$$\delta r_b = \frac{1}{R\Omega}\left(v_\parallel^2 + v_\perp^2/2\right)\frac{2\pi Rq}{v_{th}\sqrt{2\varepsilon}} \tag{2.25}$$

$$= \frac{1}{R\Omega}\left(2\varepsilon v_{th}^2 + v_{th}^2/2\right)\frac{2\pi Rq}{v_{th}\sqrt{2\varepsilon}} \tag{2.26}$$

$$= \frac{\pi q \rho_L}{\sqrt{2}}\left(\frac{4\varepsilon + 1}{\sqrt{\varepsilon}}\right) \approx \frac{\pi q}{\sqrt{2\varepsilon}}\rho_L \ , \tag{2.27}$$

where we assume a large aspect ratio. Therefore, if the particle is scattered from the passing to trapped orbit, the random-walk step-size increases by roughly $q/\sqrt{\varepsilon}$. For heat diffusion via ion-ion collision, $N \sim (t/\tau_{\text{eff}})\sqrt{2\varepsilon}$ and $\tau_{\text{eff}} = \tau_{ii}\varepsilon$. Here we have multiplied with the fraction of trapped particles, and τ_{eff} is needed to satisfy continuity requirements at the trapped-passing boundary. Combining these relations

we obtain

$$d_{\text{neo}} = \left(\frac{q\pi}{2^{1/4}\varepsilon^{3/4}}\right) d_{\text{c}} \,, \tag{2.28}$$

where d_{c} is the distance the energy diffuses in one second from classical estimates. For typical values of $\varepsilon \sim 0.33$ and $q \sim 2.0$, the neoclassical heat transport is ~ 10 greater than the classical transport in a tokamak, setting the minimum radius for ignition to ~ 1 m.

2.5 Turbulent transport

In tokamaks, confinement time predictions made using neoclassical estimates of diffusion coefficients are an improvement on the classical value, but are still typically one to two orders of magnitude higher than experimentally observed levels [70]. This 'anomalous' transport is thought to be made up of turbulent transport. Turbulence arises due to the non-linear interaction of small scale fluctuations/instabilities, called microinstabilities, which are driven by the gradients in equilibrium plasma parameters. Experimental measurements and theoretical studies suggest that a class of microinstabilities known as *drift modes* are of particular importance (refer to section 3.2).

2.5.1 The electron drift wave

There are a range of drift instabilities that can develop in a tokamak plasma driven by the electron drift wave. It is therefore useful to understand the drift wave. Consider a slab of plasma (Fig. 2.9) with uniform electron temperature T_e, cold ions $T_i = 0$, no equilibrium flows or magnetic shear, but an equilibrium density gradient in the $-\hat{x}$ (radial) direction. A small ion density perturbation $n_1 \sim \exp[\mathrm{i}(k_z z + k_y y)]$ on the length scale $1/k_{z,y}$ is introduced. Due to their small mass, electrons can respond rapidly along the magnetic field $\mathbf{B}$ and establish force balance on time-scales much smaller than that characterising the perturbation dynamics. This is referred to as the adiabatic/Boltzmann response. The resulting potential perturbation ϕ_1 (associated with n_1) leads to an $\mathbf{E}\times\mathbf{B}$ drift of particles along $\hat{x}$, where $\mathbf{E} = -(\nabla\phi_1)_y$. The resulting *drift wave* propagates in the y (poloidal) direction with a velocity v_*, as shown in Fig. 2.9. In this case there is no amplitude growth (equivalently, *radial transport*). Dissipative effects such as electron-ion collisions or collisionless wave-particle interactions can break the adiabatic/Boltzmann phase relationship between n_1 and ϕ_1 [70]. This introduces an imaginary component and the wave becomes unstable (or stable). The unstable mode is referred to as the *electron drift mode*.

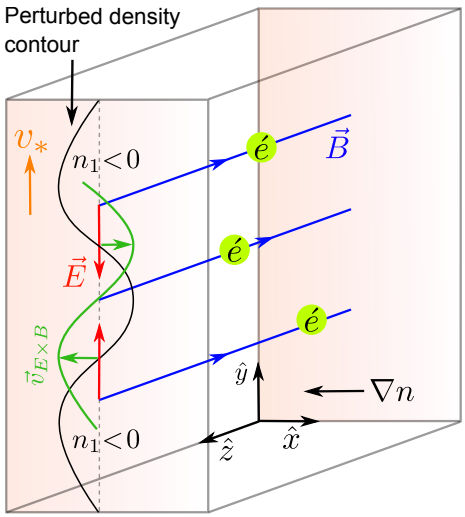

Figure 2.9: Schematic of the electron drift wave in a shearless slab. The density gradient ∇n is along $-\hat{x}$, the ion density perturbation is shown by the *black* contour and the associated $E \times B$ drift is shown by the *green* contour. The wave propagates in the $\hat{y}$ direction with a velocity v_*. The electrons $\grave{e}$ respond along the magnetic field $\vec{B}$.

2.5.2 The Ion Temperature Gradient mode

Introduction of other equilibrium gradients can also destabilise the drift wave: one such instability results from the presence of an ion-temperature gradient (ITG). As for the case of the electron drift wave, we assume the electrons to respond adiabatically. Following the work of Dickinson [71], we use a two-fluid (electron-ion) model to characterise the ITG mode dynamics. Reference [72] notes that observations of comparable electron and ion transport is suggestive of a fluid-like picture. Significant ion-temperature is allowed such that $P_i \neq 0$ and $\nabla T_i \neq 0$, but T_e is taken to be constant. The underlying physics has been explained with the help of Fig. 2.10. The ITG instability does not require a density gradient, but we retain ∇n to demonstrate its important stabilising influence. A good understanding of the ITG mode physics can be obtained by studying its linear characteristics. Linearisation is performed by decomposing a quantity f into its steady-state and fluctuating parts, i.e. $f = f_0(\mathbf{x}) + f_1(\mathbf{x}, t)$; the fluctuation in turn is described by the form $\exp[\mathrm{i}(\mathbf{k}.\mathbf{x} - \Omega t)]$, where $\Omega = \omega + \mathrm{i}\gamma$ is the complex mode frequency. The product of two fluctuating parts is neglected and the plasma is considered stationary, i.e. $\mathbf{v_0} = 0$. Since we consider a finite P_i, it is necessary to describe the ion-pressure fluctuations. This is governed by the adiabatic equation of state (introduced to provide closure to the set of fluid equations):

$$\frac{\mathrm{d}}{\mathrm{d}t}\left(P n^{-\kappa}\right) = 0\,. \tag{2.29}$$

Here κ is the adiabatic index. Using the linearised ion continuity equation

$$\frac{\partial n_1}{\partial t} + n_0 \nabla.\mathbf{v_1} + \mathbf{v_1}.\nabla n_0 = 0\,, \tag{2.30}$$

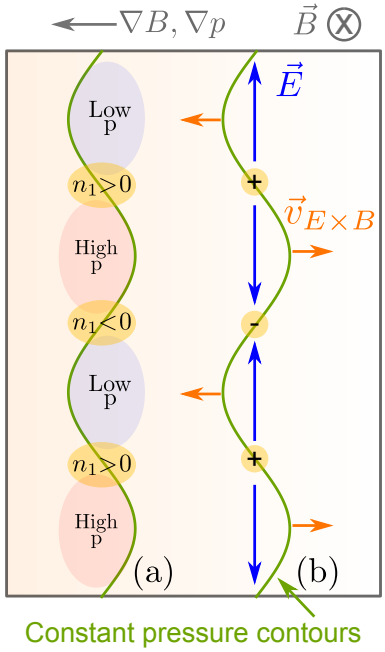

Figure 2.10: Schematic of the ITG mode in slab. (a) shows the contour of constant pressure (in *green*) with temperature (and associated pressure) perturbations. The ∇B drift leads to hotter particles drifting faster (see Table 2.1) and subsequent formation of regions of higher and lower densities. Using the picture of the electron drift wave described in Fig. 2.9, (b) shows how the resulting $E \times B$ drift amplifies the initial temperature perturbation.

we are able to eliminate density from eqn. 2.29 to obtain

$$\frac{\partial P_1}{\partial t} + \kappa P_0 \boldsymbol{\nabla}.\mathbf{v_1} + \mathbf{v_1}.\boldsymbol{\nabla} P_0 = 0 \,. \tag{2.31}$$

Next, consider the force balance equation for each species. The electron response parallel to the field line is obtained by neglecting collisions and electron inertia:

$$0 = n_e q_e E_\parallel - \nabla_\parallel P_e \,. \tag{2.32}$$

Noting that parallel gradients are only in the perturbed quantities and by linearising density we derive the adiabatic/Boltzmann relation:

$$n_{e1} = -n_0 \frac{q_e \phi_1}{T_e} \,. \tag{2.33}$$

Next, neglecting collisions, consider the perturbed parallel ion motion using the momentum equation:

$$\mathbf{v}_{i,\parallel} = -\frac{\mathrm{i}}{m_i \Omega} \left(q_i \nabla_\parallel \phi_1 + \frac{\nabla_\parallel P_1}{n_0} \right) \,. \tag{2.34}$$

Consider now eqn. 2.30. In deriving the second term, we note that $\boldsymbol{\nabla}.\mathbf{v}_\perp = 0$ in a shearless slab, and take $\mathbf{v}_\perp$ to be given predominantly by the $E \times B$ drift [72]. Hence

only

$$\nabla.\mathbf{v}_{i,\parallel} = \frac{\mathrm{i}\omega_s^2}{T_e\Omega}\left(q_i\phi_1 + \frac{P_1}{n_0}\right) \tag{2.35}$$

enters the ion continuity equation. Here we have defined $\omega_s = k_z c_s$, with c_s the ion sound speed at the electron temperature and ω_s the associated frequency. Next we consider the term $\mathbf{v}_1.\nabla$ in eqn. 2.30. Since the equilibrium gradients are only in the radial direction, only the perpendicular velocity component is present:

$$\mathbf{v}_{1,\perp}.\nabla n_0 = -\left(\frac{\nabla\phi_1 \times \hat{b}}{B}\right).\nabla n_0 = -\frac{n_0}{L_n B}\left(\hat{x}\times\hat{b}\right).\nabla\phi_1 \tag{2.36}$$

$$= -\frac{\mathrm{i}k_y n_0}{L_n B}\phi_1 \ . \tag{2.37}$$

Here $L_n = n/n'$ is the density scale-length. Before proceeding further, it is useful to define the *diamagnetic frequency*. Considering the ion continuity in the perpendicular direction, we find

$$\mathrm{i}\Omega n_1 = -\frac{\mathrm{i}k_y n_0}{L_n B}\phi_1 \ . \tag{2.38}$$

Invoking quasi-neutrality and the Boltzmann relation we derive

$$\omega_{*i}^n = \frac{k_y T_i}{L_n B q_i} \ . \tag{2.39}$$

Finally, collecting all the terms together, the ion-continuity equation is written as

$$-\mathrm{i}\Omega n_1 - \frac{\mathrm{i}k_y n_0\phi_1}{BL_n} + \frac{\mathrm{i}\omega_s^2 n_0}{\Omega T_e}\left(q_i\phi_1 + \frac{P_1}{n_0}\right) = 0 \ . \tag{2.40}$$

Setting $n_{e1} \approx n_{i1}$ and using the Boltzmann response to eliminate n_1:

$$\omega_s^2 P_1 = \left[\Omega^2 - \Omega\omega_{*e}^n - \omega_s^2\right] q_i\phi_1 n_0 \ . \tag{2.41}$$

Following a similar procedure for eqn. 2.31, we derive

$$\left[\Omega^2 - \frac{\kappa\omega_s^2}{\tau}\right] P_1 = \left[\frac{\kappa\omega_s^2}{\tau} - \Omega\omega_*^P\right] q_i\phi_1 n_0 \ . \tag{2.42}$$

Here $\tau = T_e/T_i$ and the pressure diamagnetic frequency $\omega_*^P = (k_y T_i)(q_i B L_p)^{-1}$ has been introduced, with $L_p = p/p'$ the pressure scale-length. Substituting eqn. 2.41 into 2.42 yields the desired ITG mode dispersion relation:

$$\Omega^3 - \Omega^2\omega_{*e}^n - \Omega\omega_s^2\left(1 + \frac{\kappa}{\tau}\right) + \omega_s^2\left(\omega_*^P + \frac{\kappa}{\tau}\omega_{*e}^n\right) = 0 \ . \tag{2.43}$$

We next isolate the effects of temperature and density gradients from the pressure term. Noting $L_p^{-1} = L_T^{-1} + L_n^{-1}$ we find $\omega_*^P = \omega_{*i}^T - \omega_e^n\tau^{-1}$, where $\omega_{*i}^T = (k_y T_i)(q_i B L_T)^{-1}$

has been similarly defined. Our dispersion relation then takes the final form:

$$\Omega^3 - \Omega^2\omega^n_{*e} - \Omega\omega_s^2\left(1+\frac{\kappa}{\tau}\right) + \omega_s^2\left[\omega^T_{*i} + \left(\frac{\kappa-1}{\tau}\right)\omega^n_{*e}\right] = 0\,. \tag{2.44}$$

2.5.2.1 Stability analysis

A cubic of the form $a + bx + cx^2 + dx^3 = 0$, with real coefficients, has complex roots provided $18abcd - 4c^3a + c^2b^2 - 4db^3 - 27d^2a^2 < 0$. The positive imaginary solution corresponds to the unstable ITG mode branch. In Fig. 2.11 we plot ω^n_{*e}/ω_s against ω^T_{*i}/ω_s. It can be seen that even in the absence of a density gradient, i.e. $\omega^n_{*e} = 0$, a small temperature gradient can be supported. In general, for higher density gradients, the mode becomes unstable only by exceeding higher critical temperature gradients $1/L_{T,\mathrm{crit}}$, illustrating the stabilising influence of ∇n_0.

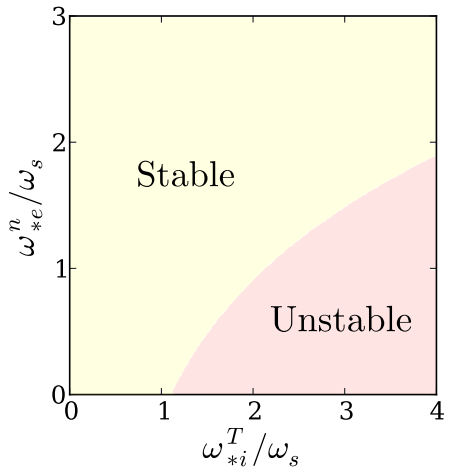

Figure 2.11: The plot indicates the stability boundary for the ITG mode in a slab geometry for the parameters $\kappa = 1$ and $\tau = 1$. For $\omega^n_{*e} = 0$, the mode becomes unstable when $\omega^T_{*i} > 1.089\omega_s$.

The critical-gradient onset of turbulence is an important concept in tokamaks. The rapid increase in transport fluxes when $1/L_T > 1/L_{T,\mathrm{crit}}$, pins the profiles close to this threshold (for example, see Fig. 3.2).

2.6 Fluctuations and transport

It is believed that electrostatic and electromagnetic instabilities release the free energy trapped in the equilibrium gradients by driving a steady level of fluctuation. The fluctuations in the associated perturbed quantities - temperature/density/magnetic field/electrostatic potential - can in turn lead to a radial excursion of particles and heat. For electrostatic modes in a slab, the perturbed radial velocity from the dominant $E \times B$ motion is $\delta v_x = \left(\delta\mathbf{E}\times\mathbf{B}\right)_x/B^2 = \delta E_y/B$, whereas for electromagnetic modes, the magnetic field stochasticization leads to a perturbed radial magnetic

field component δB_x. Density fluctuations cause associated charge separations, resulting in an outward drift of the underlying density perturbation, whereas the bulk species can freely stream along any magnetic field perturbation. The net convective radial flux of particles for a species j, Γ_j, is therefore

$$\Gamma_j = \frac{\langle \delta E_y \, \delta n_j \rangle}{B} + n_j \frac{\langle \delta v_{\parallel j} \, \delta B_x \rangle}{B} \, . \tag{2.45}$$

Associated with this convective particle flux is a heat flux $(5/2)T\Gamma_j$. The total thermal energy Q_j transported radially is a sum of this convective and two other conductive parts [35]:

$$Q_j = \frac{5}{2} T \Gamma_j + \frac{3}{2} \frac{n_j \langle \delta E_y \, \delta T_j \rangle}{B} + \kappa \nabla_\parallel T_j \, . \tag{2.46}$$

Here the second term is due to temperature fluctuations and the third term is due to the magnetic perturbations directing the large parallel conductive heat flux radially (the function κ depends on δB_x, collisionality and strength of the turbulence). The brackets $\langle \dots \rangle$ denote an average over the y coordinate (or the flux-surface). Measurements over an entire flux-surface are impractical, therefore, the surface-average is typically replaced by the time-average at each radial point [35]. Such a procedure should be carefully applied, since fluctuations may not be poloidally symmetric (see Section 3.5).

2.6.1 Theoretical description

We attempt a simple theoretical description of electrostatic-fluctuation driven transport using a random-walk model. Decomposing the perturbed potential into Fourier harmonics we may directly write

$$\delta v_k = -\mathrm{i} \frac{k_y \delta \phi_k}{B} \, . \tag{2.47}$$

If the particle velocity δv_k persists for a time τ_k, known as the correlation time, the particle would have travelled a distance $\delta r_k = \delta v_k \tau_k$. The diffusion coefficient is simply

$$D_k \approx \frac{(\delta r_k)^2}{\tau_k} = -\left(\frac{k_y \delta \phi_k}{B} \right)^2 \tau_k \, . \tag{2.48}$$

The parameter τ_k is determined by the process which most rapidly limits the unidirectional radial $E \times B$ drift. For example, with trapped particles, $1/\tau_k$ may correspond to the frequency with which collisions cause de-trapping. One could estimate the fluctuation amplitudes $\delta \phi_k$ and δn_k from the 'mixing-length estimate'. According to this, the instability drive is removed for the amplitude of δn_k such that the

equilibrium gradient becomes equal to the perturbed gradient, i.e.

$$\frac{n}{L_n} \sim \frac{\delta n_k}{\lambda_\perp} \,. \tag{2.49}$$

Further invoking the Boltzmann response, we see

$$\frac{e\delta\phi_k}{T} = \frac{\delta n_k}{n} \sim \frac{1}{k_\perp L_n} \,. \tag{2.50}$$

There is experimental evidence of this scaling across a number of tokamaks [73].

2.6.2 Measuring fluctuations

In order to understand the role fluctuations play in setting tokamak transport, it is necessary to measure the terms of eqn. 2.45. Note that the fluctuating radial velocity $\delta E_y/B$ in the first term of eqn. 2.45 time-averages to zero (see Fig. 2.9). A net transport can only occur if there are correlated variations in δn, such that more particles travel in one direction than the other. It should also be noted that the fluctuating electric field is associated with a potential variation and a scale-length $1/k_\perp$ - knowledge of the wavenumber spectrum $S(k_\perp)$ helps identify the mechanism(s) underlying these fluctuations. This highlights the complexity of correlating fluctuation measurements with transport studies: we require amplitudes and phases of δn, $\delta\phi$, δT, δB_r, $\delta v_\parallel$ and $S(k_\perp)$. The most comprehensive measurements so far have been made using Langmuir Probes (LP) [74] and Mirnov Coils (MC) [75] at the plasma edge (Fig. 2.12a). Towards the core, the probes no longer work because they would melt from the high heat fluxes, further injecting the impurities directly into the reactor core. In this region, diagnostics such as the Heavy Ion Beam Probe (HIBP) [76, 77], Beam Emission Spectroscopy (BES) [78, 79], Far Infra Red (FIR) scattering [80], Electron Cyclotron Emission Correlation Radiometry (ECECR) [81, 82], Cross Polarisation Scattering (CPS) [83] and Reflectometry [84] provide valuable insights. This has been summarised in Table 2.2.

2.6.3 Experimental correlation: fluctuation and transport

If transport is caused by fluctuations, it must be possible to correlate them (note however that fluctuations do not necessarily imply some transport, e.g. the stable drift wave described in section 2.5.1). At the plasma edge, probe measurements of amplitudes and phases allows for detailed quantitative comparisons between fluxes and fluctuations (see Fig. 2.12). In the plasma bulk however, making such measurements is much more challenging and we must resort to alternate means of relating fluctuations with transport. For example, in TFR, a clear linear correspondence was found between the inverse global energy confinement time $1/\tau_E$ and $(\delta n/n)^2$ in

Table 2.2: Diagnostics and typical fluctuation amplitude measurements (in brackets). Most of the data has been derived from [85, 86] and the references therein. See Fig. 2.12a for comparison.

Fluctuation	Edge measurement	Core measurement	Remarks
$\frac{\delta n}{n}$	LP ($> 30\%$)	Microwave/FIR scattering, BES, Reflectometry, HIBP ($< 1\%$)	• BES can be used to obtain 2D poloidal distribution of fluctuations • FIR allows monitoring of the entire $S(k_\perp, \omega)$ spectra throughout the discharge [87]
$\frac{e\delta\phi}{T_e}$	LP	HIBP	• (Expect) $e\delta\phi/T_e > \delta n/n$ at the edge, whereas Boltzmann response followed in the core [85] • The heavy-ion, e.g. thallium, energies $E \sim 100 - 1000$ keV $\gg e\delta\phi$ for small-medium tokamaks, implying application to the largest devices requiring higher beam energies is extremely challenging
$\frac{\delta T_e}{T_e}$	LP ($> 20\%$)	ECECR ($\sim 1\%$)	• Intrinsic thermal fluctuations are noise to the data; only recent advances have been able to separate noise from turbulent fluctuations with good confidence [82]
$\frac{\delta B_r}{B}$	MC ($\sim 10^{-4} - 10^{-5}$)	CPS ($\sim 10^{-4}$)	• Despite such low fluctuation levels, there is evidence linking internal magnetic perturbations to the right level of electron heat transport [88] • During strong tearing mode activity in the core, $\delta B_r/B \leq 10^{-2}$ has been measured using HIBP [89]

ohmic, ion cyclotron and neutral beam heated plasmas [35]. Assuming the Boltzmann relation holds in the core, this would resemble a scaling of the form 2.48. Further, the drop in the fluctuation level and the formation of an edge transport barrier (see Chapter 3) is seen to occur almost simultaneously (within 100 μs) [90]. Finally, advanced numerical simulations have allowed validations of turbulence models against experimentally measured fluxes to within experimental uncertainties [91]. However, other key parameters such as particle transport, wavenumber spectra and fluctuation levels were not compared. Confidence in our predictive capabilities will involve recovering simultaneously as many turbulent features as possible [92].

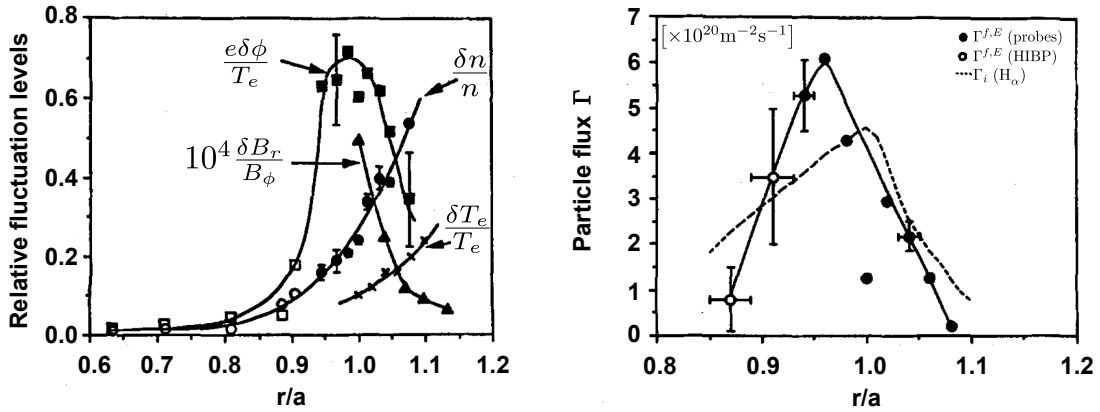

Figure 2.12: (a) shows the spatial profiles of different fluctuations in a TEXT limiter discharge and (b) shows the electrostatic particle flux $\Gamma^{f,E}$ for the same shot. There is a close positive correlation between the radial dependence of $\Gamma^{f,E}$ and $e\delta\phi/T_e$. (Reproduced from ref. [85] with permission from AIP Publishing LLC.)

2.7 Summary

Tokamaks and stellarators offer promising routes towards fusion energy. However, several technological, materials and physics challenges need to be overcome before commercialising fusion energy becomes possible. From the physics point of view, increasing the confinement time will significantly benefit the pursuit of fusion energy. There is mounting evidence that the anomalous transport observed over classical and neoclassical estimates can be attributed to turbulent fluctuations. A grand physics challenge is to minimise this turbulence caused by small-scale plasma instabilities. The next chapter discusses some candidate instabilities, how they could be stabilised, and the deleterious consequences associated with too good confinement. Finally, some key open questions, motivating the research carried out during this PhD, are identified.

Chapter 3

Towards modelling small-ELMs and intrinsic rotation

The discussion in Section 2.6 was about generic fluctuations and their relationship to transport in tokamak plasmas, without any reference to the underlying instabilities, or indeed, how this turbulent transport could be minimised or suppressed. In this chapter we will expand on these areas, as we build towards the outstanding physics questions that have motivated this project.

3.1 Quasi-linear theory for transport

Following [35], a more rigorous form for the diffusion coefficient (c.f. eqn. 2.48), relating the growth rate and wavenumber of a particular linear mode to the turbulent flux is derived. Let us begin by considering the continuity equation in the presence of an equilibrium source S

$$\frac{\partial n}{\partial t} + \nabla.(n\mathbf{v}) = S \tag{3.1}$$

and linearise the fluid density $n = \langle n \rangle + \delta n$ and velocity $\mathbf{v} = \delta\mathbf{v}$ (assuming zero equilibrium flow). Gradients are only in the radial direction x. Neglecting the product of two perturbed quantities and assuming incompressibility, the fluctuating part of eqn. 3.1 reads

$$\frac{\partial \delta n}{\partial t} + \delta v_x \frac{\partial \langle n \rangle}{\partial x} = 0 \, . \tag{3.2}$$

In the linear regime, we may decompose perturbations into Fourier harmonics k in the usual way, writing each component as $\exp[-\mathrm{i}(\omega_k + \mathrm{i}\gamma_k)t]$ and only picking out the irreversible part (i.e. real component) that contributes to the transport flux:

$$\delta n_k = -\frac{\gamma_k}{\omega_k^2 + \gamma_k^2} \delta v_{x,k} \frac{\partial \langle n \rangle}{\partial x} \, . \tag{3.3}$$

Using $\Gamma_{x,k} = \delta v_{x,k} \delta n_k$ and Fick's law (eqn. 2.20) one notes

$$D_\perp = \frac{\gamma_k}{\omega_k^2 + \gamma_k^2} |\delta v_{x,k}|^2 \ . \tag{3.4}$$

We next write the velocity in terms of the radial plasma displacement ξ_x and keep the irreversible contribution upon linearisation, i.e. $\gamma_k \xi_{x,k} = \delta v_{x,k}$. The radial displacement of a particle is typically within the instability's wavelength, and this assumption is used to write $\xi_{x,k} \approx 2\pi/k_x$. A further simplification is possible for isotropic perturbations: $k_x \approx k_y = k_\perp$. Then, $|\xi_{x,k}|^2 = 4\pi^2/k_\perp^2$ and

$$D_\perp = 4\pi^2 \left(\frac{\gamma_k}{k_\perp^2} \frac{\gamma_k^2}{\omega_k^2 + \gamma_k^2} \right)_{\max} \ . \tag{3.5}$$

From this quasi-linear estimate, we infer that instabilities with stronger linear growth rates and wider spatial extents would dominate transport in their non-linearly saturated states.

3.1.1 Flow-shear and transport

From eqn. 3.5, we note that turbulent diffusivity is reduced if the perpendicular wavenumber of the underlying instability could somehow be increased. One way of achieving this is by putting the isotropic turbulent eddy in a sheared velocity field $v_{E\times B} = \gamma_E x$ (Fig. 3.1a), associated with a radially varying electric field E_r [93]. It is straightforward to note from Fig. 3.1b that the major axis[1] gets modified as $L_l = L\sqrt{1 + (\gamma_E t)^2}$. Further assuming that the eddy area $\pi L_l L_\perp$ is conserved, the perpendicular wavenumber is modified according to

$$k_{\perp,\gamma_E} = k_{\perp,0} \left(1 + \gamma_E^2 t^2\right)^{1/2} \ . \tag{3.6}$$

This process persists for a correlation time $t = \tau_k$. Combining eqns. 2.50 and 3.6, we derive

$$\frac{\langle \delta n^2 \rangle}{\langle \delta n^2 \rangle_0} \approx \frac{1}{1 + \gamma_E^2 \tau_k^2} \ . \tag{3.7}$$

In the presence of sheared flows, the fluctuation amplitude, and therefore the particle and heat transport, are reduced. This simple picture of turbulent eddies tilting (and ultimately, splitting) seems to be supported by the 2D Gas Puff Imaging diagnostic on TEXTOR [94].

[1] The major axis of the ellipse is stretched along the $E \times B$ velocity field, whereas the minor axis shrinks and rotates to align perpendicular to the flow.

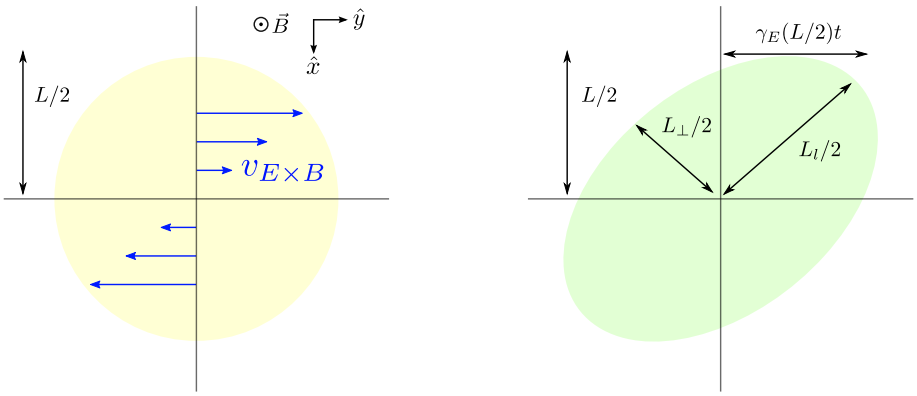

(a) **(b)**

Figure 3.1: (a) An initial isotropic fluid eddy with a sheared velocity field $v_{E\times B}$ imposed on it. (b) The fluid eddy is stretched with time and (not shown) can ultimately break down into multiple smaller eddies.

3.2 Candidate modes for turbulent transport

A number of drift modes exist in a torus, with their stability and scale-length determining γ_k and $k_\perp$. A few key ones are the ion/electron temperature gradient (ITG/ETG) mode, the trapped ion/electron mode (TIM/TEM), the kinetic ballooning mode (KBM) and the micro-tearing mode (MTM). Some of their features and the mechanisms responsible for driving and stabilising them are summarised in Table 3.1. More complete discussions can be found in references [95, 92].

3.2.1 Profile-stiffness

Before proceeding, it is useful to discuss the two closely related concepts of profile-stiffness and critical-gradient onset of turbulence. There is strong theoretical and experimental evidence that significant turbulent ion heat transport is triggered when a critical gradient in the ion-temperature is exceeded. The toroidal ITG mode is a strong candidate to explain this transport [119, 120]. Referring to Fig. 3.2, at low rotation, clearly $R/L_{T_i} = -c(r)$ with $c(r)$ a weakly varying function of r. Then the core temperature T_{core} is related to the edge temperature T_{edge} according to

$$\frac{T_{\text{core}}}{T_{\text{edge}}} = \exp\left(\int_{\text{core}}^{\text{edge}} \frac{c(r)}{R}\,\mathrm{d}r\right) \approx \text{constant}. \tag{3.8}$$

Reference [122] reports evidence of this scaling in ASDEX Upgrade.

3.3 Suppressing turbulence

In section 3.1.1 we discussed how flow-shear reduces turbulent transport. But crucially, electron and (in particular) ion diffusivities can be reduced to neoclassical

Table 3.1: Examples of toroidal drift modes and some of their key features [92, 96].

Mode	$k_\perp \rho_i$	Destabilisation	Stabilisation	Remarks
ITG	≤ 0.5	∇T_i	∇n_i, $E \times B$ shear [97, 98]	• Associated turbulence isotropic [99] • Linear critical-gradient up-shifted due to the stabilising influence of the nonlinearly generated, sheared 'zonal' flows [100, 101]
TEM/TIM [102]	0.2-1.0	∇T and ∇n of trapped particles	Minimising bad curvature region where particles are trapped [103], $E \times B$ [97, 98], Shafranov shift [104]	• Trapped particles are minimised in highly collisional edges and towards the core [35] • Dissipative (collision dependent) branch predicted to be more dangerous than the collisionless branch [35]
ETG	≥ 2.0	∇T_e	∇n_e, $\hat{s}$ [105, 106], Shafranov shift [107]	• Not affected by flow-shear due to small spatial scales and large linear growth rates [107] • Forms radially elongated 'streamer' structures with $k_r \ll k_\theta$ [108] • Can match experimentally relevant critical gradient profile [109]
MTM	≤ 1.0 [110], ~ 3 [111]	∇T_e	∇n_e	• Electromagnetic mode; involves tearing and reconnection of magnetic field-lines • Virulent close to the pedestal top [111]
KBM [112]	≤ 0.5 [113]	∇p [111], energetic ions [114]	Finite gyro-radius [115]	• Similar in spatial-scale to ITG, but exhibits shorter correlation times and much higher heat and particle transport [116] • An electromagnetic mode, so important at high β [117, 118]

levels when the $E \times B$ shearing rate exceeds the growth rate of the most unstable mode: $\omega_{E\times B} > \gamma_{\max}$ [123, 124]. There are several significant consequences of such a paradigm change in transport characteristics, and we discuss these in the subsequent

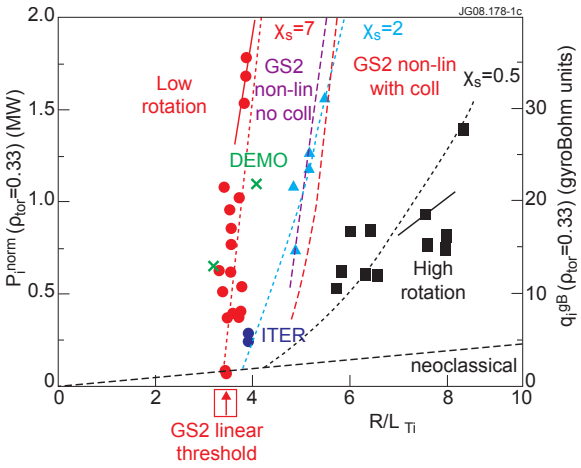

Figure 3.2: Plot showing the normalised ion heat flux as a function of temperature gradient for various plasma rotations (circles, triangles and squares). The 'stiffness' parameter χ_s characterises the ion thermal transport: a lower χ_s, associated with high rotation, would support stronger gradients due to reduced transport. (Reproduced from [121] courtesy of [47]; permission to publish obtained from the American Physical Society.)

sections.

3.3.1 High-confinement mode

In order to increase the plasma energy content beyond what is achievable with ohmic heating alone, tokamaks rely on additional heating (section 2.2.4.1). It was initially found that the confinement degraded with applied power P. This was referred to as the Low-confinement or 'L-mode' of operation, with the confinement time $\tau_{E,L} \propto P^{-0.5}$ [125]. But curiously, as the heating exceeded a certain threshold, a *bifurcated* state associated with an improved energy confinement time (typically twice that of the L-mode) could be accessed [126]. This high-confinement or 'H-mode' of operation has been reported by almost all tokamaks[2]. Figure 3.3 compares the two auxiliary heated modes of operation with the help of a cartoon. Note that the improved plasma pressure achieved across the radius can be attributed to a narrow region of improved confinement (~ cm) at the very edge of the plasma, called the 'pedestal'[3] [128, 129]. From eqn. 3.8, we observe straightforwardly that the core temperature $T_{\text{core}} \propto T_{\text{ped}}$, the temperature at the pedestal top. ITER's goal of delivering an energy gain of 10 is tightly hinged on its ability to access the H-mode.

Often in discharges with non-monotonic q profiles, or reversed shear, internal transport barriers (ITBs) can instead form near low-order rational surfaces (q = 2, 3) [130]. The desired q profile can be obtained by locally modifying the plasma current through non-inductive current drive schemes (see section 2.2.4.1). Although

[2]Often the parameter H_{98} is used to measure the 'quality' of the H-mode. This is basically the confinement time normalized to the IPB98(y,2) confinement time scaling for Type-I ELMy H-modes [126].

[3]The pedestal width can be given by the scaling $\Delta_{\text{ped}} \propto \rho_{\text{pol}}^{\nu} a^{1-\nu}$, where ρ_{pol} is the poloidal Larmor radius, a is the minor radius and $0 \leq \nu \leq 1$ [127].

reversed shear is not a sufficient condition for the formation of ITBs, it facilitates turbulence suppression through other processes such as flow-shear. The internal and edge transport barriers can co-exist, allowing very high performances with H_{98} = 1.7 – 1.9 [131]. The physics of ITBs is reviewed in ref. [130].

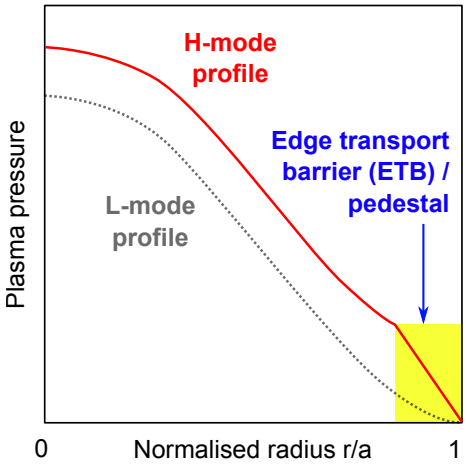

Figure 3.3: Cartoon illustrating the L- and H-modes of operation. The formation of a narrow (~ cm) edge transport barrier (ETB), or pedestal, characterises the H-mode.

3.3.2 Edge localised modes

The strong pressure gradient and the associated bootstrap-current[4] in the pedestal, can *simultaneously* destabilise pressure-driven 'ballooning' and current-driven 'peeling' modes [132]. This results in an explosive edge instability called the edge localised mode (ELM). At ELM onset, plasma filaments carrying substantial amount of particles and heat break away [133, 134]. These 'Type-I' ELMs can be extremely damaging to ITER, with the biggest ELMs projected to expel up to ~ 30 MJ of energy 20 times per second [135]. Such intense bursts of energy and particles would severely damage the heat-handling target plates, significantly reducing ITER's operational lifetime [136]. An acceptable lifetime for this 'divertor' plate requires an energy loss of < 6 MJ per ELM [137]. Such Type-I ELMs are unacceptable, but smaller ELMs within the material limits are in fact desirable: these periodic bursts of energy and particles help remove impurities (Helium ash, high-Z wall material sputtered into the plasma, etc.) and control density, allowing steady-state operation. There are many ways to avoid large ELMs: actively mitigate them by increasing their frequency (thereby reducing the energy released per ELM), eliminate/suppress them altogether, or identify intrinsic small/no-ELM regimes. These are discussed in turn:

[4]In the presence of a density gradient, radially-neighbouring trapped particles undergoing banana motion are associated with a parallel current. They can further transfer momentum to the untrapped ions and electrons. The bootstrap current arises due to the difference in the momentum exchanged with the passing electrons versus ions.

3.3.2.1 Active ELM control techniques

Magnetic fields generated by in-vessel current coils can 'puncture' the equilibrium flux surfaces, enhancing the radial transport. These resonant magnetic perturbations (RMPs) can mitigate [138] or completely suppress [139] Type-I ELMs without significant/any pedestal pressure degradation. Although in order to smooth the toroidally asymmetric heat-fluxes associated with RMP application [140], the ITER RMP coils are being designed to rotate the applied perturbation at few Hz [141]. Another approach involves firing small cryogenic D-pellets. Reference [142] showed that the natural ELM frequency, $f_{\mathrm{ELM}} \approx 30$ Hz, could be completely replaced by the pellet frequency f_{pel} above $f_{\mathrm{pel}} \geq 1.5 f_{\mathrm{ELM}}$, with a mild degradation in the pedestal stored energy, $W_{\mathrm{ped}} \propto f_{\mathrm{pel}}^{-0.16}$. It is understood that the cloud of deuterium generates a strong cross-field pressure-gradient, triggering small-ELMs. Reference [143] reviews these and other ELM-control methods for application to ITER scenarios. Although, while such techniques may provide the solution on ITER, going beyond, steady-state scenarios will benefit from intrinsic small/no-ELM regimes, which are likely to relax the level of shielding and maintenance that become necessary with added ELM-control components.

3.3.2.2 Small/no-ELM regimes

There are many different ELM categories. One may refer to [144] for a discussion on their characterisation or [145] for an overview of theoretical ideas relating to their onset. Here we briefly review the peeling-ballooning (PB) model that robustly describes the Type-I ELMs, and further provides plausible explanations for other small-/no-ELM regimes (see Fig. 3.4):

(a) In a hot plasma with a relatively long current diffusion time, one could expect the pressure gradient to quickly reach the ballooning boundary, where it'll remain tied due to the critical-gradient argument given before. The associated bootstrap current then rises towards the PB limit, triggering a large crash. This is widely accepted as the mechanism behind Type-I ELMs [129].

(b) Type-II ELMs are associated with Type-I-like pressure pedestals and exist in a narrow operational window at high densities. It is speculated that these ELMs are purely ballooning [145], with the high collisionality suppressing the bootstrap current, preventing the PB instability.

(c) Type-III ELMs are divided into 2 categories [146]: a high n_e, low T_e branch and a low n_e, high T_e branch (the latter is sometimes referred to as Type-IV). Both branches are associated with degraded pedestals in comparison with their Type-I counterpart. The low n_e branch, with a lower collisionality, is associated

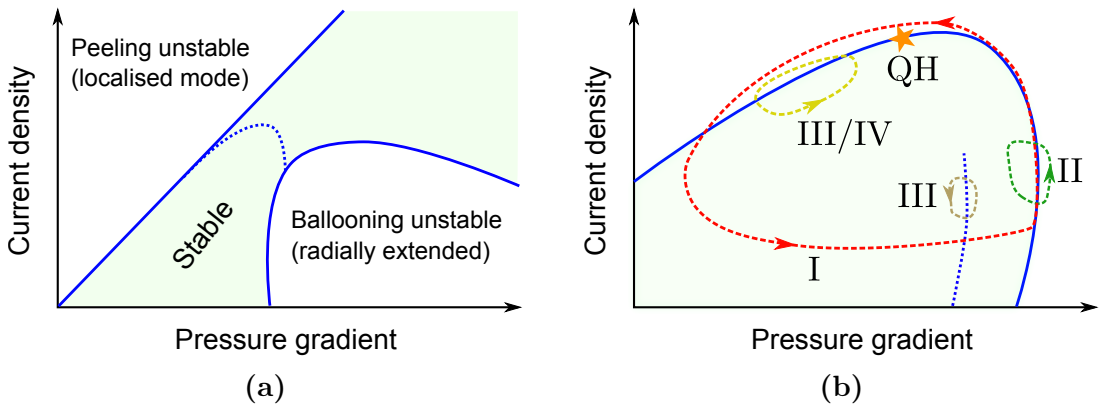

Figure 3.4: (a) The localised peeling mode (driven by current density and stabilised by pressure gradient) can couple (dashed-line) with the extended ballooning mode (destabilised by pressure gradient and stabilised by current density) for intermediate toroidal mode numbers (typically $n \sim 10{-}15$). (b) Different trajectories on this peeling-ballooning diagram can lead to different ELM types (see text for discussion).

with the pure-peeling mode whereas the high n_e, low T_e branch is associated with the resistive ballooning mode triggered at lower pressure gradients.

(d) The quiescent H (QH) mode [147] is a stationary ELM-free regime with high confinement. Low collisionality is important for its accessibility, making it ITER relevant. The following mechanism is thought to be responsible for its onset [148]: low n kink mode is destabilised by flow-shear; the radial mode growth damps the sheared flow (mode coupling to the wall provides another mechanism to brake the torque); the mode is stabilised and the flow-shear may increase again; this provides a saturation mechanism.

Another attractive operation scenario is the grassy-ELM regime. This is characterised by high confinement, tolerable energy loss per ELM, and appears in low-collisionality plasmas that are again relevant for ITER [144]. As of date, a robust theoretical understanding of the responsible physics mechanisms, which could guide the accessibility of small/no-ELM regimes on ITER, is lacking, and has been identified as a priority area by the ITPA Pedestal and Edge Physics topical group [149].

3.3.3 Intrinsic rotation

As the plasma enters the H-mode, there is an associated build-up of *intrinsic* torque in the co-current direction. Modelling [150] and observation [151] indicate that the rotation at the top of the pedestal increases with its width, propagating inwards into the core. Ion ITBs also exhibit spontaneous rotation [152], as does the I-mode regime which is characterised by an H-mode like temperature pedestal but L-mode like particle confinement [153]. The change in the toroidal rotation velocity ΔV_ϕ across the L-H transition is given by the 'Rice-scaling', $\Delta V_\phi \sim \Delta W/I_p$ (ΔW is the change in

the plasma stored energy and I_p the plasma current), with spontaneous core impurity toroidal rotations as high as 130 km/s, or a thermal ion Mach number $M_i = 0.3$, measured in plasma discharges [154, 155]. Understanding rotation in tokamaks is crucial for a number of reasons: (a) the L-H power threshold depends strongly on toroidal rotation [156]; (b) rotation can stabilise macroscopic MHD modes such as the internal kink[5] [157] and resistive wall modes [158]; and (c) profiles in rotating plasmas can become less stiff (Fig. 3.2), supporting stronger gradients. However, neutral beam injected torque, significant in present tokamaks, is predicted to be modest on machines such as ITER, with $M_i \approx 0.05$ [159]. Intrinsic torque is then expected to provide the dominant source of rotation, necessitating a deeper understanding of its physics. The underlying drive requires *symmetry-breaking*, which can occur via a number of mechanisms. References [160, 161] provide a comprehensive summary on the theories of turbulent momentum transport and intrinsic rotation. Here, we briefly comment on the 'heat-engine' model of [162], which captures some of the features of the Rice-scaling. According to this model, the radial inhomogeneity in temperature (i.e. ∇T) drives drift-wave turbulence, which generates flow via residual stresses. Detailed theoretical analysis yields the estimate $\langle V_\parallel \rangle \propto \rho_* L_s / L_T$ (here $\rho_* = \rho/a$, $L_s = q/q'$ and $L_T = T/T'$). Noting that $L_s \propto q \propto I_p^{-1}$ and $L_T^{-1} \propto \Delta W$, we recover the form of Rice-scaling. The linear scaling of torque with gradients is consistent with experimental observations [152, 153] and global gyrokinetic simulations of ITG [163] and collisionless TEM [164, 165] modes. The main limitation of this model is the ρ_* scaling, which the experimental findings of [155] show no dependence on. These results may have severe implications for ITER's operation. In the 'Solomon-cancellation' experiment [166], a net on-axis counter-NBI torque was used to cancel the pedestal co-intrinsic torque to yield a flat rotation profile right across the minor radius. It is speculated that in the electron cyclotron-heated H-mode, the counter-torque associated with the excitation of ∇T_e-driven TEM [167, 168] could cancel the pedestal co-torque at the $q = 2$ surface[6]. The locking of a 2/1 neoclassical tearing mode island to the wall allows it to grow rapidly, likely ending the discharge with a disruption [169]. Indeed, understanding intrinsic rotation and the impact of rotation on L-H power threshold and suppression of turbulence, have been identified by the ITPA Transport and Confinement topical group as key areas [170].

[5] An intuitive understanding of the physics can be gained from an analogy with the gyroscopic-stabilisation of a spinning top. The toroidally rotating plasma has an angular momentum about the central column; distortions introduced by the kink-modes alter this momentum, which the spinning plasma opposes.

[6] The 'flat' rotation profile of Solomon, when core-counter-NBI cancels the pedestal-co intrinsic torque, must be contrasted with the formation of a 'connection-layer' when counter-core and co-pedestal intrinsic torques interact [161].

3.4 Dynamics of pedestal formation

Since the H-mode is so rich with physics, while being critical to the success of ITER, it is worthwhile to understand the dynamics of the pedestal evolution here (in particular, the high performance Type-I ELMing discharges). In most tokamaks such as MAST, NSTX, Alcator C-Mod and DIII-D [111, 171], the pedestal forms through an interplay between two distinct physical mechanisms (refer Fig. 3.6 for a schematic):

(a) Immediately following a large-ELM, small-scale microinstabilities responsible for turbulent transport, such as the Kinetic Ballooning Mode (KBM), constrain the pressure-gradient, allowing the pedestal to widen (Fig. 3.5) [113].

(b) The pedestal keeps expanding radially inwards until it encounters the global stability limit of the ideal-MHD peeling-ballooning mode [132]. For small pedestal widths, the global MHD mode is unable to 'fit' inside the pedestal, and this has a stabilising influence on the mode [172], allowing for a higher threshold in the gradient. (Once the mode is able to fit inside, increasing the pedestal width should have no further bearing on the mode's stability.)

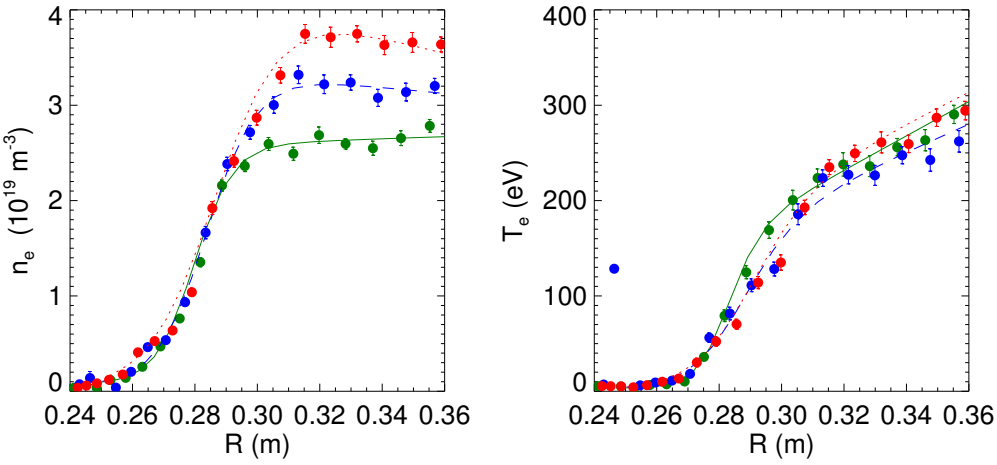

Figure 3.5: Plot (a) shows the evolution (green → blue → red) of the density profile in between two Type-I ELMs on MAST, with (b) showing the corresponding temperature evolution. The pressure pedestal formation therefore follows (a). The plasma core is to the right in both figures. (Reproduced from [111] with permission from the American Physical Society.)

The EPED model [173] uses these constraints to predict the pedestal height and width at the onset of a Type-I ELM. With MHD ballooning and toroidal drift modes central to the pedestal dynamics, it is important that we understand the physics of their onset. The 'linear ballooning formalism' is an extremely useful tool towards

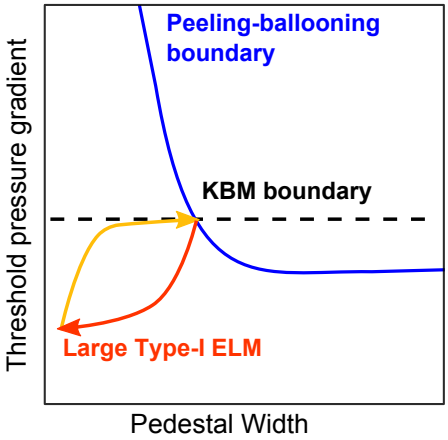

Figure 3.6: Illustration of the EPED model (see text for discussion).

this study[7].

3.5 Ballooning framework

Toroidal drift modes and MHD ballooning modes are strongly localised about rational flux surfaces (minimising field-line bending), with the rational surface spacing given by $\Delta = (nq')^{-1}$ (n is the toroidal mode number and q' is the radial derivative of the safety factor profile). For high-n modes, $\Delta \ll L_{eq}$ with L_{eq} characterising the length-scale over which equilibrium profiles vary. The formalism exploits this approximate invariance of rational surfaces, and expands in the small parameter Δ/L_{eq} to reduce a system describing a 2D perturbation (in r and θ) to two uncoupled 1D equations (in the field-aligned coordinate η (related to θ) and the radial coordinate r). To the lowest order, the perturbations on adjacent rational surfaces are decoupled and evolve independently of each other. The problem is then of one along the field-line η and yields the *local* eigenvalue $\lambda(r, \eta_0)$, together with the mode structure. At this level both η_0 (an arbitrary phase offset) and r are free parameters and typically chosen to yield the most unstable mode. But the higher-order theory imposes constraints (section 3.5.3). Before discussing this, we must make an important distinction between MHD ballooning and toroidal drift modes.

3.5.1 MHD ballooning modes

Ideal MHD is Hermitian [174] and the eigenvalue $\lambda = \gamma^2(r, \eta_0)$ is real, where γ is the growth rate. Further, the stability of these eigenmodes affect the entire plasma. Therefore, if an unstable mode was to exist, all we need to do is pick r and η_0 that maximises the growth rate. To see this, Taylor-expand the local eigenvalue in the neighbourhood of r_0 where γ^2 is maximised (Fig. 3.7): $\lambda = \lambda_0(r_0, \eta_0) + \lambda_r(r_0, \eta_0)(r -$

[7]While the linear theory deals with the instability triggers, nonlinear theory is instrumental in determining the consequences of the instability onset.

$r_0) + \lambda_{rr}(r_0, \eta_0)(r - r_0)^2/2 + \ldots$ (here λ_r and λ_{rr} are the first and second radial derivatives). To obtain the maximum growth rate, one requires $\lambda_r(\eta_0 = \hat{\eta}) = 0$, where $(\partial\lambda_r/\partial\eta_0)|_{\eta_0=\hat{\eta}} = 0$. For ballooning modes in an up-down symmetric equilibria, the instability drive is maximised at the outboard-midplane, thus $\hat{\eta} = 0$ typically satisfies the constraint. Under these assumptions the global eigenvalue is accurate to the local limit within $\mathcal{O}(1/n)$ [172], so the local solution is a very good description of the full 2D problem.

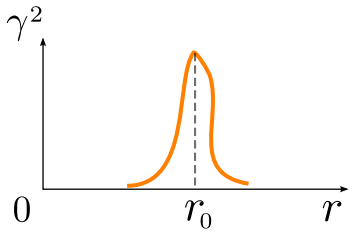

Figure 3.7: Cartoon of the ideal-MHD ballooning mode growth rate variation with radius.

3.5.2 Toroidal drift modes

For toroidal drift modes the situation is a little more subtle due to the eigenvalue being complex: $\lambda = \omega_0(r, \eta_0) + i\gamma_0(r, \eta_0)$. Here ω_0 and γ_0 are the frequencies and growth rates of the linear perturbations for different r and η_0. A treatment similar to MHD cannot be uniquely followed since the stationary point condition $\lambda_r(\eta_0 = \hat{\eta}) = 0$ is not trivially satisfied. This is illustrated in Fig. 3.8. Consider the pressure pedestal of H-mode. The instability drive is expected to be maximum somewhere inside the pedestal where the profile gradients are the steepest. There is no apparent reason why the frequency should peak at the same radial location (Fig. 3.8a). Now from the

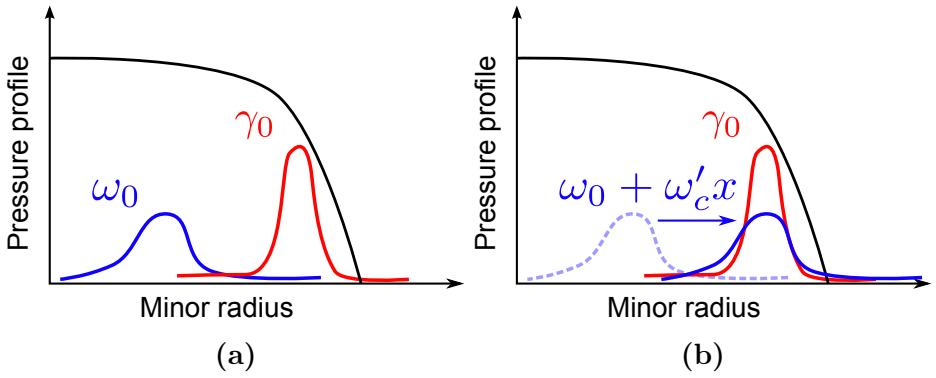

Figure 3.8: Schematic of the pressure pedestal demonstrating why (a) the complex local eigenvalue is not necessarily stationary at the same radial location, and (b) how a linearly sheared flow profile can transiently make this possible.

force balance equation, it can be seen that the pressure gradient is associated with equilibrium toroidal flows. A Doppler shift associated with the linearly sheared flow $\omega' x$ ($x = r - r_0$, with r_0 our reference frame) could shift the frequency to transiently

align the peaks in γ_0 and ω_0 (Fig. 3.8b). Note that the peaks only align in the presence of a *critical* flow-shear ω'_c. Only now could a treatment similar to the one adopted for MHD ballooning modes be followed. Therefore, a higher-order theory that treats general radial profile variations, is desirable.

3.5.3 Higher-order theory: two branches

The lowest order treatment yields the mode structure along the field-line η and the local eigenvalue $\lambda(r, \eta_0)$, with both r and η_0 being free parameters. Moving on to the next order, the problem becomes one in radius: the theory uses the radial variation in $\lambda(r, \eta_0)$ to construct the *global* mode structure and global (true) eigenvalue. Depending on the profiles, the parameter η_0 is now predicted by theory, and is essentially the poloidal location where the most unstable mode sits. When applied to toroidal drift modes (ITG, KBM etc.), two distinct classes of global instabilities have been identified by theory [175, 176, 177, 178]: the *General Mode (GM)* and the *Isolated Mode (IM)*. The IM exists in the special situation when $\lambda(r, \eta_0)$ has a stationary point in r and η_0 (Fig. 3.8b). This is closely related to the *local* solution obtained for ideal MHD. In typical up-down symmetric equilibrium this mode will balloon close to the outboard-midplane (i.e. $\hat{\eta} = 0$) and have a strong growth rate, $\gamma \sim \max[\gamma_0]$. More general (e.g. shaped) equilibria can result in non-zero values of $\hat{\eta}$. The GM on the other hand does not have any such constraint on $\lambda(r, \eta_0)$ and is therefore always accessible (Fig. 3.8a). For a circular cross-section, it will typically peak at the top/bottom of the poloidal plane, and the growth rate is obtained by averaging $\lambda(r, \eta_0)$ over η_0 [177, 179, 180] (λ is periodic in η_0). The GM is therefore more stable than the IM. Finally, global eigenvalue simulations [178, 181] have shown that the two branches can transition into one another in the presence of a critical flow-shear.

3.6 Project motivation

Global turbulence codes that treat profile variations cannot, in general, distinguish between the two branches (IM and GM) without knowledge of the local eigenvalue $\lambda(r, \eta_0)$. However, and as we shall see in Chapter 5, knowledge of local solutions does enable us to efficiently[8] reconstruct the global eigenmode [181]. The thrust of turbulence modelling in fusion research has been to understand the different microinstabilities responsible for transport and how the associated losses could be minimised. For any given set of (typically *static*) equilibrium profiles, global codes are employed to predict the linear instability threshold and the nonlinear fluxes, without needing

[8]Solving multiple 1D ordinary differential equations to map $\lambda(r, \eta_0)$ can be done independently in the $r - \eta_0$ plane. The subsequent step of calculating the global eigenvalue from $\lambda(r, \eta_0)$ is effectively a one-step Fourier integral.

to make a distinction between the two branches. However, some exciting physics ideas do emerge when considering the dynamics of the IM and GM and how the two branches can transition into one another as the profiles *evolve*. This research aims to address three key areas.

3.6.1 Dynamics of eigenmode formation

The global mode comprises of coupled Fourier modes, each of which evolve on rational flux surfaces. There are two time-scales of significance: firstly, how quickly do the neighbouring local modes couple with the right amplitudes and phases to establish the global mode structure; and secondly, how long does it take the local modes to have significant amplitude to drive the system nonlinear. If by the latter time period the global modes have not formed, the plasma cannot make a distinction between the IM and GM, and these structures should have no bearing on the nature of turbulence (e.g. GM driven turbulent transport is likely to be most virulent at the top/bottom of the poloidal cross-section). This could additionally have important implications for local flux-tube turbulence simulations, which cannot make a distinction between the IM and GM, and take the more unstable IM to drive growth in the linear phase leading up to saturation.

3.6.2 A model for small-ELMs?

Assuming that the global modes can form sufficiently quickly, thereby allowing them to influence the nonlinearly saturated states, their dynamics can form the basis of a new model for small-ELMs. This is illustrated using Fig. 3.9. Based on Fig. 3.8a, we argue that the gradient at which the KBM holds the pedestal is one associated with the GM (KBM-GM). Since the KBM-IM is more violent, we posit that there exists a lower critical gradient for the onset of this branch. However, due to the strict stationary point constraint on $\lambda(r, \eta_0)$, the plasma is normally unable to access the IM. Type-I ELMs occur when the critical flow-shear needed to trigger the KBM-IM is outside the trajectory of the evolving pedestal (red-star). Plasma shaping can move the peeling-ballooning boundary or NBI can influence the flow-shear to make this lie in the pedestal trajectory (green-star). At this point the plasma sees the IM much above its threshold, triggering a sudden increase in growth rate and, likely, an associated burst in transport. Furthermore, the rapid adjustment of profiles would terminate the crash and re-establish the GM, limiting the energy released, and allowing the cycle to repeat. Indeed, there is experimental evidence of NBI [182] and strong shaping [183] triggering grassy-ELMs on JT-60U. Of course, a key question is whether the GM-IM-GM transition *does in fact* drive a burst in transport. This would require nonlinear simulations well outside the scope of present linear studies. Here we only seek to address the time-scales associated with the aforementioned

GM-IM-GM dynamics.

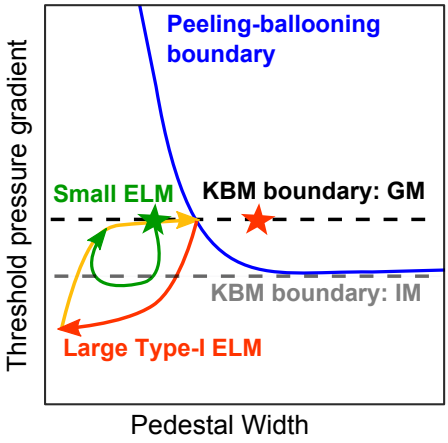

Figure 3.9: Sketch illustrating extensions to the standard EPED-type model of Fig. 3.6 to accommodate small-ELMs (see relevant text for discussion). The 'stars' indicate the critical flow-shear needed to access the IM which may (green) or may not (red) be encountered by the evolving pedestal constrained at the critical gradient of GM.

3.6.3 Towards intrinsic rotation modelling

There is another important piece of physics to consider: the effect the mode structure would have on the flow, through Reynolds stresses [184] for example. Following [185], it is intuitive that a radially-outward-directed 'effective gravity', experienced by all toroidal plasmas, would cause any poloidally asymmetric density (and through the Boltzmann relation, electrostatic potential) imbalance to align with the effective-gravity. Though magnetic-pumping[9] may impede such flows [186], sufficiently strong poloidally asymmetric particle/momentum sources may overcome this damping [187]. If such an effect was to be significant, the more *general* asymmetric GM would not be stable according to this picture, whereas the *special* IM would be! References [188, 189] further conclude that asymmetric modes such as the GM are expected to generate a significant torque compared to the symmetric IM. This motivates the following questions: (a) does the intrinsic torque generated by the GM drive the mode towards the IM structure?; (b) could a balance between the intrinsic and externally (e.g. NBI) driven torque influence the stability of IM/GM solutions?; and (c) is there a correlation between the torque associated with these linear mode structures and the nonlinearly saturated flows? Answering the final question again requires nonlinear simulations and cannot be addressed here.

Note that the equilibrium profiles set the critical flow-shear for a GM-IM transition. If the GM torque drives towards an IM (the latter not expected to produce any significant torque), then this can tell us about the flow-shear that is produced.

[9]When a 'flux-tube' of plasma gets convected poloidally from the outboard to the inboard side, the compression of magnetic field-lines causes more collisions. These collisions dissipate the kinetic energy of the poloidal rotation as heat, damping such flows.

We posit that global modes sitting on resonant surfaces would drive torques and set boundaries on the neighbouring modes; integrating across the minor radius with global boundary conditions (e.g. core NBI and scrape-off layer flows) would give the plasma rotation profile. This could potentially provide a handle on torque profile control using shaping (for example) to modify the global mode structure. There is evidence of plasma shaping strongly influencing the intrinsic toroidal rotation profile on TCV [190].

3.7 Summary

In this chapter we looked at microinstabilities in a torus and how flow-shear may reduce the associated turbulent transport. High enough flow-shears can lead to turbulence suppressed regimes. Such regimes are accompanied by edge plasma eruptions and spontaneous rotation, driven by the steep profile gradients that form. Both areas are crucial to the success of ITER and yet we lack robust predictive capabilities to guide ITER's operation. The global theory of microinstabilities could provide a firm physics basis to build this capacity. For *all* toroidal microinstabilities, two distinct branches are predicted: an asymmetric yet generally accessible branch (General Mode), and a strongly unstable, symmetric, although generally inaccessible branch (Isolated Mode). The working hypotheses are (1) a transition between the relatively benign and violent branch could drive a burst of transport and (2) the asymmetric accessible branch could drive intrinsic torque. In Chapter 4 we shall introduce the new initial value code and present benchmarks. The code will be used to explore the global mode dynamics in Chapter 5, in particular the GM-IM-GM transition, from the point of view of the ELM problem. In Chapter 6, the more self-consistent problem accounting for the feedback of the mode on the flow is explored.

Chapter 4

A time-dependent code to study toroidal drift modes

From the previous chapter it is amply clear that, in order to address the questions on small-ELM and intrinsic rotation modelling, we need a global initial value code that permits profile evolution. The following sections describe the development and testing of this new code to study toroidal drift modes.

4.1 Physics model

To explore the dynamics of the GM-IM-GM transition as flow-shear evolves, we require a physics model that captures the essential features of toroidicity and radial profiles generic to all toroidal micro-instabilities. The global toroidal fluid model of [191] contains this physics. This model is derived from the gyrokinetic equation in the fluid limit of small Larmor radius for a large aspect-ratio circular cross-section tokamak. It is electrostatic with adiabatic electrons, and describes both ITG and electron drift modes. The equation for the perturbed potential $\tilde{\phi} = \phi_1(x,\theta)\exp(\mathrm{i}n\varphi)$ in this model is

$$\left[\rho_s^2\frac{\partial^2}{\partial x^2} - k_\theta^2\rho_s^2 - \frac{\sigma^2}{\Omega^2}\left(\frac{\partial}{\partial\theta} + \mathrm{i}nq\right)^2 - \frac{2\epsilon_n}{\Omega}\left(\cos\theta + \mathrm{i}\frac{\sin\theta}{k_\theta}\frac{\partial}{\partial x}\right) - \frac{\Omega-1}{\Omega+\eta_s}\right]\phi_1(x,\theta) = 0. \quad (4.1)$$

Here, the first two terms containing ρ_s are due to finite Larmor radius effects; the third term is the ion-sound term and encapsulates the parallel dynamics; the fourth term arises due to the toroidal curvature; and the final eigenvalue term captures the adiabatic electron response. The various equilibrium parameters used are as follows (prime denotes a radial derivative): $\rho_s^2 = \rho_i^2\tau$, where ρ_i is the ion Larmor radius and $\tau = T_e/T_i$ the electron to ion temperature ratio; $\epsilon_n(r) = L_n/R$ is the density scale length $L_n(= n_s/n_s')$ normalised to the plasma major radius R; $\sigma(r) = \epsilon_n/(qk_\theta\rho_s)$; $k_\theta = m_0/r$ is the poloidal wavenumber, with $q(r_0) = m_0/n$ and n the toroidal mode number; $q = q(r_0) + q'x$ is the safety factor profile with $x = r - r_0$ and r_0 some

reference rational surface; $\eta_s = (1 + 1.5\eta_i)/\tau$, where $\eta_i(r) = n_s T_i'/T_i n_s'$ is the ITG mode drive; and finally, $\Omega = \omega + i\gamma$ is the global mode frequency normalised to the electron diamagnetic frequency ω_{*e}.

In eqn. 4.1, balancing the eigenvalue term with the rest (which are small) requires either $\Omega \simeq 1$ or $\eta_s \gg 1$. The ordering $\Omega \simeq 1$ gives rise to the electron drift mode, whereas the condition $\eta_s \gg 1$ corresponds to the ITG branch [35] - the latter is the focus of this work. Note that because $\eta_s \gg 1$, we are constrained to consider only strongly unstable modes. This model is, of course, a great simplification of the full ITG mode physics, which requires a gyrokinetic or gyrofluid treatment to take proper account of drift-resonances, and should also include electromagnetic effects particularly at high β [117]. That said, the applicability of the gyrokinetic framework itself rests on the smallness of the parameter ρ_s/L – an ordering that may well break down at the edge where the ELM dynamics are of interest. This constrains us to the study of microinstabilities whose scale-lengths do not violate the gyrokinetic ordering. Nevertheless, since we are more interested in the dynamics of the two toroidal eigenmode categories (IM and GM) as opposed to the details of any particular micro-instability, the use of this model, shown previously to analytically capture the two branches, is justified [192].

4.1.1 Cylindrical limit

By Fourier-expanding eqn. 4.1 with $\phi_1(x,\theta) = \sum_m \phi_m(x)\exp(-im\theta)$, it can be shown that each Fourier harmonic satisfies:

$$\left[b\hat{s}^2\frac{\partial^2}{\partial y^2} - b + \left(\frac{\sigma}{\Omega}\right)^2 (m' - y)^2 - \frac{\Omega - 1}{\Omega + \eta_s}\right]\phi_m = \frac{\epsilon_n}{\Omega}\sum_{\pm}\left[1 \pm \hat{s}\frac{\partial}{\partial y}\right]\phi_{m\pm1}. \tag{4.2}$$

Here $b = k_\theta^2\rho_s^2$, $m' = m - m_0$, $nq' = k_\theta\hat{s}$ ($\hat{s} = rq'/q$ is the magnetic-shear), and we have further defined the dimensionless radial variable $y = nq'x$ (note y takes integer values at rational surfaces). This form also explicitly highlights the coupling of mode m with $m\pm1$ modes, which is a result of the curvature drift term. Dropping the toroidal coupling terms on the right hand side of eqn. 4.2, we obtain the cylindrical branch of the ITG mode. Next defining $m' - y = z$, we have

$$\left[b\hat{s}^2\frac{\partial^2}{\partial z^2} + \frac{\sigma^2 z^2}{\Omega^2} - \hat{\lambda}\right]\Psi(z) = 0 \tag{4.3}$$

where

$$\frac{\Omega - 1}{\Omega + \eta_s} + b = \hat{\lambda}\,. \tag{4.4}$$

Defining $z = t/\alpha$, we derive

$$\Phi''(t) + \left[\frac{\sigma^2 t^2}{\Omega^2\alpha^4(\hat{s}\sqrt{b})^2} - \frac{\hat{\lambda}}{(\alpha\hat{s}\sqrt{b})^2}\right]\Phi(t) = 0\,. \tag{4.5}$$

Here $\Psi(z) = \Psi(t/\alpha) = \Phi(t)$. Referring to Appendix B.1, we see that it is possible to write eqn. 4.5 in an analytically solvable form by choosing α such that

$$\frac{\sigma^2}{\Omega^2\alpha^4(\hat{s}\sqrt{b})^2} = -1\,. \tag{4.6}$$

This yields the expression

$$\Phi''(t) + \left[-t^2 - \frac{\hat{\lambda}}{(\hat{s}\sqrt{b})^2}\left(\frac{\Omega\hat{s}\sqrt{b}}{\pm\mathrm{i}\sigma}\right)\right]\Phi(t) = 0\,. \tag{4.7}$$

Equation 4.7 is solved by the form $\Phi(t) = \exp(-t^2/2)H_k(t)$, where H_k is the order-k Hermite polynomial. We choose the positive sign in front of σ to give a decaying form for the electrostatic potential. Equation B.3 is again used to determine the order of the Hermite polynomial:

$$-\frac{\hat{\lambda}}{(\hat{s}\sqrt{b})^2}\left(\frac{\Omega\hat{s}\sqrt{b}}{\mathrm{i}\sigma}\right) = (2k+1)\,. \tag{4.8}$$

Rearranging into a quadratic form for the complex mode frequency Ω:

$$\Omega^2(1+b) + \Omega\left(b\eta_s - 1 + (2k+1)(\mathrm{i}\sigma\hat{s}\sqrt{b})\right) + (2k+1)\left(\mathrm{i}\sigma\hat{s}\sqrt{b}\eta_s\right) = 0\,. \tag{4.9}$$

Motivated by the choice of parameters in ref. [178], eqn. 4.9 is solved numerically for the values $m_0 = 90$, $n = 50$, $\hat{s} = 2.0$, $b = 0.1$, $\epsilon_n = 0.03$ and a range of η_s and τ. A scan is also performed in the k space to identify the most unstable solution. The result is plotted in Fig. 4.1. Clearly, for these parameters the most unstable mode is not the fundamental. From the quasi-linear mixing-length estimate (eqn. 3.5), it is clear that diffusivity depends both on the growth rate and radial wavenumber of the linear instability. In this situation, the very high-order modes - which are radially extended and strongly unstable - are expected to dominate transport. A more rigorous kinetic treatment (including ion Landau damping) restricts the mode number k that can exist in the plasma [193].

4.2 Numerical modelling

The eigenmode eqn. 4.2 was first solved numerically for arbitrary profiles by Dickinson [178]. Here we develop a time-dependent system. But before describing the algorithm, let us consider the role of sheared flows.

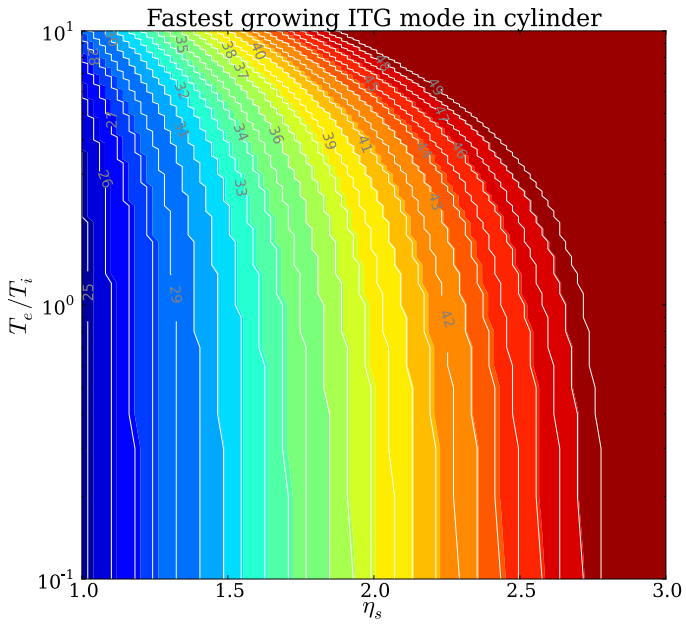

Figure 4.1: Contour plot showing mode numbers of the most dominant cylindrical eigenmodes (labelled inset), obtained by solving eqn. 4.9.

4.2.1 Incorporating the effect of flow-shear: Doppler shift

Sheared perpendicular ($v'_\perp$) and parallel ($v'_\parallel$) flows are ubiquitous to the edge pedestal. In our analysis, we consider the toroidal flow v_ϕ as dominant due to effects such as NBI driven toroidal momentum input and strong neoclassical damping of poloidal flows [186]. If the flow is much less than the sound speed, as we shall assume, then the centrifugal and Coriolis forces can be neglected. We next set $v_\theta = 0$, and this constraint allows us to relate v_ϕ with $v_\parallel$ and $v_\perp$. The perpendicular $E \times B$ shear provides a stabilisation mechanism [194] and also convects the ballooning modes in the poloidal angle [195]. If the toroidal flow varies on the equilibrium scale, the shear between adjacent rational surfaces will be of $\mathcal{O}(1/n)$. The Doppler shift from the convective derivative $\mathbf{v}_\phi.\nabla = -in v_\phi/R$, however, has an $\mathcal{O}(1)$ effect on the ITG growth rate in the vicinity of the GM-IM-GM transition. As we seek to explore the dynamics of this transition, it is appropriate to neglect the parallel velocity gradient drive in comparison to the ITG drive [196]. Then, toroidal flow-shear is included in our model through the transform $\Omega \to \Omega + n\Omega'_\phi x$ [197], where Ω'_ϕ is a real number and sets the flow-shearing rate (note that this definition implies the toroidal rotation frequency $\Omega'_\phi x$ is also normalised to ω_{*e}). We work in the reference frame where the rational surface of interest at $r = r_0$ is at rest.

4.2.2 A time-dependent formalism

We start with eqn. 4.2 and perform the transformation $\Omega \to \Omega + f$, where $f = \gamma_E y$ is the Doppler shift due to the flow-shear. We further define three new fields $G_m = \Omega\phi_m$,

$H_m = \Omega G_m$ and $F_m = \Omega H_m$ for mathematical convenience. This allows eqn. 4.2 to be written in a differential-difference form

$$\hat{\alpha} F_m = -\left(\hat{\Delta}\phi_m + \hat{\beta} H_m + \hat{\Gamma} G_m\right) + \chi\epsilon_n[\kappa_H + \kappa_G(2f + \eta_s) + \kappa_\phi(f^2 + \eta_s f)] \,. \tag{4.10}$$

Here we have introduced the fictitious parameter χ that can be set to zero to neglect toroidal coupling. The spatial operators acting on the fields in the presence of flow-shear are defined in table 4.2 (note $G_\pm$ and $H_\pm$ follow $\phi_\pm$), which are related to the operators in the absence of flow-shear, table 4.1. Next transforming $\Omega \to \mathrm{i}\partial/\partial t$, we

Table 4.1: Spatial operators in the absence of plasma flow.

α	$b\hat{s}^2\partial_y^2 - (b+1)$
β	$\eta_s(b\hat{s}^2\partial_y^2 - b) + 1$
Γ	$\sigma^2(m' - y)^2$
Δ	$\eta_s\sigma^2(m' - y)^2$
$\phi_\pm$	$\phi_{m+1} \pm \phi_{m-1}$

Table 4.2: New operator definitions upon the incorporation of flow-profile f.

$\hat{\alpha}$	α
$\hat{\beta}$	$\beta + 3f\alpha$
$\hat{\Gamma}$	$\Gamma + 2f\beta + 3f^2\alpha$
$\hat{\Delta}$	$\Delta + f\Gamma + f^2\beta + f^3\alpha$
κ_ϕ	$\phi_+ + \hat{s}\partial_y\phi_-$
κ_G	$G_+ + \hat{s}\partial_y G_-$
κ_H	$H_+ + \hat{s}\partial_y H_-$

see

$$\frac{\partial}{\partial t}\begin{pmatrix} \phi_m \\ G_m \\ H_m \end{pmatrix} = -\mathrm{i}\begin{pmatrix} G_m \\ H_m \\ F_m \end{pmatrix}, \tag{4.11}$$

which we solve using the 4^{th}-order Runge-Kutta scheme, with F_m calculated consistently at every time-step by inverting eqn. 4.10 (see Appendix C for details). An instantaneous complex mode frequency

$$\Omega_m(t) = \mathrm{i}\frac{\partial \ln \phi_m}{\partial t} \tag{4.12}$$

can be associated with each individual Fourier mode, evaluated at the rational surface where $q(r_m) = m/n$, i.e. at $y = m'$. Once an eigenmode is established, we expect $\Omega_m(t)$ to be the same for all m and independent of time.

4.3 Global growth rate from electrostatic potential

For an eigenmode formulation we may write:

$$\phi(x,\theta,t) = e^{-\mathrm{i}\Omega t}\sum_m \phi_m(x)e^{-\mathrm{i}m\theta} \tag{4.13}$$

$$= e^{-\mathrm{i}\Omega t}\hat{\phi}. \tag{4.14}$$

Multiplying through by the complex-conjugate ϕ^* gives $|\phi|^2 = e^{2\gamma t}|\hat{\phi}|^2$, where

$$|\hat{\phi}|^2 = \left(\sum_m \phi_m e^{-\mathrm{i}m\theta}\right)\left(\sum_k \phi_k^* e^{\mathrm{i}k\theta}\right) \tag{4.15}$$

$$= \left(\sum_m \phi_m\phi_m^*\right) + \left(\sum_m\sum_{k\neq m} \phi_m\phi_k^* e^{-\mathrm{i}\theta(m-k)}\right). \tag{4.16}$$

Integrating over the poloidal cross-section $\langle ...\rangle_\theta$ provides

$$\left\langle|\hat{\phi}|^2\right\rangle_\theta = 2\pi\sum_m |\phi_m|^2.$$

Further integrating in x, we can define the quantity

$$\zeta_\phi = \left\langle|\phi|^2\right\rangle_{\theta,x}^{1/2} = e^{\gamma t}\sqrt{2\pi}\sqrt{\sum_m\int_x |\phi_m|^2\mathrm{d}x} \quad , \tag{4.17}$$

from which we derive the global growth rate:

$$\gamma = \frac{1}{\zeta_\phi}\frac{\partial\zeta_\phi}{\partial t} \quad . \tag{4.18}$$

The advantage of defining the global growth rate in this way is that (a) it is insensitive to where the global mode peaks in x and θ, and (b) it factors in the amplitude of all constituent Fourier harmonics; therefore, the peripheral harmonics which do not have significant amplitudes compared to the dominant harmonics, do not affect the global growth rate calculations sizeably. Further from $G_m = \Omega\phi_m$,

$$\sum_m G_m \mathrm{e}^{-\mathrm{i}m\theta} = \Omega\sum_m \phi_m \mathrm{e}^{-\mathrm{i}m\theta} \, . \tag{4.19}$$

Multiplying eqn. 4.19 with its complex-conjugate, and performing a similar integral-sum that enabled us to derive eqn. 4.17, provides:

$$|\Omega| = \sqrt{\gamma^2+\omega^2} = \frac{\zeta_G}{\zeta_\phi} \, , \tag{4.20}$$

from which we may derive the global mode frequency ω. It is seen that the negative root of ω matches the right solution.

4.4 Benchmarks

To test the new global initial value code, several benchmarks were performed. First, insensitivity of the converged eigenvalues and mode structures to the initial conditions and numerical parameters were verified. For profiles held fixed in time, the growth rate and mode frequency of the time-evolving global mode is seen to converge (Fig. 4.2) as expected from an eigenmode treatment. To quantify this, the converged eigenvalue was first compared against the analytic cylindrical solution of eqn. 4.9, and then with the full 2D global eigenvalue code developed by Dickinson [178].

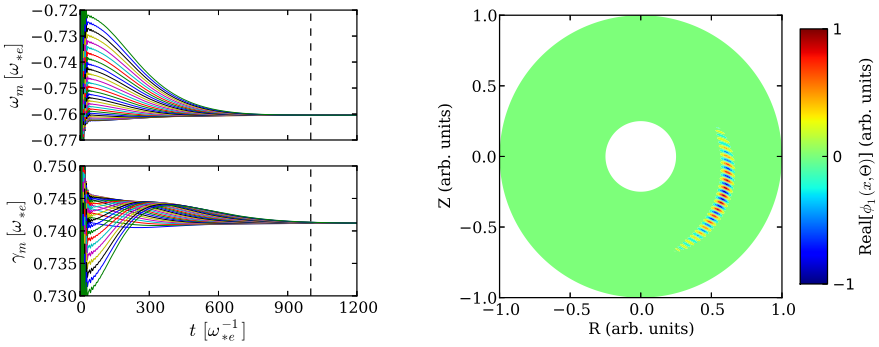

(a) **(b)**

Figure 4.2: (a) shows the evolution of $\Omega_m(t) = \omega_m(t) + \mathrm{i}\gamma_m(t)$ (eqn. 4.12), where each line is a different poloidal harmonic m. (b) shows the real part of the eigenfunction in the poloidal plane, corresponding to the time indicated by the dashed vertical line in (a). We note that the global mode peaks at $r_0/a = 0.965$; all our 2D plots have been scaled to help clearer visualisation of the mode structure.

4.4.1 Cylindrical limit

Neglecting toroidal coupling (setting $\chi = 0$ in eqn. 4.10), the reduced initial-value code was run with the following parameters: $b = 0.1$; $\tau = 10.0$; $\eta_s = 1.0$; $\hat{s} = 2.0$; $q = 1.8$; $n = 50$; $m_0 = 90$; $\gamma_E = 0$; and ϵ_n was varied in the range shown in Fig. 4.3. The choice of parameters at this stage is purely to do with performing validations in a regime where different harmonics are progressively unstable. This provides a better handle on running of the code. As evident, the percentage difference between the analytics and numerics is $0.01 - 0.1\%$ everywhere, except for very low values of ϵ_n. As ϵ_n is decreased further, this difference is much higher. This observation can be explained with the help of Figs. 4.3a and 4.3b. At low values of ϵ_n, the complex mode frequency of the most unstable mode is comparable to other harmonics and, consequently, Ω_{num} receives significant contribution from a mixture of harmonics for a specified run-time. With time, Ω_{num} is dominated by the single most unstable mode and the agreement becomes better.

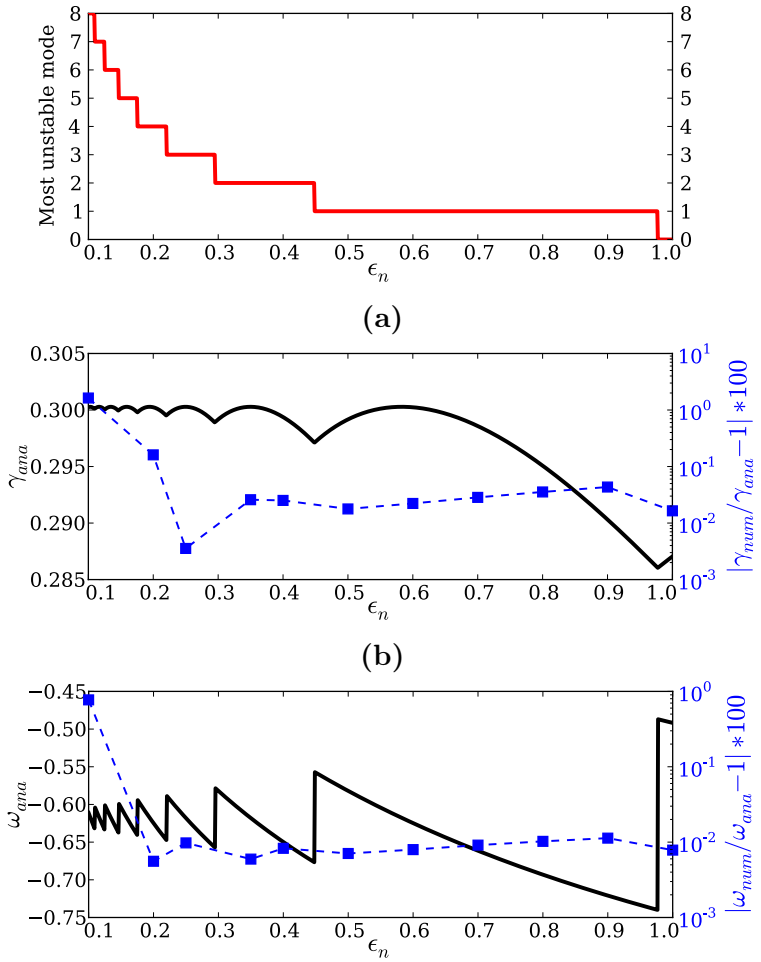

Figure 4.3: The three plots look at (a) the most unstable ITG mode number k in the cylindrical limit, (b) the corresponding growth rates and (c) the mode frequencies of the converged solutions. The analytical frequencies and growth rates are plotted in black, whereas the percentage-difference between the analytical and numerical solutions are given by the blue squares.

4.4.2 Full toroidal system

Next, comparisons were made with the full 2D eigenvalue code of Dickinson [178] (Fig. 4.4) with the same parameter set used for the cylindrical benchmark. The converged Ω_{ini} from the initial-value code was used as a guess for the eigenvalue code and Ω_{eig} was calculated. Differences in the range of $0.01 - 0.25\%$ indicate that the two codes are in very good agreement. A final validation was performed with the inclusion of flow-shear around the GM-IM-GM transition point (with parameters defined in section 4.5). The agreement is likewise very good. This result is deferred to the next chapter, after the global modes have been introduced, though one may refer to Fig. 5.3 for completeness.

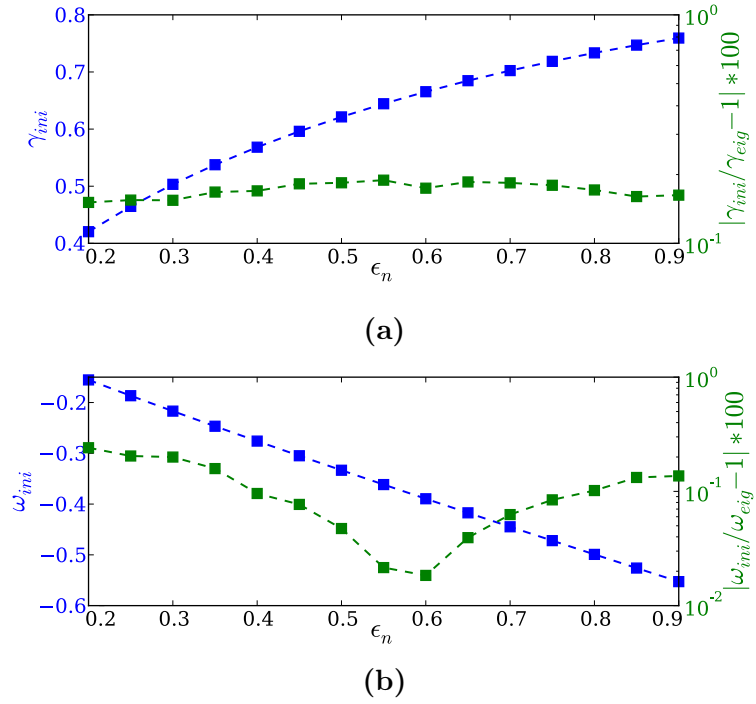

Figure 4.4: The two plots show the (a) growth rate and (b) mode-frequency of the global toroidal eigenmode as a function of ϵ_n. Results from the new initial-value code are plotted in *blue* and the percentage difference upon comparisons with the eigenvalue code of [178] are in *green*.

4.5 Equilibrium parameters

Table 4.3 lists the physical parameters used in subsequent simulations (deviations from these are mentioned where appropriate). In addition, the ITG drive η_s has a radial profile of the form $\eta_s = \eta_g(1.0 - \eta_c x^2)$, with $\eta_g = 2.0$, $\eta_c = 1062.5$, and 40 Fourier-modes on either side of m_0 are found to be sufficient for convergence. For

Table 4.3: Equilibrium parameters used in simulations.

a	R	r_0/a	$k_\theta\rho_i$	$\hat{s}$	ϵ_n	τ	q	n	m_0	γ_E
0.5	2.5	0.965	0.2	25.0	0.08	1.0	1.4	50	70	-0.006 to 0.006

any given set of parameters, several radial harmonics of an eigenmode are simultaneously unstable. The initial-value code becomes dominated in time by the most unstable harmonic. To find the dominant linear mode more rapidly, we have chosen parameters where the most unstable harmonic has a significantly higher growth rate than the other modes, and is also close to the fundamental radial harmonic (further relaxing the grid resolution needed to resolve the finer spatial structures associated with higher harmonics). This means the solution will rapidly converge to the dominant mode from initial conditions, allowing for numerical efficiency and easy comparison with earlier eigenmode solutions to eqn. 4.1. Another guiding influence

for our parameter choice is to ensure that the same eigenmode is the most unstable as the flow-shear is varied through the GM-IM-GM transition. That said, and with small-ELM dynamics in mind, our parameters are relevant to those typically found in the pedestal.

4.6 Summary

In this chapter, the development of a new global initial value code[1] was discussed, which can capture the dynamics of the GM and IM branches as profiles evolve[2]. The physics model used describes the fluid-ITG mode in a circular cross-section geometry. The choice of this model allows comparisons with an earlier eigenvalue code, and various benchmarks have been successfully performed. In the next chapter, after discussing the theory of global eigenmodes, we will consider the dynamics associated with the GM/IM formation and transition, in the presence of an externally imposed flow-shear.

[1]Solutions for typical parameters converge on the order of hours. A Message Passing Interface (MPI) based parallelisation provides speed-up in some cases.

[2]The code is available from the University of York's Data Catalogue [198].

Chapter 5

The response of toroidal drift modes to profile evolution

In this chapter, we provide an intuitive overview of ballooning instabilities, followed by a mathematical description of the framework used to obtain the two generic (Isolated and General) branches of toroidal drift-ballooning instabilities. The new initial-value fluid-ITG code is then used to explore the dynamics of these global modes in the presence of evolving equilibrium sheared flows.

5.1 Ballooning modes: an intuitive overview

Based on reference [199], a simple physical description of the effect of flow on ballooning modes is presented. MHD ballooning instabilities require a combination of high plasma pressure gradient and magnetic field curvature. Since bending of magnetic field lines in a plasma requires energy, and is therefore stabilising, the most unstable modes tend to minimise field line bending. Let us introduce a $q = m/n = 10/5$ plasma wave to the system (Fig. 5.1); as the toroidal and poloidal directions are periodic, we must fit a whole number of wavelengths in these directions. Furthermore, if the crests of the wave align with the magnetic field lines, as the wave amplitude grows, it will just raise the field line as a whole without bending it. As we move away from the $q = 2$ surface, the crests will lie at a different angle to the field line and this will cause field line bending. Therefore, this type of mode is highly localised in the vicinity of rational surfaces. Now a wave consisting of a single radially localised Fourier harmonic m has the same amplitude on both the inboard (good curvature) and the outboard (bad curvature) side[1]. In a tokamak, plasma shaping allows the good curvature to dominate and the wave is damped. One way to beat the stabilising effect of

[1]When a flux surface is radially perturbed, the curvature drift causes a vertical separation of opposite charges. A radial pressure gradient implies that there is a charge imbalance on the perturbed flux surface. The resulting electric field reinforces the perturbation on the outboard side and damps it on the inboard side.

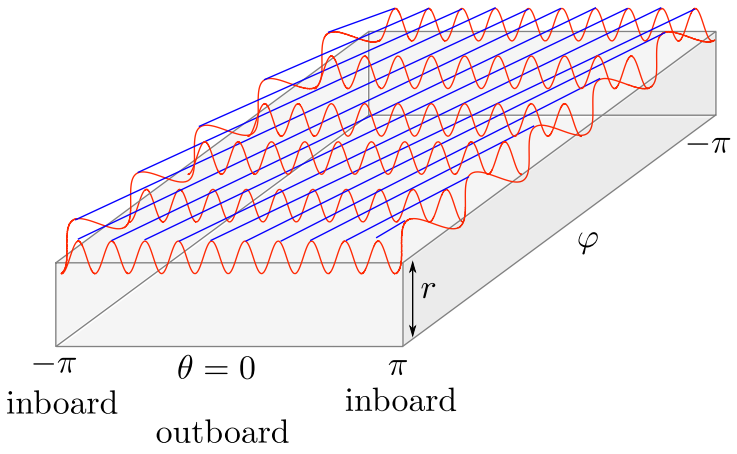

Figure 5.1: Flux surfaces in a torus (radius r, poloidal angle θ and toroidal angle φ) are cut and opened into a slab. An $m/n = 10/5$ mode is next introduced. Note the wave crests are parallel to the $q = 2$ field lines (in blue).

the average good curvature is to construct a mode that has a maximum amplitude in the bad curvature region. This can be achieved by fixing n and combining a number of poloidal Fourier modes[2] m, $m \pm 1$, $m \pm 2$ etc. This situation is illustrated by Fig. 5.2a. The waves are seen to constructively interfere on the outboard side (this is labelled by the 'ballooning angle' θ_0). Though clearly, in order to interfere with each other, the poloidal modes must extend radially to the adjacent rational surface. The result of this small but finite radial extent is that the field lines are actually bent a little, providing a stabilising influence.

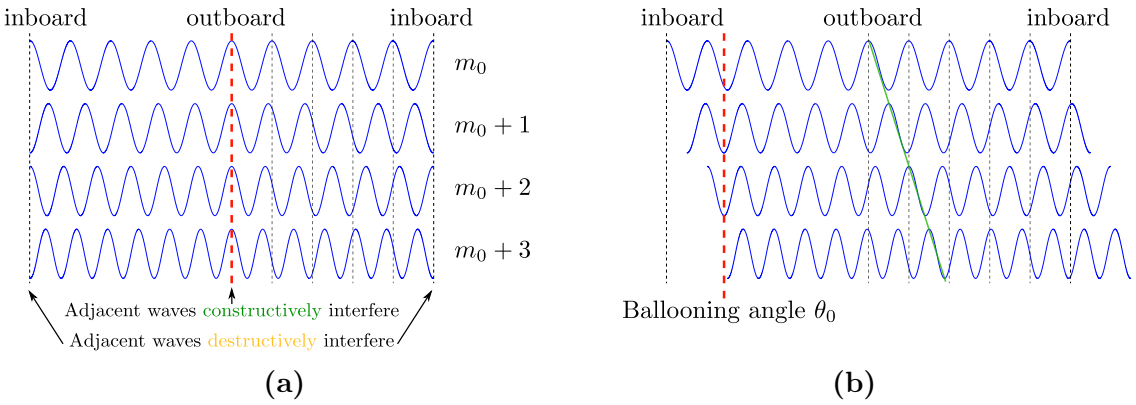

Figure 5.2: (a) shows different poloidal harmonics interfering to give a maximum/minimum amplitude on the outboard/inboard side. Here the ballooning angle $\theta_0 = 0$ (labelled by the red dashed-line). (b) illustrates how a sheared flow can introduce a phase shift (indicated in green), leading to a non-zero value of θ_0.

[2]Within linear theory, toroidal symmetry of the tokamak means we cannot couple different toroidal harmonics.

The effect of flows

We consider each flux surface as a rotating rigid body, free to move relative to others - this allows sheared flows. Shearless flows only affect the mode frequency - the growth rate, and thereby stability, remain unaffected. Initially, the waves constructively interfere on the outboard side (Fig. 5.2a); with time, as the flux surfaces move relative to each other, the poloidal angle where the modes interfere to give a maximum, rotates (Fig. 5.2b). Thus, θ_0 rotates poloidally from the outboard side to the inboard side, and back to the outboard side.

The role of magnetic shear

The formation of ballooning modes depends on the radial coupling of poloidal Fourier harmonics (Fig. 5.2). The separation of flux surfaces $\Delta = 1/nq'$ which determines the extent of the radial overlap, therefore the coupling, is controlled by the magnetic shear $\hat{s} \propto q'$. Evidently, in regimes with low $\hat{s}$, the radial coupling of poloidal modes is weak and the resulting modes are not well described by the ballooning formalism. The strength of this coupling has been shown to vary with the magnetic shear as $\exp(-1/|\hat{s}|)$ [200].

To summarise, in the absence of sheared flows, the growth rate will be given by the dominant mode's growth; the most violent modes typically balloon on the outboard side. With flow-shear, the poloidal angle where the ballooning mode peaks is expected to vary. The time-averaged growth rate of the ballooning mode will therefore involve an average over the mode's instantaneous growth at each poloidal location - making it more stable. Finally, note that while the electrostatic modes are also localised about rational surfaces, the physics is different. On irrational flux surfaces, the field lines can come arbitrarily close to one another, with an arbitrary phase on the perturbations. The fluctuations are thus more likely to cancel out and are unable to establish any coherent structure.

5.2 Ballooning theory: the mathematical framework

The ballooning formalism is an extremely useful tool to study high-n instabilities in axisymmetric toroidal systems such as tokamaks. This framework was first introduced to study MHD ballooning modes [172]. Broadly following the analyses in [71, 201], the subsequent sections introduce this formalism in detail.

5.2.1 The formalism

The potential perturbation $\tilde{\phi}$ in an axisymmetric torus can be described as

$$\tilde{\phi}(r,\theta,\varphi) = \phi(r,\theta)\mathrm{e}^{\mathrm{i}n\left[\varphi - \int^{\theta} q^* \mathrm{d}\theta\right]} \tag{5.1}$$

$$\approx \phi(r,\theta)\mathrm{e}^{-\mathrm{i}nq\theta}\mathrm{e}^{\mathrm{i}n\varphi} \,. \tag{5.2}$$

Here $q^* = rB_\varphi/RB_\theta$ is the local safety factor; the integral $\int^{\theta} q^* \mathrm{d}\theta$ describes the change in the toroidal coordinate as one traverses a poloidal angle θ whilst moving along a magnetic field line; and $q = (2\pi)^{-1}\oint q^* \mathrm{d}\theta$ is the poloidally-averaged safety factor. The above approximation is valid as long as the local q^* does not deviate much from the averaged q. The focus is on determining $\phi(r,\theta)\exp(\mathrm{i}nq\theta)$; the dependence on φ can be recovered by simply multiplying with $\exp(\mathrm{i}n\varphi)$. The problem with this form, however, is that it violates the poloidal periodicity constraint on $\tilde{\phi}$. To see this, note that the electrostatic potential must be periodic in θ, i.e.

$$\frac{\phi(r,\theta+2\pi)}{\phi(r,\theta)}\exp\left(\mathrm{i}2\pi nq\right) = 1 \,. \tag{5.3}$$

This is true if nq is an integer. The radial variation of q implies that away from rational surfaces, this periodicity constraint is violated.

One technique is to map a function $f(\theta)$ from the finite θ domain, periodic between $-\pi$ and π, to $\hat{f}(\eta)$ in the infinite 'ballooning domain' η. This is possible through the transform

$$f(\theta) = \sum_m \int_{-\infty}^{\infty} \hat{f}(\eta)\,\delta(\eta - 2\pi m - \theta)\,\mathrm{d}\eta \,, \tag{5.4}$$

where δ is the Dirac-delta function. For a given m, the integral picks out the function $\hat{f}(2\pi m + \theta)$. Convergence of the integral in eqn. 5.4 requires $\hat{f}(\eta) \to 0$ as $\eta \to \pm\infty$. For any suitably defined function, the summation then adds infinite copies of it, with each shifted by 2π. It is intuitive why this would lead to a periodic function. Next, making use of the identity

$$2\pi \sum_{k=-\infty}^{\infty} \delta\left(r - 2\pi k\right) = \sum_{m=-\infty}^{+\infty} \mathrm{e}^{\mathrm{i}mr} \tag{5.5}$$

(see Appendix B.2 for proof), eqn. 5.4 is straightforwardly written as

$$f(\theta) = (2\pi)^{-1}\sum_m \int_{-\infty}^{\infty} \hat{f}(\eta)\mathrm{e}^{\mathrm{i}m(\eta-\theta)}\,\mathrm{d}\eta \,. \tag{5.6}$$

Equation 5.6 is the standard ballooning transform. Then, the (periodic part of the)

electrostatic potential may be expressed according to eqn. 5.6 as:

$$\phi\,(r,\theta)\mathrm{e}^{-\mathrm{i}nq\theta} = \sum_m \mathrm{e}^{-\mathrm{i}m\theta} \int_{-\infty}^{\infty} \mathrm{e}^{\mathrm{i}m\eta}\ \hat{\phi}\,(r,\eta)\ \mathrm{d}\eta \tag{5.7}$$

$$= \sum_m \mathrm{e}^{-\mathrm{i}m\theta} u_m(r)\ . \tag{5.8}$$

The potential $\hat{\phi}(r,\eta)$, free from the periodicity constraint, is now amenable to the Wentzel-Kramers-Brillouin-Jeffreys (WKBJ) eikonal approach. Convergence of the integral 5.7 requires that $\hat{\phi} \to 0$ as $\eta \to \pm\infty$. Note, in neglecting profile variations (including in q) as a leading order assumption, $\Delta = (nq')^{-1} \to 0$ and the Fourier mode m is *identical* to $m \pm 1$. However, when we consider the full problem in the high-n limit, Δ is small and the adjacent Fourier modes are considered to differ by a slowly varying amplitude factor $A(x)$ and a constant phase difference θ_0 (as we shall see shortly, this phase difference is indeed the 'ballooning angle'). It is therefore appropriate to seek solutions of the form

$$u_m(x) = u_0\left(x - \frac{\delta m}{nq'}\right) A(x)\mathrm{e}^{\mathrm{i}m\theta_0}\ . \tag{5.9}$$

Here, the function $u_0(x)$ represents the radial variation of the reference mode $m_0 = nq_0$ and $x = r - r_0$ (r_0 is the rational surface where $q(r_0) = m_0/n$). The constant $\exp(-\mathrm{i}m_0\theta_0)$ is dropped for convenience. Writing $u_0(x)$ as a Fourier transform between the normalised radial coordinate $-nq'x$ and the field-aligned coordinate η (brought out by eqns. 5.7 and 5.8):

$$u_0(x) = \int_{-\infty}^{\infty} \mathrm{e}^{-\mathrm{i}nq'x\eta}\ \hat{u}(\eta)\ \mathrm{d}\eta\ ; \tag{5.10}$$

together with eqn. 5.9, gives

$$u_m(x) = A(x)\mathrm{e}^{\mathrm{i}m\theta_0} \int_{-\infty}^{\infty} \hat{u}(\eta)\,\mathrm{e}^{\mathrm{i}(\delta m - nq'x)\eta}\,\mathrm{d}\eta\ . \tag{5.11}$$

We may finally express the perturbed potential $\phi(x,\theta) = \sum_m u_m(x)\exp(-\mathrm{i}m\theta)$ as

$$\phi\,(x,\theta) = \sum_m \mathrm{e}^{-\mathrm{i}m(\theta-\theta_0)} \int_{-\infty}^{\infty} \mathrm{e}^{\mathrm{i}(\delta m - nq'x)\eta} A(x)\hat{u}(\eta)\ \mathrm{d}\eta\ . \tag{5.12}$$

5.2.2 The ballooning angle θ_0

The role of θ_0 is revealed by eqn. 5.12: Fourier harmonics constructively interfere at $\theta = \theta_0$, and the global mode has a maximum, i.e. 'balloons' at θ_0. Reverting our

attention back to eqn. 5.7, $\hat{\phi}$ can be written as (cf. eqn. 5.2)

$$\hat{\phi}(r,\eta) = \hat{A}(x,\eta)\,\mathrm{e}^{-\mathrm{i}nq\eta} \tag{5.13}$$

$$= A(x,\eta)\mathrm{e}^{\mathrm{i}nq'S(x)}\mathrm{e}^{-\mathrm{i}nq\eta}\,. \tag{5.14}$$

Here $A(x,\eta)$ is the slowly varying amplitude envelope in x, the function $S(x)$ varies slowly with x, but the phase $\exp[\mathrm{i}S(x)/\Delta]$ varies rapidly between rational flux surfaces. Taking the leading-order radial derivative of eqn. 5.14, i.e. ignoring the radial variation of $A(x,\eta)$:

$$\frac{\partial}{\partial x} \to \mathrm{i}nq'\left(\frac{\mathrm{d}S(x)}{\mathrm{d}x} - \eta\right) \quad . \tag{5.15}$$

Comparing with the Fourier derivative representation, $\mathrm{d}/\mathrm{d}x \to \mathrm{i}k_x$, we can see that $nq'\,\mathrm{d}S/\mathrm{d}x = k_x$ (evaluated at $\eta = 0$). Next, compare eqns. 5.12 and 5.7 with the help of 5.14; we observe

$$A(x)\,\hat{u}(\eta)\,\mathrm{e}^{\mathrm{i}m\theta_0} = A(x,\eta)\,\mathrm{e}^{\mathrm{i}nq'S(x)}\,. \tag{5.16}$$

Assuming $A(x,\eta) \approx A(x)\,\hat{u}(\eta)$, it is apparent

$$m\theta_0 = nq'S(x)\,. \tag{5.17}$$

Noting $\delta x = \delta m\Delta$, i.e. $nq' = \delta m/\delta x \approx \mathrm{d}m/\mathrm{d}x$, we find

$$\frac{\mathrm{d}S(x)}{\mathrm{d}x} = \theta_0\,, \tag{5.18}$$

which from the earlier relation $nq'(\mathrm{d}S(x)/\mathrm{d}x) = k_x$, relates the ballooning angle to the radial wavenumber:

$$k_x = nq'\theta_0\,. \tag{5.19}$$

5.2.3 Fourier-ballooning representation

Substituting $m\theta_0 = nq'S(x)$ into eqn. 5.12, and upon some rearrangement

$$\phi(x,\theta) = \mathrm{e}^{\mathrm{i}nq'S(x)}A(x)\sum_m \int_{-\infty}^{\infty} \mathrm{e}^{\mathrm{i}m(\eta-\theta)}\,\mathrm{e}^{-\mathrm{i}nq\eta}\,\hat{u}(\eta)\,\mathrm{d}\eta \quad . \tag{5.20}$$

We first express the radial variation to the potential as a Fourier transform:

$$\mathrm{e}^{\mathrm{i}nq'S(x)}A(x) = \int_{-\infty}^{\infty} \chi(p)\,A(p)\,\mathrm{e}^{\mathrm{i}nq'xp}\,\mathrm{d}p\,. \tag{5.21}$$

Here p is the conjugate Fourier variable to $nq'x$, $\chi(p)$ and $A(p)$ label the slow and fast variations in p. Next, with the help of eqn. 5.6, we express the integral-sum in

eqn. 5.20 as

$$\sum_m \int_{-\infty}^{\infty} \mathrm{e}^{\mathrm{i}m(\eta-\theta)} \hat{u}(\eta)\, \mathrm{e}^{-\mathrm{i}nq\eta}\, \mathrm{d}\eta = \hat{\xi}(\theta) \mathrm{e}^{-\mathrm{i}nq\theta} \quad . \tag{5.22}$$

The potential $\phi(x,\theta)$ is now written using eqns. 5.21 and 5.22 as

$$\phi(x,\theta) = \int_{-\infty}^{\infty} \hat{\xi}(\theta)\chi(p)A(p)\, \mathrm{e}^{\mathrm{i}nq'x(p-\theta)} \mathrm{e}^{-\mathrm{i}nq_0\theta}\, \mathrm{d}p \tag{5.23}$$

$$= \int_{-\infty}^{\infty} \xi(p,\theta)A(p)\, \mathrm{e}^{\mathrm{i}nq'x(p-\theta)} \mathrm{e}^{-\mathrm{i}nq_0\theta}\, \mathrm{d}p \quad , \tag{5.24}$$

where the term $\xi(p,\theta)$ varies slowly in p in relation to $A(p)$ and $q = q_0 + q'x$. The above equation is referred to as the Fourier-Ballooning representation and was first introduced in [202].

5.2.4 Leading-order theory

To put in use the formalism developed so far, we study a simple fluid-ITG system described by eqn. 4.1. Decomposing the potential into poloidal harmonics

$$\phi(x,\theta) = \sum_m u_m(x) \mathrm{e}^{-\mathrm{i}m\theta} \quad , \tag{5.25}$$

and noting that

$$\int_{-\pi}^{\pi} \left(\sum_m u_m(x) \mathrm{e}^{-\mathrm{i}m\theta} \right) \mathrm{e}^{\mathrm{i}k\theta} \mathrm{d}\theta = 2\pi u_m(x) \ , \tag{5.26}$$

we straightforwardly project out the Fourier harmonics to write:

$$\begin{aligned} \left[\rho_s^2 \frac{\mathrm{d}^2}{\mathrm{d}x^2} + \frac{\sigma^2}{\Omega^2} \left(\delta m - nq'x\right)^2 - \left(\frac{\Omega - 1}{\Omega + \eta_s} + k_\theta^2 \rho_s^2 \right) \right] u_m \\ - \frac{\epsilon_n}{\Omega} \left[\left(1 + \frac{1}{k_\theta} \frac{\mathrm{d}}{\mathrm{d}x} \right) u_{m+1} + \left(1 - \frac{1}{k_\theta} \frac{\mathrm{d}}{\mathrm{d}x} \right) u_{m-1} \right] = 0 \ . \end{aligned} \tag{5.27}$$

Equation 5.27 is effectively 2D, since it needs to be solved for a finite set of poloidal mode numbers $\{u_m(x)\}$, such that the behaviour of the global mode is properly captured. Using eqn. 5.11 however, it may be reduced to a 1D ordinary differential equation (ODE) along the field line coordinate η. For this, we must make the *leading-order* assumption of neglecting the effect of equilibrium scale variations, captured by the term $A(x)$. Then we may write

$$\frac{\mathrm{d}u_m}{\mathrm{d}x} = A(x) \mathrm{e}^{\mathrm{i}m\theta_0} \int_{-\infty}^{\infty} \left(-\mathrm{i}nq'\eta\right) \hat{u}(\eta) \mathrm{e}^{\mathrm{i}(\delta m - nq'x)\eta}\, \mathrm{d}\eta \quad . \tag{5.28}$$

Next multiplying u_m by $\mathrm{i}(\delta m - nq'x)$ and integrating by parts (noting $\hat{u}(\eta) \to 0$ as $\eta \to \pm\infty$)

$$\mathrm{i}(\delta m - nq'x)u_m = A(x)\mathrm{e}^{\mathrm{i}m\theta_0} \int_{-\infty}^{\infty} -\frac{\mathrm{d}\hat{u}(\eta)}{\mathrm{d}\eta}\mathrm{e}^{\mathrm{i}(\delta m - nq'x)\eta}\,\mathrm{d}\eta \quad . \tag{5.29}$$

Finally, using eqns. 5.11, 5.28 and 5.29 with eqn. 5.27, we arrive at the *local/leading-order* ballooning equation for the structure of the perturbation along the magnetic field-line:

$$\left[\frac{\sigma^2}{\Omega^2}\frac{\mathrm{d}^2}{\mathrm{d}\eta^2} + (\rho_s nq'\eta)^2 + \frac{2\epsilon_n}{\Omega}\left(\cos(\eta+\theta_0) + \hat{s}\eta\sin(\eta+\theta_0)\right) + \left(\frac{\Omega-1}{\Omega+\eta_s} + k_\theta^2\rho_s^2\right)\right]\hat{u}(\eta) = 0 \quad . \tag{5.30}$$

This is a one-dimensional ODE which can be solved for the eigenfunction $\hat{u}(\eta)$ given x and θ_0 - free parameters at this order. Here we stress upon the important distinction between the *local* eigenvalue of eqn. 5.30, henceforth referred to as $\Omega_0(x,\theta_0)$, and the *global* (true) eigenvalue of eqn. 4.1, Ω, which is independent of x and θ_0. The two eigenvalues are in fact related; this relation is brought out by the plasma profiles - an effect neglected in the leading order treatment, but captured by the higher-order theory discussed next. The ballooning angle θ_0 is also *predicted* at this higher-order.

5.2.5 Higher-order theory

The relation between the local and global eigenvalues is more readily brought out by employing the Fourier-ballooning transform (eqn. 5.24). Taking the differentials of this equation leads to:

$$\frac{\partial\phi}{\partial x} = \int_{-\infty}^{\infty} \mathrm{i}nq'(p-\theta)\,\xi(p,\theta)A(p)\mathrm{e}^{\mathrm{i}nq'x(p-\theta)}\mathrm{e}^{-\mathrm{i}nq_0\theta}\,\mathrm{d}p \quad , \tag{5.31}$$

$$\frac{\partial\phi}{\partial\theta} + \mathrm{i}nq\phi = \int_{-\infty}^{\infty} \frac{\partial\xi(p,\theta)}{\partial\theta}A(p)\mathrm{e}^{\mathrm{i}nq'x(p-\theta)}\mathrm{e}^{-\mathrm{i}nq_0\theta}\,\mathrm{d}p \quad . \tag{5.32}$$

Substituting the above equation set into eqn. 4.1 yields eqn. 5.30 with the following transformations:

$$\eta \to \theta - p \qquad \hat{u}(\eta) \to \xi(p,\theta) \qquad \theta_0 \to p\,. \tag{5.33}$$

We note a final transformation by multiplying eqn. 5.24 with x:

$$x\phi = \int_{-\infty}^{\infty} xA\,\xi\, \mathrm{e}^{\mathrm{i}nq'x(p-\theta)}\mathrm{e}^{-\mathrm{i}nq_0\theta}\,\mathrm{d}p \tag{5.34}$$

$$= \frac{1}{\mathrm{i}nq'}\int_{-\infty}^{\infty} A\,\xi\,\frac{\partial}{\partial p}\mathrm{e}^{\mathrm{i}nq'x(p-\theta)}\mathrm{e}^{-\mathrm{i}nq_0\theta}\,\mathrm{d}p \tag{5.35}$$

$$= -\frac{1}{\mathrm{i}nq'}\int_{-\infty}^{\infty} \frac{\mathrm{d}A}{\mathrm{d}p}\,\xi\mathrm{e}^{\mathrm{i}nq'x(p-\theta)}\mathrm{e}^{-\mathrm{i}nq_0\theta}\,\mathrm{d}p \quad , \tag{5.36}$$

where the last step is obtained by integration by parts, with $|\partial\xi/\partial p| \ll |\mathrm{d}A/\mathrm{d}p|$ and vanishing boundary conditions on $\xi(p,\theta)$. We accordingly define the transformations:

$$xA \to -\frac{1}{\mathrm{i}nq'}\frac{\mathrm{d}A}{\mathrm{d}p} \qquad\qquad x^2A \to -\frac{1}{(nq')^2}\frac{\mathrm{d}^2A}{\mathrm{d}p^2}\,. \tag{5.37}$$

5.2.5.1 Relating the local and global eigenvalues

To summarise the results obtained so far, the global time-dependent problem

$$\mathcal{L}\left[\frac{\mathrm{i}}{nq'}\frac{\partial}{\partial x}, \frac{\partial}{\partial\theta} + \mathrm{i}nq(x), x, \theta, \frac{\partial}{\partial t}\right]\phi(x,\theta,t) = 0 \tag{5.38}$$

is reduced to

$$\mathcal{L}\left[(\theta - p), \frac{\partial}{\partial\theta}, x, \theta, \frac{\partial}{\partial t}\right]\xi(p,\theta,x,t) = 0 \tag{5.39}$$

by the Fourier-ballooning transformation of 5.24. Note that the time dependence is implicit to both equations. Local flux-tube codes such as GS2 solve $\xi(p,\theta,x,t)$ for the free parameters x and p, such that the instability growth rate is maximised. Now the global (Ω) and local eigenmodes (Ω_0) of the above equations are seen to be related by

$$\frac{\partial\phi}{\partial t} = -\mathrm{i}\Omega\phi = -\mathrm{i}\int_{-\infty}^{\infty}\Omega_0(x,p)\hat{\xi}(x,p)\mathrm{e}^{\mathrm{i}nq'x(p-\theta)}\mathrm{e}^{-\mathrm{i}nq_0\theta}A(p)\mathrm{d}p\,, \tag{5.40}$$

where we have assumed $\xi = \hat{\xi}\exp(-\mathrm{i}\Omega_0 t)$ and $\phi = \hat{\phi}\exp(-\mathrm{i}\Omega t)$. Next, Taylor-expanding Ω_0 in x:

$$\int_{-\infty}^{\infty}\left[\Omega_0(p) + \Omega_x x + \frac{\Omega_{xx}}{2}x^2 - \Omega\right]A(p)\hat{\xi}(x,p)\mathrm{e}^{\mathrm{i}nq'x(p-\theta)}\mathrm{e}^{-\mathrm{i}nq_0\theta}\mathrm{d}p = 0\,, \tag{5.41}$$

(Ω_x and Ω_{xx} denote the first and second order partial derivatives in x) and making use of the transforms 5.37, we derive

$$\frac{\Omega_{xx}}{2(nq')^2}\frac{\mathrm{d}^2A}{\mathrm{d}p^2} + \frac{\Omega_x}{\mathrm{i}nq'}\frac{\mathrm{d}A}{\mathrm{d}p} - [\Omega_0(p) - \Omega]\,A = 0\,. \tag{5.42}$$

Equation 5.42 must be solved subject to the periodicity constraint $A(p) = A(p+2\pi)$ to ensure that the electrostatic potential is periodic in θ; note also $\Omega_0(p)$ is periodic in p. Finally, depending on the radial variation in Ω_0, as determined by the plasma profiles, we find two distinct classes of microinstabilities in a toroidal plasma.

5.2.5.2 Isolated Mode: quadratic radial variation

In the special situation when Ω_0 is stationary in the $x-p$ plane, i.e. $\Omega_x = 0$ (both real and imaginary parts must be stationary at the same radial location) *and* $\Omega_p = 0$ (typically at the outboard midplane, i.e. $p = 0$), eqn. 5.42 reduces to

$$\frac{\Omega_{xx}}{2(nq')^2}\frac{\mathrm{d}^2A}{\mathrm{d}p^2} - \left[\Omega_{00} + \frac{\Omega_{pp}}{2}p^2 - \Omega\right]A = 0 \tag{5.43}$$

(here we have Taylor-expanded $\Omega_0(p) = \Omega_{00}+\Omega_p p+\Omega_{pp}p^2/2+\dots$). Due to the stringent requirement on its existence, this class of toroidal drift instabilities, following [176, 192], were referred to as *Isolated Modes (IMs)*. Equation 5.43 is easily rewritten as

$$\frac{\mathrm{d}^2A}{\mathrm{d}p^2} + (\lambda - \mu p^2)A = 0\,, \tag{5.44}$$

where $\lambda = 2(nq')^2(\Omega-\Omega_{00})/\Omega_{xx}$ and $\mu = (nq')^2(\Omega_{pp}/\Omega_{xx})$. Equations of the form 5.44 are solved according to Appendix B.1 by

$$A(p) \propto H_l(p)\exp(-\sigma p^2)\,. \tag{5.45}$$

Here l is the order of the Hermite polynomial and σ is to be determined. For simplicity, we restrict ourselves to the fundamental $l = 0$ mode in this analysis. Substituting $A \propto \exp(-\sigma p^2)$ into eqn. 5.44, we find the structure of the perturbation:

$$A \propto \exp\left[-\frac{nq'}{2}\sqrt{\frac{\Omega_{pp}}{\Omega_{xx}}}\,p^2\right], \tag{5.46}$$

and an expression relating the global and local eigenvalues:

$$\Omega = \Omega_{00} + \frac{1}{2nq'}\sqrt{\Omega_{xx}\Omega_{pp}}\,. \tag{5.47}$$

Equation 5.46 implies that $A(p)$ is a Gaussian localised near $p = 0$, and scales in width as $\Delta p \sim (\Omega_{xx}/\Omega_{pp})^{1/4}/\sqrt{nq'}$. Since $A(p)$ is directly related to $\phi(x,\theta)$ through the Fourier-ballooning integral, we expect ϕ to have a similar Gaussian radial envelope which scales with the toroidal mode number as $1/\sqrt{n}$. Equation 5.47 tells us that, for the Isolated Mode, the global eigenvalue is equal to the local eigenvalue at the latter's stationary point, with a $1/n$ correction introduced as a result of profile effects.

5.2.5.3 General Mode: linear radial variation

But there exists a more general class, which does not have any constraint on its existence. This class is referred to as the *General Mode (GM)*. To study its properties, we consider only the first-order radial variation to eqn. 5.42:

$$\frac{\Omega_x}{\mathrm{i}nq'}\frac{\mathrm{d}A}{\mathrm{d}p} = [\Omega_0(p) - \Omega]\, A\,. \tag{5.48}$$

Upon integrating in p over the 2π periodic domain we find

$$\ln A(p+2\pi) - \ln A(p) = \mathrm{i}nq' \oint \frac{\Omega_0(p) - \Omega}{\Omega_x}\,\mathrm{d}p\,. \tag{5.49}$$

Noting that $A(p)$ must be periodic, we are left with

$$1 = \exp\left(\mathrm{i}nq' \oint \frac{\Omega_0(p) - \Omega}{\Omega_x}\mathrm{d}p\right) = \exp(2\pi \mathrm{i}w) \tag{5.50}$$

(here w is an integer). With the poloidal average defined as $\langle \dots \rangle = (2\pi)^{-1} \oint \dots \mathrm{d}p$, eqn. 5.50 simplifies to

$$\Omega = \frac{1}{\langle \Omega_x^{-1} \rangle}\left\langle \frac{\Omega_0(p)}{\Omega_x} \right\rangle - \frac{w}{nq'\langle \Omega_x^{-1} \rangle}\,. \tag{5.51}$$

For a circular cross-section plasma, the simplest p variation that satisfies the periodicity constraint on the local frequency is $\Omega_0(p) = \overline{\Omega} + \epsilon \cos p$, where $\overline{\Omega} = (2\pi)^{-1} \oint \Omega_0(p)\,\mathrm{d}p$ is defined to be the averaged local frequency. Further assuming that Ω_x has no p dependence, we find

$$\Omega \approx \overline{\Omega}\,. \tag{5.52}$$

That is, the global complex frequency is just an average of the local complex frequency over p at the chosen radial location (plus an $1/nq'$ correction). The GM is therefore more stable than the IM (the latter effectively picks out the most unstable local eigenvalue). To determine the mode structure in our simplified model, we use $\Omega = \overline{\Omega}$ together with eqn. 5.48 to arrive at

$$A(p) \propto \exp\left(\mathrm{i}nq' \frac{\epsilon}{\Omega_x} \sin p\right)\,. \tag{5.53}$$

From the method of stationary phase, for high n, the integral 5.24 will be strongly localised around the turning point of $\sin p$, i.e. when $p = \pm\pi/2$. The correct sign is determined in conjunction with the sign of ϵ/Ω_x, such that the integral is well behaved.

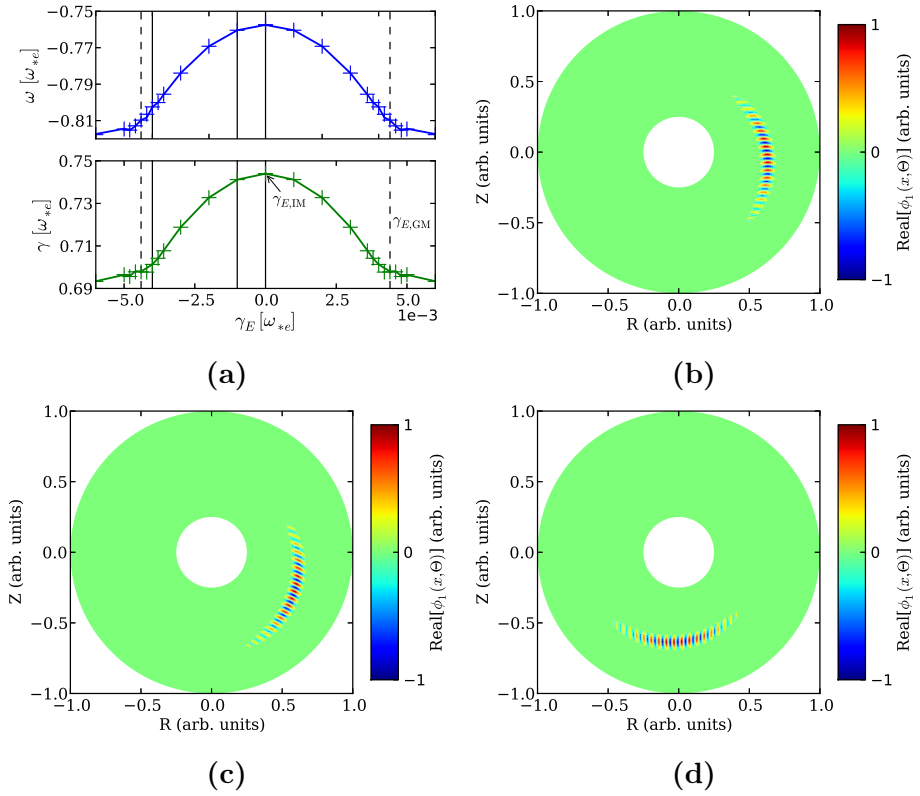

Figure 5.3: In (a), the solid curves show the *converged* eigenvalues from the initial-value code, whereas the crosses are solutions to the eigenmode eqn. 4.1 using the code from ref. [178]. The subsequent frames show how the IM (b) smoothly evolves (c) into the GM (d), as the flow-shear increases from $\gamma_E = 0$, through $\gamma_E = -0.001$ and finally to $\gamma_E = -0.004$, as indicated by the vertical lines in (a). The instability is a fully developed GM for $|\gamma_E| \geq \gamma_{E,\mathrm{GM}}$ (dashed lines in (a)).

5.3 Global mode behaviour: stationary profiles

Having established the theory of drift-ballooning modes, we now proceed to study their dynamics using the new global initial-value fluid-ITG code. For the results discussed in this section, all simulations were performed with plasma *profiles held fixed in time*. The simulations were initialised with noise, and after sufficient time, the initial-value code is seen to converge to an eigenmode solution (Fig. 4.2). Note how all the individual $\Omega_m(t)$ converge to a single global complex mode frequency Ω as the eigenmode establishes.

5.3.1 Obtaining the global eigenmodes: the IM and GM

We first set the flow-shearing rate $\gamma_E = 0$, and neglect all profile variations except for a quadratic η_s profile. As described in [178, 181], we then expect the IM which should balloon at the outboard-midplane (see Fig. 5.3b). The incorporation of flow-shear Doppler shifts the real part of the complex mode frequency, removing the stationary point from the complex $\Omega_0(x)$. The IM is therefore no longer possible and the global eigenmode moves to peak away from the outboard midplane. Referring to Fig. 5.3a,

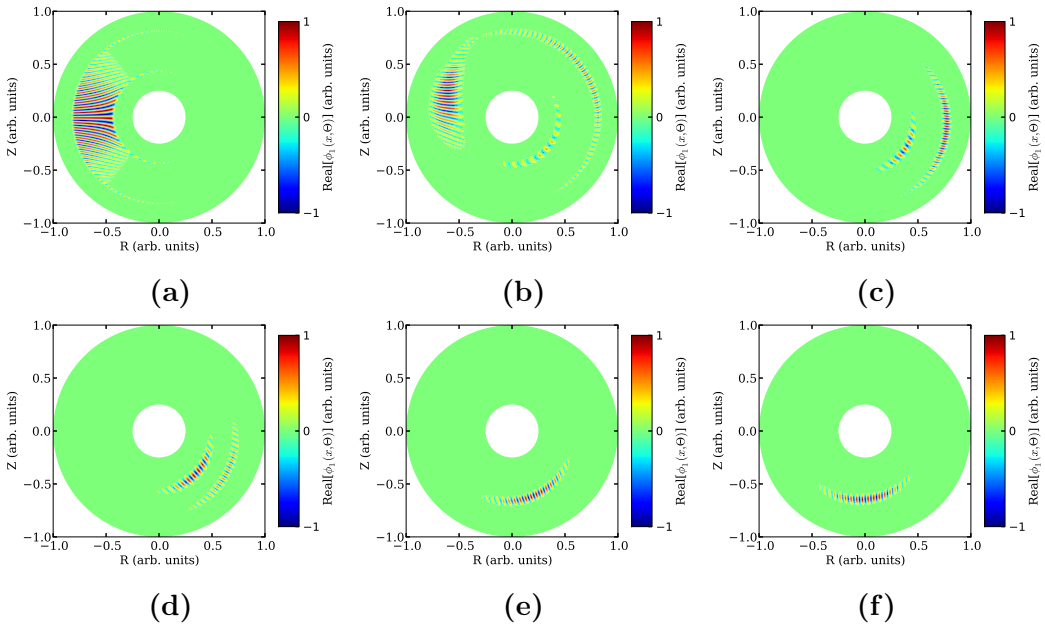

Figure 5.4: The plots show the poloidal mode-structure of the instability as it evolves towards a GM, after initiating the perturbation on the inboard side (to the left of each figure) with $\gamma_E = -0.95\gamma_{E,\mathrm{GM}}$. (a) shows the initial perturbation; (b)-(c) show the rapid formation of the outboard structure (only for $\gamma_E = \gamma_{E,\mathrm{IM}}$ does the final eigenmode establish here), accompanied by a decay of the initial inboard perturbation; and (d)-(f) show the subsequent evolution towards the GM. The frames correspond to the times 0T, 0.017T, 0.071T, 0.125T, 0.5T and 1.0T, where T is the eigenmode formation time.

the IM is seen to have the strongest growth. As the flow-shear magnitude is steadily increased towards $|\gamma_E| = \gamma_{E,\mathrm{GM}}$, the ITG growth rate γ is reduced, and the IM is seen to smoothly evolve into the GM (Figs. 5.3b-5.3d), rotating from the outboard midplane at $\theta = 0$ for $\gamma_E = 0$ to the top/bottom at $\theta = \pm\pi/2$ for $|\gamma_E| > \gamma_{E,\mathrm{GM}}$. For our parameters (refer to Table 4.3), $|\gamma_{E,\mathrm{GM}}| = 0.004$. The GM complex growth rate is only weakly dependent on γ_E, and the transition to this asymptotic regime is labelled by $\gamma_{E,\mathrm{GM}}$ in Fig. 5.3a. The IM therefore exists within a narrow window in γ_E, which, in our model, is in the vicinity of $\gamma_E = 0$. In general, as we introduce plasma profiles (i.e. an x-dependence of q, ϵ_n etc.), the IM is accessed for a non-zero value of $\gamma_E = \gamma_{E,\mathrm{IM}}$ [181, 203]. Also note the small difference between γ_{GM} and γ_{IM}. This is likely a result of the large aspect-ratio assumption ($\epsilon_n \ll 1$) and high magnetic shear, which favour the slab-like modes. For realistic geometries, we expect the Fourier modes to be more strongly coupled, leading to more highly unstable IMs compared to GM. But qualitatively, the results would be similar to those presented here.

5.3.2 Dynamics of eigenmode formation

The previous section was only concerned with the final states of the time-evolving perturbations; this section discusses their evolution. Depending on how the perturbation is initialised, we observe three distinct scenarios for the formation of the eigen-

mode. Firstly, as illustrated in Fig. 5.4, if the initial perturbation peaks around the inboard-midplane, then independent of γ_E, the initial structure decays rapidly, and almost *simultaneously*, a transient double-structure is established near the outboard-midplane - this is not yet an eigenmode. Now if $|\gamma_E| < \gamma_{E,\mathrm{GM}}$, this double-structure combines into a single *coherent* eigenmode structure localised on the outboard side (at the midplane if $\gamma_E = \gamma_{E,\mathrm{IM}} = 0$). This is the situation shown in Fig. 5.4, where $\gamma_E = -0.0038 = -0.95\gamma_{E,\mathrm{GM}}$. Figures 5.3b and 5.3c give two further examples of the converged eigenmode structure for smaller values of $|\gamma_E| < \gamma_{E,\mathrm{GM}}$ ($\gamma_E = 0$ and -0.001). If however $|\gamma_E| \geq \gamma_{E,\mathrm{GM}}$, the coherent mode is convected poloidally and performs many poloidal rotations, before finally settling down to the eigenmode. This *Floquet* behaviour is distinguished by its periodic variation in $\gamma(t)$ (Fig. 5.5a), and will be described in more detail in Section 5.3.3. Secondly, if the perturbation is initialised anywhere on the outboard side, independent of γ_E, a strong single coherent structure first forms *at* the position of the initial perturbation, before being convected to its final eigenmode position. Figure 5.5b shows the evolution of the global growth rate when the initial perturbation amplitude is maximum at the outboard-midplane. Finally, when initialised with random noise distributed uniformly in the poloidal angle, a coherent structure first forms at the outboard-midplane *independent* of the size of γ_E. Next, and as with both previous scenarios, if $|\gamma_E| < \gamma_{E,\mathrm{GM}}$, the structure rotates to the poloidal position associated with its eigenmode and stays there, whereas if $|\gamma_E| \geq \gamma_{E,\mathrm{GM}}$, the coherent structure rotates continually to establish the Floquet Mode (Fig. 5.5c).

5.3.3 Floquet Modes

With the inclusion of sheared plasma rotation, the standard ballooning representation no longer captures the eigenfunction efficiently, as the sheared rotation destroys the underlying equivalence of adjacent rational flux surfaces. Cooper [204] addressed this by employing a time-dependent eikonal, which then leads to Floquet Modes. In ref. [205], Taylor and Wilson use an alternative eigenmode representation and conclude that, when higher-order $(1/n)$ effects are considered (as captured directly by these global simulations), a perturbation adopts a time-dependent Floquet form which evolves towards the eigenmode over $\sim n$ Floquet periods. Our simulations shed more light on this mechanism and we quantify this for specific cases. We first establish the most unstable eigenmode for the parameters $\epsilon_n = 0.04$ and $\gamma_E = -0.003$, which is located near the bottom of the poloidal cross-section, as shown in Fig. 5.6b. We then re-start the simulation, and at $t = 200$, switch the flow-shear to $\gamma_E = 0.006$ instantly, and hold it fixed in time for the remainder of the simulation. Figure 5.6a shows how the global instantaneous Floquet Mode growth rate, $\gamma_{\mathrm{FM}}(t)$, evolves in time in response to this change in γ_E. The eigenmode for this new shearing rate

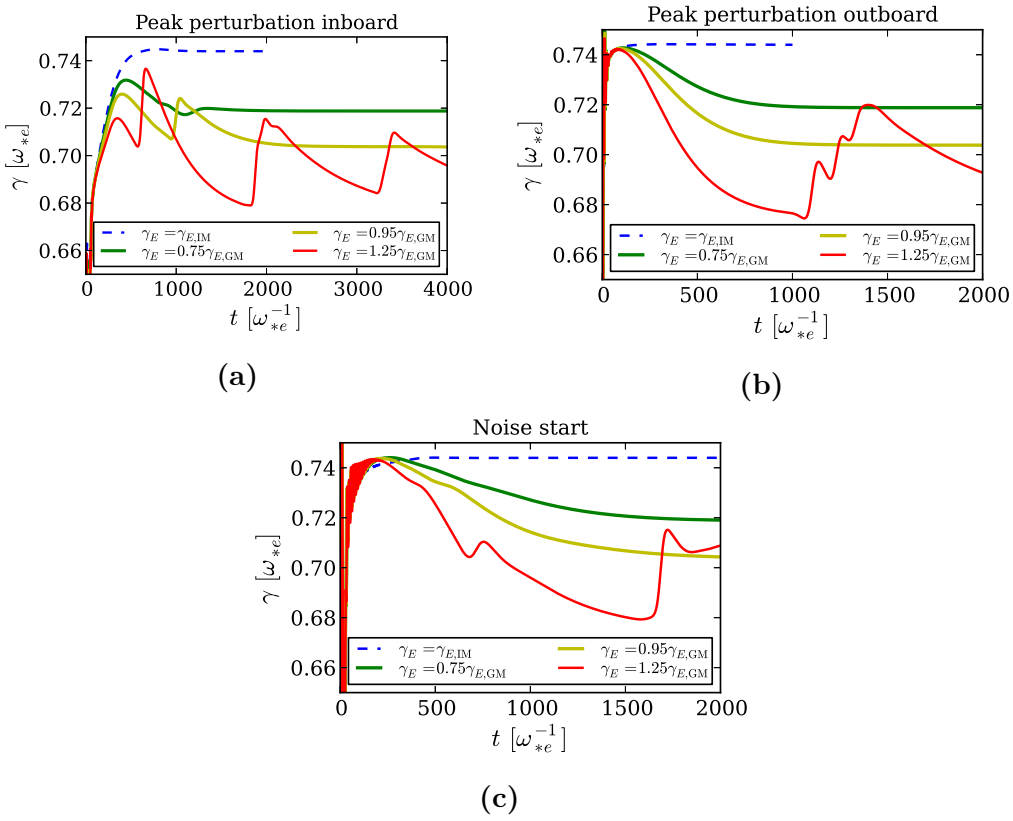

Figure 5.5: Evolution of the global growth rates in time, as a function of the flow-shearing rate for different initial perturbations: (a) maximum amplitude on the inboard side; (b) maximum amplitude on the outboard side; and (c) poloidally uniform noise. For the case $\gamma_E = 1.25\gamma_{E,\mathrm{GM}}$, we just show the first few Floquet periods.

would be localised at the top of the plasma. However, instead of rotating poloidally to the top and staying there (Fig. 5.6c), the mode overshoots to the inboard side (Fig. 5.6d), then makes a *rapid* transition (Fig. 5.6e) to the outboard side (Fig. 5.6f), before again slowly tracking across the top; this rotation in the poloidal angle continues for many periods. The final three plots (Figs. 5.6g, 5.6h, 5.6i) show a similar behaviour for the next Floquet period, except now the onset of the rapid outboard transition occurs closer to the top, and the mode whips even faster around the bottom. Further into the simulation, the evolving Floquet Mode gradually spends less time at the bottom and more time at the top with each cycle, before eventually settling down as a GM, with $\gamma_{\mathrm{FM}}(t) \to \gamma_{\mathrm{GM}}$ as predicted in ref. [205]. Our simulations suggest that the onset of this Floquet-like poloidal precession occurs when the flow-shear exceeds the threshold value, indicated by $\gamma_{E,\mathrm{GM}}$ in Fig. 5.3. For $|\gamma_E| \sim \gamma_{E,\mathrm{GM}}$, the instability goes to the top/bottom of the poloidal cross-section and stays there, but exceeding this value tips the mode into a Floquet oscillation.

Taylor and Wilson [205] further conclude that Floquet solutions evolve to the eigenmode over a time of order $n\kappa/\kappa_1$ Floquet periods, where the radial flow profile is given by $f = \kappa y + \kappa_1 y^2/n$ (cf. Table 4.2). Note that in a higher-order treatment, even with $\kappa_1 = 0$, the radial variation in other equilibrium quantities typically contribute

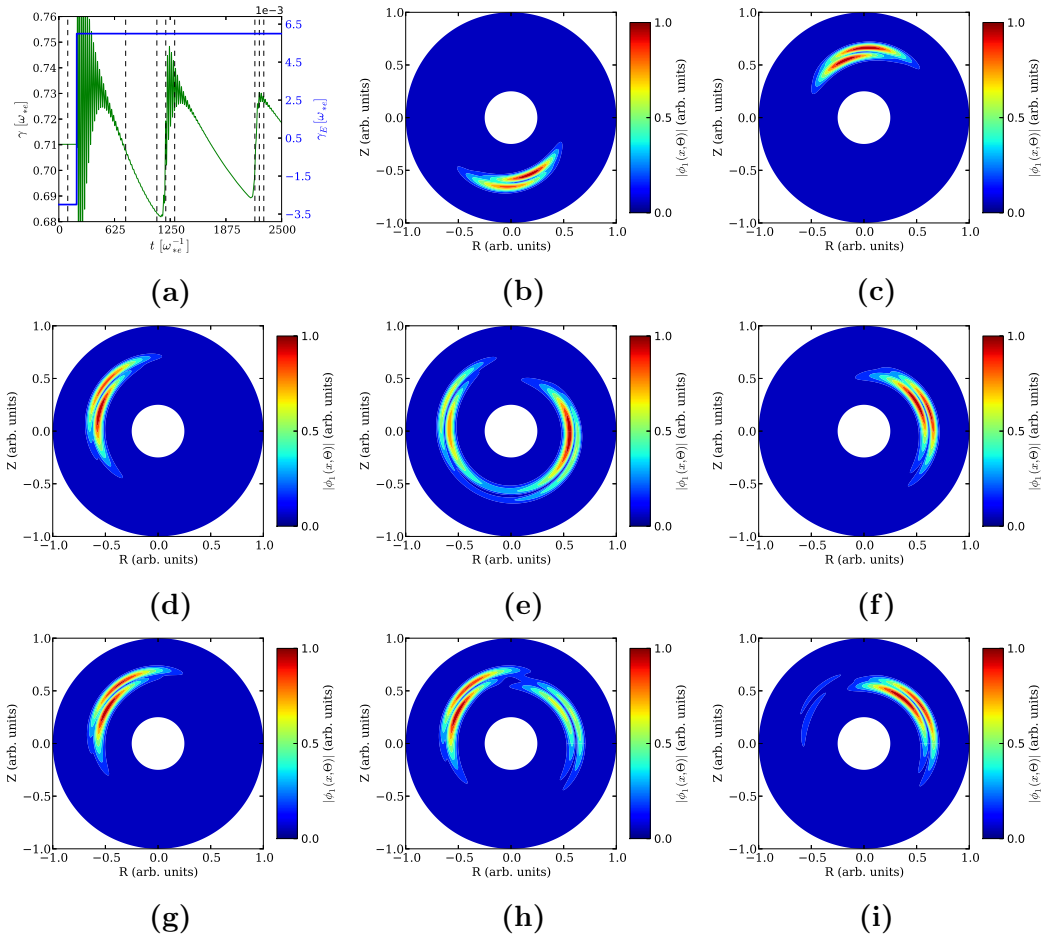

Figure 5.6: (a) shows the global growth rate γ (green) and flow-shear γ_E (blue) as a function of the normalised time. The dashed vertical lines indicate time-slices that correspond to the potential plots presented in frames (b)-(i) in chronological order. The potential plots are non-uniformly spaced in time.

an $\mathcal{O}(n^{-2})$ piece to the quadratic term (such as $\eta_s(x)$), implying then that the Floquet Mode settles down to the eigenmode after $\mathcal{O}(n^2)$ periods of rotation, as is the case in Fig. 5.6. Note also that ref. [205] analyses the electron-drift branch of eqn. 4.1. Nonetheless, we expect their conclusions will hold for all toroidal drift modes, in particular the ITG mode considered here; this is confirmed in Fig. 5.7. Each run is initialised with a perturbation on the outboard side, then performing scans in κ_1 at fixed κ and n, we find that the number of Floquet periods (approximated by the decaying amplitude envelope in Fig. 5.7a falling below a threshold) to converge to the eigenmode, is well described by the analytic linear scaling $n\kappa/\kappa_1$ of [205] (with the coefficient of determination R^2 = 0.97). Note that for $n\kappa/\kappa_1$ = −40 and −100, Fig. 5.7a shows the classic Floquet behaviour. For $n\kappa/\kappa_1$ = −30 however, there is no Floquet behaviour, as the expected γ_E would have dropped below the $\gamma_{E,\mathrm{GM}}$ for these parameters.

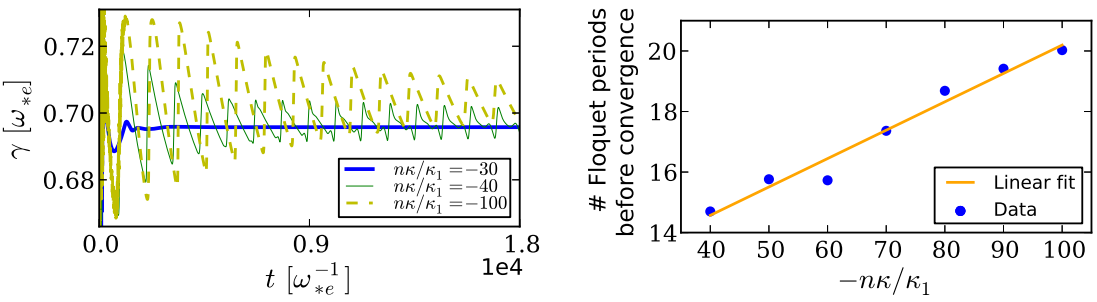

(a) **(b)**

Figure 5.7: (a) shows the evolution of the growth rate in time for three different values of $n\kappa/\kappa_1$. Scans have been performed with fixed $\kappa = -0.005$, $n = 50$ and $\epsilon_n = 0.04$, while κ_1 was varied. (b) shows the number of Floquet periods required for the decaying global growth rate envelope in (a) to converge to within 0.1% of the eigenmode growth rate.

5.4 Global mode behaviour: dynamic profiles

The trigger for Type-I ELMs is well described by the ideal-MHD peeling-ballooning model [132, 173], and some other ELM types are qualitatively consistent with MHD triggers (section 3.3.2.2). But, are all ELMs necessarily MHD events? Or can the linear properties of toroidal drift modes provide an alternative model for some small-ELM types? In exploring whether such a model could explain small-ELMs, we are interested in how these modes would respond to evolving plasma profiles, particularly, as the flow-shear passes through a critical value that triggers the GM-IM-GM transition.

Since our interest is in the GM-IM-GM eigenmode transition as γ_E evolves from $-\gamma_{E,\mathrm{GM}}$, through $\gamma_{E,\mathrm{IM}}$ to $\gamma_{E,\mathrm{GM}}$, we choose to remove the Floquet dynamics from this study and initiate our simulations with an eigenmode that is close to a fully developed GM (ballooning at $\theta \sim -\pi/2$ for $\gamma_E = -0.95\gamma_{E,\mathrm{GM}}$). We then ramp the flow-shear through the critical value ($\gamma_E = \gamma_{E,\mathrm{IM}} = 0$ for our parameters) to access the IM, and then hold the flow-shear fixed (at $\gamma_E = 0.95\gamma_{E,\mathrm{GM}}$) to obtain another GM (ballooning now at $\theta \sim \pi/2$). The rate of change of flow-shear, $\mathrm{d}\gamma_E/\mathrm{d}t$, is then considered on three distinct time-scales: (1) a sufficiently slow change such that the instability retains its eigenmode form as it evolves in response to $\gamma_E(t)$, with $\mathrm{d}\gamma_E/\mathrm{d}t$ = 1.0e-6; (2) a much faster ramp with $\mathrm{d}\gamma_E/\mathrm{d}t$ = 1.0e-4; and (3), in the limiting case of $\mathrm{d}\gamma_E/\mathrm{d}t \to \infty$, i.e. a sudden switch in γ_E. We discuss these cases in turn.

5.4.1 Mode response to slowly varying profiles

If the equilibrium profiles vary sufficiently slowly, the linear modes have time to respond and retain the eigenmode structure corresponding to the *instantaneous* plasma parameters. Figure 5.8a represents this scenario. We know that the evolving insta-

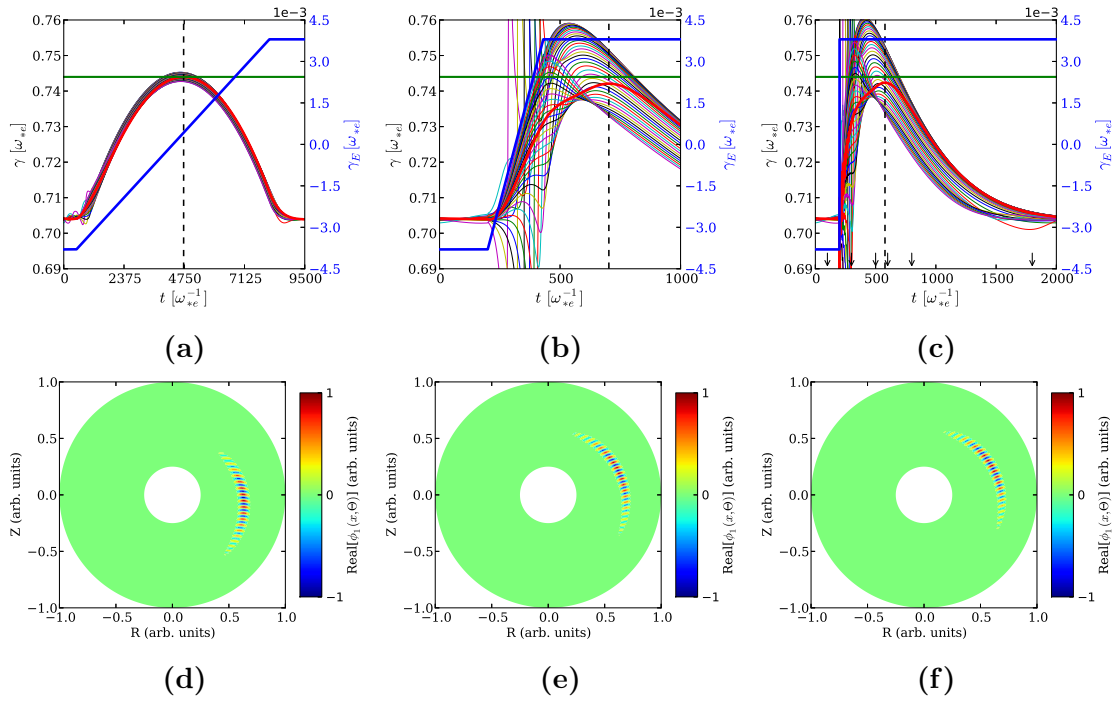

Figure 5.8: Plots (a)-(c) show the evolution of the growth rate of each Fourier mode (coloured curves) as a function of flow-shear γ_E (solid blue) for different $\mathrm{d}\gamma_E/\mathrm{d}t$. (d)-(f) show the corresponding mode-structures at the times when the instantaneous global growth rate is maximum, indicated by the dashed-vertical lines in the frames above. The green-horizontal line indicates the IM growth rate, whereas the solid-red line is the instantaneous global growth rate. Potential structures at the times annotated by the arrows in (c) can be seen in Fig. 5.9. [For $\omega_{*e} = 10^6$ Hz, 1000 units on the time-axis ~ 1 ms.]

bility is an eigenmode throughout since the plotted significant Fourier modes[3] have the same $\Omega_m(t)$ for each time point. Figure 5.8d shows the eigenfunction at the time when the global growth rate is the maximum (indicated by the dashed-vertical line in Fig. 5.8a). As expected, the mode balloons at $\theta = 0$ and has the same growth rate as the IM for $\gamma_E = \gamma_{E,\mathrm{IM}} = 0$. Note that this scenario is similar to Fig. 5.3, where *each* value of γ, for the corresponding γ_E, was obtained by running the simulation to long times with profiles held fixed in time.

5.4.2 Mode response to rapidly varying profiles

Changing the flow-shear over a much quicker time-scale (Fig. 5.8b) in turn leads to several interesting observations:

Coherent identity

If the profiles change rapidly, the evolving instability can no longer retain its eigenmode identity. This is apparent from the different growth rates $\gamma_m(t)$ associated with the significant Fourier harmonics (Fig. 5.8b). Nevertheless, the perturbation

[3]The significant Fourier modes are defined to be those with an amplitude greater than 1% of the global-mode amplitude envelope.

does retain a *coherent structure* as it rotates from the bottom of the plasma to the top with evolving γ_E. This characteristic is demonstrated in Fig. 5.9, but in the limit when $\mathrm{d}\gamma_E/\mathrm{d}t \to \infty$ (see section 5.4.3).

Strong growth

Even though some Fourier harmonics can transiently have growth rates greater than the IM, the global growth rate as defined in Section 4.3 never exceeds γ_{IM} for the parameters considered, but does transiently approach it. This may be expected since the IM is obtained by combining the amplitudes and phases of the Fourier modes to yield the maximum growth rate. What is intriguing, perhaps, is that $\max[\gamma(t)] \approx \gamma_{\mathrm{IM}}$ even though the structure is not exactly that of the eigenmode.

Profile lag

We observe that the growth rate peaks, approaching that of the IM, somewhat after γ_E has passed through its critical value for the IM. Further, referring to Fig. 5.8e, we note that this maximum in growth rate occurs after the mode has rotated past the outboard-midplane.

5.4.3 Mode response to a sudden profile switch

Finally, we ask what happens when the flow-shear passes through the critical value in the limit $\mathrm{d}\gamma_E/\mathrm{d}t \to \infty$, switching γ_E suddenly from negative to positive (Fig. 5.8c). We find that all the features discussed in section 5.4.2 are recovered. Note also that the global growth rate approaches γ_{IM} after only ~ 300 e-foldings, and then returns to the γ_{GM} value over a much longer period of ~ 1500 e-foldings. These numbers are approximately of the order it takes the IM and GM to establish their structures from noise.

5.4.4 Eigenmode-Floquet dynamics

So far, Floquet dynamics were removed from our GM-IM-GM transition studies by stopping the flow-shearing rate γ_E from going beyond $\gamma_{E,\mathrm{GM}}$. In Fig. 5.10a, we show that if γ_E is ramped beyond $\gamma_{E,\mathrm{GM}}$ at the same rate as for Fig. 5.8a, the mode develops into a Floquet Mode. If one ramps γ_E more slowly (so that the eigenmode can be treated in time more precisely) as in Fig. 5.10b, we find that the eigenmode performs two full Floquet cycles as γ_E exceeds $\gamma_{E,\mathrm{GM}}$, before settling to oscillate at the bottom of the tokamak (see γ around t = 8.4e4 in Fig. 5.10c). We return to consider the possible implications of this in ELM dynamics in Section 5.5.

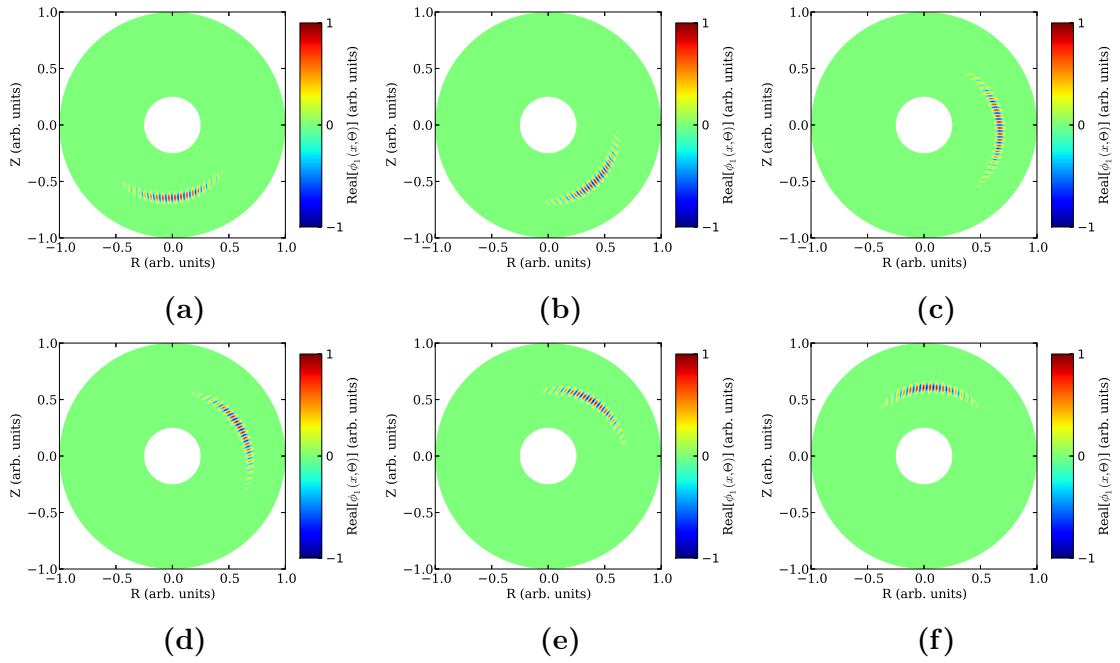

Figure 5.9: (a)-(f) show the poloidal mode-structure of the time evolving instability following a step in γ_E, with $\gamma_E < \gamma_{E,\mathrm{GM}}$ (chronologically at times indicated by arrows in Fig. 5.8c).

5.5 Summary

In the high-n limit, the higher-order ballooning eigenmode theory predicts two distinct linear mode structures (Isolated Mode and General Mode) for all toroidal microinstabilities (ITG, TEM, KBM etc.). While we consider the ITG mode as a specific example, we expect our results to be generic to most toroidal microinstabilities.

In Section 5.3, holding all plasma profiles fixed in time, we obtain both mode structures from our initial value approach and further characterise their behaviour leading up to the eigenmode formation. First, considering the eigenmode, we demonstrate that the GM, sitting at the bottom of the poloidal cross-section for a negative flow-shear, rotates to the top for a positive flow-shear, accessing the IM on the outboard side for an intermediate critical flow-shear. Note that if the direction of the curvature and ∇B drifts are reversed, the GM will then balloon at the bottom (top) for a positive (negative) flow-shear. It is interesting to note that Brower *et al* [87] in their study of the spatial and spectral distribution of tokamak microturbulence, observe a strong up-down asymmetry in the poloidal density fluctuation distribution along a vertical chord passing through the plasma centre, which inverts with current reversal. This could be connected to the presence of General Modes. Second, we find that for our strongly unstable cases, the GM structure takes ~ 1300 e-foldings to form from noise, while the IM takes considerably fewer ~ 300 e-foldings[4]. These values

[4]These timescales are found to be broadly similar for a range of initial conditions.

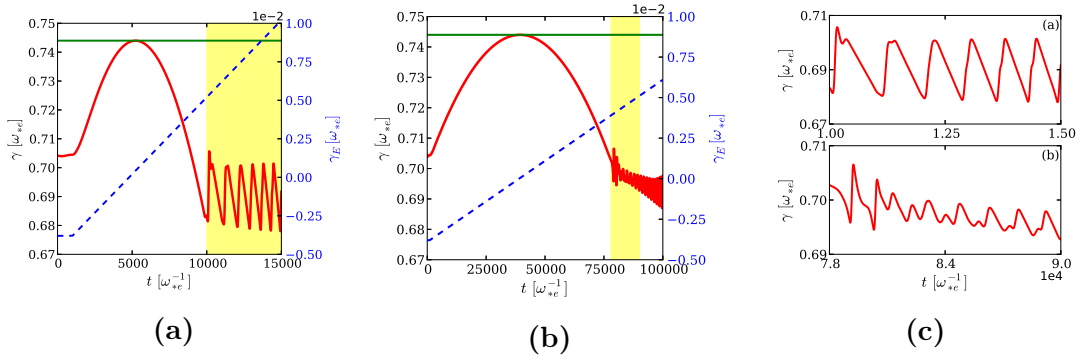

Figure 5.10: (a) shows the situation in Fig. 5.8a, except now the flow-shearing rate (dashed-blue line) has been pushed past the γ_E that would give a GM in the eigenmode limit (refer to Fig. 5.3); the case in (b) is for a much slower evolution of γ_E, with dγ_E/dt=1.0e-7. Plot (c) shows the magnified images of the shaded regions in (a) and (b).

indicate that, in this case, non-linear terms are likely to become important before the linear mode-structures can establish. However, we note that our fluid model is constrained to consider only strongly unstable modes. As we gradually increase η_s by 100%, we find that the global growth rate increases by over 80%, whereas the time to form the eigenmode only changes by 0.1%. Future studies should test these ideas in a more realistic plasma model - if the time to form the eigenmode remains insensitive to the linear drive when profiles are held close to marginal stability, then the linear dynamics may play an important role in the turbulence close to the linear threshold. Thirdly, for high linear flow-shears κ (equivalently, γ_E), we find the instability exhibits Floquet behaviour. The addition of a quadratic flow-profile $\kappa_1 y^2/n$ damps the Floquet oscillations so that $\gamma_{\rm FM}(t)$ approaches $\gamma_{\rm GM}$, as the Floquet Mode evolves towards the eigenmode, over $\mathcal{O}(n\kappa/\kappa_1)$ Floquet periods; this is in agreement with the theoretical predictions in ref. [205].

In Section 5.4, the response of these toroidal drift modes as the flow-shear is evolved through a critical value to trigger a GM-IM-GM transition was investigated. For small deviations from the critical flow-shear, i.e. $|\gamma_E| < \gamma_{E,\rm GM}$, the flow profile was changed over three time-scales. When the flow is varied on a slow time-scale compared to the eigenmode formation time, as the mode structure responds, it retains the instantaneous eigenmode form. However, when the flow profile was changed more rapidly, and subsequently in the limiting case of dγ_E/d$t \to \infty$, several interesting features emerge: (1) the evolving instability is no longer an eigenmode, but nevertheless maintains a coherent structure which is convected poloidally throughout the flow-ramp; (2) despite not being an eigenmode, the peak growth rate $\gamma_{\rm max} \sim \gamma_{\rm IM}$; (3) there is a noticeable lag, with $\gamma_{\rm max}$ realised some time after the profiles pass through the critical γ_E (which would give the IM for flows held fixed in time); and (4) the peak in growth rate occurs when the mode structure has rotated slightly beyond the outboard-midplane. Next when the flow-shear is taken into the $|\gamma_E| > \gamma_{E,\rm GM}$ regime, the presence of Floquet transients seem ubiquitous to our system. The parameter

$(\mathrm{d}^2\Omega_\phi)/(\mathrm{d}q\mathrm{d}t)$ strongly influences the eigenmode-Floquet dynamics and determines how closely the instability tracks an eigenmode.

Experimental test of theory

These results, although based on a relatively simple fluid-ITG model, are expected to be generic for all types of toroidal micro-instabilities, and thus provide some robust experimentally testable predictions:

(a) Towards understanding the origin of tokamak turbulence and the ubiquity/role of the General Mode, we remark that the density/potential/magnetic fluctuation measurements, viewed over a wide poloidal angle, should indicate asymmetries about the mid-plane, which would typically reverse when the direction of the ∇B drift is reversed.

(b) Further, if some small-ELM types are indeed triggered by the GM-IM-GM transition, data from the above diagnostic, resolved temporally between successive small-ELM bursts, should indicate *poloidally shifting* fluctuations at the time of ELM onset. This feature is expected to be quite robust, since the mode structure remains coherent with a strong growth rate, independent of how rapidly the profiles change. It is interesting to note that for a typical ω_{*e} = 10^6 Hz, the GM-IM-GM dynamics occur on the $\mathcal{O}(ms)$ time-scale characteristic of small-ELMs [182].

So far, the parameter controlling the transition between the GM and the IM has been an *externally imposed* toroidal flow-shear. However, there is strong evidence of *intrinsic* toroidal rotation in tokamaks [155], a likely source of which could be turbulent fluctuations themselves [161, 206, 207]. A self-consistent (quasi-linear) coupled system that accounts for the feedback of the turbulence on the flows is therefore explored in the next chapter.

Chapter 6

Self-consistent mode–flow interaction

In this chapter, we begin by presenting new analytical calculations of the intrinsic torque that is generated by the General Mode. The GM is of particular interest since these structures are predicted to be more generally accessible by the plasma. Next, a fluid plasma model is derived for the diffusion of the fluctuation-driven toroidal flow, which is coupled to the fluid-ITG model for the electrostatic fluctuation introduced in the previous chapters. The extended quasi-linear initial-value code is then utilised to study the interaction between the global modes, the residual intrinsic and equilibrium flows.

6.1 Toroidal momentum transport

The conservation of the toroidal angular momentum density P_ϕ yields an equation describing the evolution of the toroidal rotation in the presence of external sources and sinks S_ϕ [160, 189]:

$$\frac{\partial \langle P_\phi \rangle}{\partial t} + \frac{1}{V'} \frac{\partial}{\partial r} \left[V' \Gamma_\phi^r \right] = S_\phi \, . \tag{6.1}$$

Here V' denotes the radial derivative of the volume enclosed by a flux-surface at radius r and Γ_ϕ^r is the flux surface-averaged $\langle \, \rangle$ toroidal angular momentum density flux. The momentum flux is further expressed as:

$$\frac{\Gamma_\phi^r}{\langle n \rangle m R} = \chi_\phi \frac{\partial \langle v_\phi \rangle}{\partial r} + V_{co} \langle v_\phi \rangle + \Pi_{r,\phi} \, . \tag{6.2}$$

Here the term with the coefficient χ_ϕ characterises the diagonal, or diffusive, contribution; the Coriolis force due to the plasma rotation gives rise to the pinch, or convective, term with the coefficient V_{co} [208]; the final term $\Pi_{r,\theta}$ describes the 'residual' flux – essentially to do with symmetry-breaking [161]. As discussed in section 3.3.3, in devices such as ITER, we expect S_ϕ to be small in comparison to the intrinsic contributions arising from (for example) the electrostatic fluctuations simulated

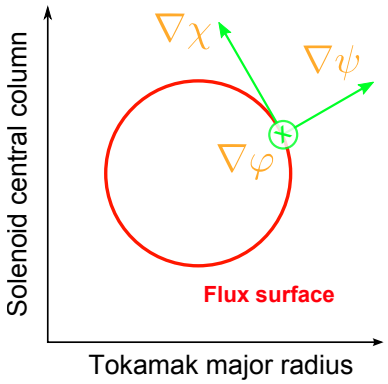

Figure 6.1: An orthogonal coordinate system defined by the poloidal flux ψ, the toroidal angle φ and the poloidal angle χ. Their gradients are shown in green.

here. Considering then the terms of eqn. 6.2, from the context of this work crucially, we note that the diffusive and convective terms are only weakly dependent on the ballooning angle θ_0 [189]. Since we are interested in the evolution of the IM ($\theta_0 = 0$) and GM ($\theta_0 = \pm\pi/2$) in the presence of intrinsic flows they generate, we only treat the Reynolds residual contribution $\Pi_{r,\theta}$. In the linear regime at least, this residual stress can be significant, comparing in magnitude to the diagonal term [189]. Note that there are in fact various symmetry-breaking mechanisms [161] – here we shall only consider the residual stress generated by the (r,θ) tilting of ballooning structures.

6.2 Reynolds stress in a tokamak

The Reynolds stress associated with fluctuations is expected to generate a torque that spins the plasma. This torque takes the form [184]

$$\frac{\partial\langle\mathbf{v}\rangle}{\partial t} = -\langle(\mathbf{u}.\nabla)\mathbf{u}\rangle \ , \tag{6.3}$$

where $\mathbf{v}$ is the plasma flow, $\mathbf{u} = (\mathbf{B}\times\nabla\phi)/B^2$ is calculated from the electrostatic potential fluctuation. In a steady-state, this intrinsic torque is balanced by a viscous-drag term (and any external source of torque). To calculate $\mathbf{u}$, we adopt the orthogonal coordinate system described in Fig. 6.1. Following Appendix A, we define the magnetic field on a flux-surface as

$$\mathbf{B} = f\nabla\varphi + \nabla\varphi\times\nabla\psi \tag{6.4}$$

($f = RB_\varphi$ is constant on a flux-surface). In this coordinate system

$$\nabla = \nabla\varphi\frac{\partial}{\partial\varphi} + \nabla\chi\frac{\partial}{\partial\chi} + \nabla\psi\frac{\partial}{\partial\psi} \ , \tag{6.5}$$

$$\mathbf{u} = u_\varphi\frac{\nabla\varphi}{|\nabla\varphi|} + u_\chi\frac{\nabla\chi}{|\nabla\chi|} + u_\psi\frac{\nabla\psi}{|\nabla\psi|} \ . \tag{6.6}$$

It can be seen that $|\nabla\varphi| = R^{-1}$. Next, taking the dot product of eqn. 6.4 with the poloidal field $\mathbf{B_p}$, we find $|\nabla\psi| = RB_p$. Finally, noting that the Jacobian J is related to the volume of the parallelepiped defined in this coordinate by $(\nabla\varphi\times\nabla\psi).\nabla\chi = J^{-1}$, we deduce $|\nabla\chi| = (JB_p)^{-1}$.

The components of $\mathbf{u}$ in this coordinate are next evaluated:

$$\begin{aligned} u_\varphi = \frac{\mathbf{u}.\nabla\varphi}{|\nabla\varphi|} &= \frac{R}{B^2}\left(\mathbf{B}\times\nabla\phi\right).\nabla\varphi = \frac{R}{B^2}\left(\nabla\varphi\times\mathbf{B}\right).\nabla\phi \\ &= \frac{R}{B^2}\left[\nabla\varphi\times\left(\nabla\varphi\times\nabla\psi\right)\right].\nabla\phi \\ &= -\frac{R}{B^2}|\nabla\varphi|^2\nabla\psi.\nabla\phi \\ &= -\frac{R}{B^2}|\nabla\varphi|^2|\nabla\psi|^2\frac{\partial\phi}{\partial\psi} \\ &= -\frac{RB_p^2}{B^2}\frac{\partial\phi}{\partial\psi}\,; \end{aligned}$$

$$\begin{aligned} u_\chi = \frac{\mathbf{u}.\nabla\chi}{|\nabla\chi|} &= \frac{JB_p}{B^2}\left(\mathbf{B}\times\nabla\phi\right).\nabla\chi = -\frac{JB_pf}{B^2}\left(\nabla\varphi\times\nabla\chi\right).\nabla\phi \\ &= -\frac{JB_pf}{B^2}\left[\nabla\varphi\times\frac{\left(\nabla\varphi\times\nabla\psi\right)}{JB_p^2}\right].\nabla\phi \\ &= \frac{f}{B^2B_p}\left[|\nabla\varphi|^2\nabla\psi\right].\nabla\phi \\ &= \frac{fB_p}{B^2}\frac{\partial\phi}{\partial\psi}\,, \end{aligned}$$

$$\begin{aligned} u_\psi = \frac{\mathbf{u}.\nabla\psi}{|\nabla\psi|} &= \frac{1}{RB_pB^2}\left(\nabla\psi\times\mathbf{B}\right).\nabla\phi \\ &= \frac{1}{RB_pB^2}\left(R^2B^2\nabla\varphi - f\mathbf{B}\right).\nabla\phi \\ &\approx \frac{1}{RB_p}\frac{\partial\phi}{\partial\varphi}\,; \end{aligned}$$

Here we have treated the parallel derivative $\mathbf{B}.\nabla\phi \approx 0$. Collecting the above terms:

$$\mathbf{u} = \left[-\frac{R^2B_p^2}{B^2}\frac{\partial\phi}{\partial\psi}\right]\nabla\varphi + \left[\frac{f}{B^2}\frac{\partial\phi}{\partial\psi}\right]\nabla\varphi\times\nabla\psi + \left[\frac{1}{R^2B_p^2}\frac{\partial\phi}{\partial\varphi}\right]\nabla\psi\,. \tag{6.7}$$

To estimate the intrinsic torque generated in the toroidal direction, we evaluate $(\mathbf{u}.\nabla)u_\varphi$. With the help of eqn. 6.4, which allows us to neglect the parallel derivative,

eqn. 6.7 yields

$$(\mathbf{u}.\nabla)u_\varphi = \frac{B_p^2}{B^2}\frac{\partial\phi}{\partial\psi}\frac{\partial}{\partial\varphi}\left(\frac{RB_p^2}{B^2}\frac{\partial\phi}{\partial\psi}\right) + \frac{B_\phi^2}{B^2}\frac{\partial\phi}{\partial\psi}\frac{\partial}{\partial\varphi}\left(\frac{RB_p^2}{B^2}\frac{\partial\phi}{\partial\psi}\right) - \frac{\partial\phi}{\partial\varphi}\frac{\partial}{\partial\psi}\left(\frac{RB_p^2}{B^2}\frac{\partial\phi}{\partial\psi}\right) \quad (6.8)$$

$$= \frac{\partial\phi}{\partial\psi}\frac{\partial}{\partial\varphi}\left(\frac{RB_p^2}{B^2}\frac{\partial\phi}{\partial\psi}\right) - \frac{\partial\phi}{\partial\varphi}\frac{\partial}{\partial\psi}\left(\frac{RB_p^2}{B^2}\frac{\partial\phi}{\partial\psi}\right) \quad (6.9)$$

$$= \frac{RB_p^2}{2B^2}\left[\frac{\partial}{\partial\varphi}\left(\frac{\partial\phi}{\partial\psi}\right)^2\right] - \left\{\frac{\partial}{\partial\psi}\left(\frac{RB_p^2}{B^2}\frac{\partial\phi}{\partial\psi}\frac{\partial\phi}{\partial\varphi}\right) - \frac{RB_p^2}{2B^2}\left[\frac{\partial}{\partial\varphi}\left(\frac{\partial\phi}{\partial\psi}\right)^2\right]\right\} . \quad (6.10)$$

Integrating over the periodic variable φ, the first and third terms vanish:

$$\oint (\mathbf{u}.\nabla)u_\varphi \,\mathrm{d}\varphi = -\frac{\partial}{\partial\psi}\oint \frac{RB_p^2}{B^2}\frac{\partial\phi}{\partial\psi}\frac{\partial\phi}{\partial\varphi}\,\mathrm{d}\varphi . \quad (6.11)$$

To find the net torque, the velocity is first expressed as

$$\mathbf{u} = u_\varphi\mathbf{e}_\varphi + u_\chi\mathbf{e}_\chi = u_\parallel\mathbf{e}_\parallel + \hat{u}_\varphi\mathbf{e}_\varphi \quad (6.12)$$

(here $\mathbf{e}_\chi$ is the unit vector along χ, etc.). In order to calculate the Doppler shift which arises from the $\mathbf{u}.\nabla$ convective derivative, we note that $\mathbf{u}.\nabla \approx \hat{u}_\varphi\mathbf{e}_\varphi.\nabla$. We therefore need to evaluate $\hat{u}_\varphi$. From the relations $\mathbf{B} = B\mathbf{e}_\parallel = B_\phi\mathbf{e}_\varphi + B_p\mathbf{e}_\chi$, $u_\chi = u_\parallel(B_p/B)$ and $u_\chi = -(B_\phi/B_p)u_\varphi$, we derive

$$\hat{u}_\varphi = u_\varphi - u_\chi(B_\phi/B_p) \quad (6.13)$$

$$= \frac{B_\phi^2}{B_p^2}\left(1 + \frac{B_p^2}{B_\phi^2}\right)u_\varphi . \quad (6.14)$$

Then, the torque that spins $\hat{u}_\varphi$ is given by eqn. 6.11 with a factor $(1 + B_\phi^2/B_p^2)$ upfront:

$$\frac{\partial\langle\mathbf{v}\rangle}{\partial t} = T_q = \frac{\partial}{\partial\psi}\oint \frac{f^2}{RB^2}\left(1 + \frac{B_p^2}{B_\phi^2}\right)\frac{\partial\phi}{\partial\psi}\frac{\partial\phi}{\partial\varphi}\,\mathrm{d}\varphi \quad (6.15)$$

(note sign change from eqn. 6.3). To estimate the torque associated with the global mode structures, we adopt the Fourier-ballooning representation (eqn. 5.24):

$$\phi = \mathcal{R}\left[\mathrm{e}^{-\mathrm{i}\Omega t}\mathrm{e}^{\mathrm{i}n\varphi}\int_{-\infty}^{\infty}\xi(\psi,p,\theta)\mathrm{e}^{-\mathrm{i}m_0\theta}\mathrm{e}^{-\mathrm{i}y(\theta-p)}A(p)\,\mathrm{d}p\right] . \quad (6.16)$$

Here $\mathcal{R}$ represents the real part of the complex potential. Provided we remain close to ψ_s (ψ and r have been used interchangeably), $A(p)$ is seen to satisfy eqn. 5.42:

$$\frac{\Omega_{xx}}{2n^2q'^2}\frac{\mathrm{d}^2A}{\mathrm{d}p^2} - \frac{\mathrm{i}\Omega_x}{nq'}\frac{\mathrm{d}A}{\mathrm{d}p} + [\Omega - \Omega_0(p)]\,A = 0 . \quad (6.17)$$

Here Ω is the global mode's complex frequency and $\Omega_0(x,p) = \Omega_0(p) + \Omega_x(p)x +$

$\Omega_{xx}(p)x^2/2 + \ldots$ is the local eigenvalue.

6.2.1 Model assumptions

If we are close to the maximum in the linear growth rate (at $\psi = \psi_s$), then Ω_x is approximately real. From the convective derivative, we see that the toroidal flow-shear modifies the real frequency through a Doppler shift $\Omega \to \Omega + n\Omega'_\varphi x$ (assuming a linear flow-shear Ω'_φ). Equilibrium profiles also introduce a variation to Ω_x, but $\Omega_x \approx n\Omega'_\varphi$ due to the large parameter n. However, Ω_{xx} is complex in general and approximately $n\Omega''_\varphi$ (in our specific case, $\Omega_{xx} = 0$). Finally note, since we are working in a frame where the rational surface ψ_s is at rest, $\Omega_0(p)$ is $\mathcal{O}(1)$ due to profile variations in p.

6.2.2 Analytical estimation

With these assumptions, we may drop the first term of eqn. 6.17, which is $\mathcal{O}(1/n)$ (this forbids the IM and we can only consider the GM), and integrate to write

$$A(p) = \exp\left[-\frac{inq'}{\Omega_x}\int^p (\Omega - \Omega_0(p))\,\mathrm{d}p\right] . \tag{6.18}$$

Periodicity of ϕ in θ requires that $A(p)$ is periodic in p, i.e. $A(p+2\pi)/A(p) = 1 = \exp(\mathrm{i}2\pi N)$ for any integer N. Using this condition we derive

$$\Omega = \frac{1}{2\pi}\oint \Omega_0(p)\,\mathrm{d}p - \frac{\Omega_x}{nq'}N \tag{6.19}$$

$$= \langle\Omega_0(p)\rangle - \frac{\Omega_x}{nq'}N \tag{6.20}$$

Defining a new perturbed quantity

$$\tilde{\Omega}(p) = \Omega_0(p) - \langle\Omega_0(p)\rangle , \tag{6.21}$$

we may express

$$A(p) = \exp\left[\frac{inq'}{\Omega_x}\int^p \tilde{\Omega}(p)\,\mathrm{d}p\right]\exp\left(\mathrm{i}Np\right) . \tag{6.22}$$

The electrostatic potential is now written as

$$\phi = \mathcal{R}\left[\mathrm{e}^{-\mathrm{i}\Omega t}\mathrm{e}^{\mathrm{i}n\varphi}\int_{-\infty}^{\infty}\xi(\psi,p,\theta)\mathrm{e}^{-\mathrm{i}m_0\theta}\mathrm{e}^{-\mathrm{i}y\theta}\mathrm{e}^{\mathrm{i}nq'S(p)}\,\mathrm{d}p\right] \tag{6.23}$$

$$= \mathcal{R}\left[\mathrm{e}^{-\mathrm{i}\Omega t}\mathrm{e}^{\mathrm{i}n\varphi}\phi_n\right] , \tag{6.24}$$

where

$$S(p) = \left(x + \frac{N}{nq'}\right)p + \frac{1}{\Omega_x}\int^p \tilde{\Omega}(p)\,\mathrm{d}p . \tag{6.25}$$

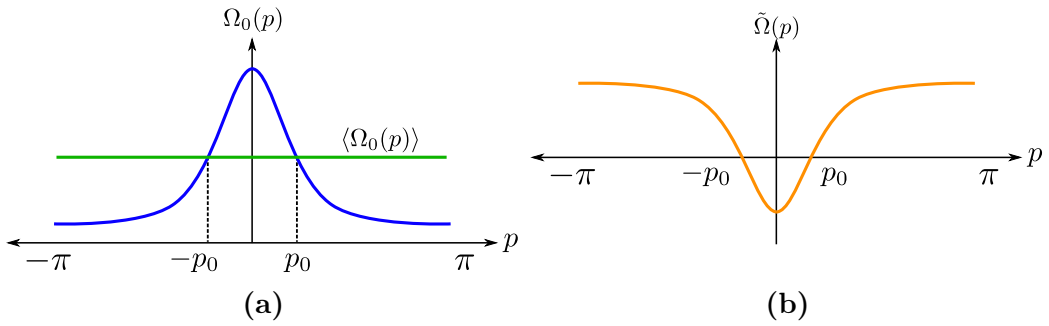

Figure 6.2: (a) shows a typical variation of $\Omega_0(p)$ in the periodic p domain (blue). The General Mode eigenvalue (green) is obtained by averaging $\Omega_0(p)$ over the complete period (section 5.2.5.3). (b) illustrates why $\tilde{\Omega}(p) = 0$ at $p = \pm\pi/2$ in a circular cross-section geometry. Note that in our model, this variation is assumed to be sinusoidal.

Note that the integer N simply shifts $x = \psi - \psi_s$ by N rational surfaces, i.e. labels different global mode solutions on various ψ_s. Since these structures evolve independently in the linear regime, we only consider a single mode labelled by $N = 0$. To evaluate the integral given by eqn. 6.24, we can use the method of stationary phase. Accordingly, the integral receives the dominant contribution from the region around p where $S(p)$ is stationary, i.e. $\mathrm{d}S(\hat{p})/\mathrm{d}p = 0$. This is given by

$$\tilde{\Omega}(\hat{p}) = -\Omega_x x \,. \tag{6.26}$$

To evaluate $\hat{p}$, expand

$$\tilde{\Omega}(\hat{p}) \approx \tilde{\Omega}(p_0) + \tilde{\Omega}_p(\hat{p} - p_0) \tag{6.27}$$

around the region where $\tilde{\Omega}(p_0) = 0$. For our circular cross-section model, $p_0 = \pm\pi/2$ (see Fig. 6.2 for a pictorial description). The correct sign of p_0 is determined by the ∇B drift and is such that the integral for ϕ converges. We solve for $\hat{p}$ to find

$$\hat{p} = p_0 - \frac{\Omega_x x}{\tilde{\Omega}_p(p_0)} \,. \tag{6.28}$$

Taylor-expanding $S(p)$ around $\hat{p}$:

$$S(p) = S(\hat{p}) + \frac{S''(\hat{p})}{2}(p - \hat{p})^2 + \ldots \tag{6.29}$$

$$= xp_0 - \frac{\Omega_x x^2}{\tilde{\Omega}_p(p_0)} + \frac{1}{\Omega_x}\int^{\hat{p}} \tilde{\Omega}\,\mathrm{d}p + \frac{\tilde{\Omega}_p(\hat{p})}{2\Omega_x}(p - \hat{p})^2 \,. \tag{6.30}$$

Using this stationary phase approximation for $S(p)$, we may express eqn. 6.24 as

$$\phi_n = \mathrm{e}^{-\mathrm{i}y\theta}\mathrm{e}^{-\mathrm{i}m_0\theta}\mathrm{e}^{\mathrm{i}nq'p_0x}\mathrm{e}^{-\frac{\mathrm{i}nq'\Omega_x}{2\tilde{\Omega}_p(p_0)}x^2}\mathrm{e}^{\frac{1}{\Omega_x}\int^{\hat{p}}\tilde{\Omega}\,\mathrm{d}p}\int_{-\infty}^{\infty}\xi\exp\left[\frac{\mathrm{i}nq'\tilde{\Omega}_p(\hat{p})}{2\Omega_x}(p-\hat{p})^2\right]\mathrm{d}p \,. \tag{6.31}$$

For the integral over p to be defined, the imaginary component of $\tilde{\Omega}_p$, $\mathcal{I}(\tilde{\Omega}_p)$, must be positive. This simultaneously ensures that the Gaussian in x does not diverge as $x \to \infty$. We next define three new complex variables

$$\sigma = \frac{\mathrm{i}q'\Omega_x}{2\tilde{\Omega}_p(p_0)}, \quad \mu = -\frac{\mathrm{i}q'\tilde{\Omega}_p(\hat{p})}{2\Omega_x} \quad \text{and} \quad k = \sqrt{\mu n}(p-\hat{p}) \,. \tag{6.32}$$

This allows us to write (absorbing any constant term in C):

$$\phi_n = \frac{C}{\sqrt{\mu n}} \mathrm{e}^{-\mathrm{i}m_0\theta} \mathrm{e}^{-n\sigma x^2} \mathrm{e}^{-\mathrm{i}nq'x(\theta-p_0)} \int_{-\infty}^{\infty} \mathrm{e}^{-k^2} \xi\left(\psi, \hat{p} + \frac{k}{\sqrt{\mu n}}, \theta\right) \mathrm{d}k \tag{6.33}$$

$$= \frac{C}{\sqrt{\mu n}} \mathrm{e}^{-\mathrm{i}m_0\theta} \mathrm{e}^{-n\sigma x^2} \mathrm{e}^{-\mathrm{i}nq'x(\theta-p_0)} \int_{-\infty}^{\infty} \mathrm{e}^{-k^2} \left[\xi(\hat{p}) + \frac{\partial \xi}{\partial p}\frac{k}{\sqrt{\mu n}} + \frac{\partial^2 \xi}{\partial p^2}\frac{k^2}{\mu n} + \dots\right] \mathrm{d}k \tag{6.34}$$

$$= \frac{C}{\sqrt{\mu n}} \mathrm{e}^{-\mathrm{i}m_0\theta} \mathrm{e}^{-n\sigma x^2} \mathrm{e}^{-\mathrm{i}nq'x(\theta-p_0)} \left[\xi(\hat{p})\sqrt{\pi} + \mathcal{O}\left(\frac{1}{\mu n}\frac{\partial^2 \xi}{\partial p^2}\right)\right] \tag{6.35}$$

$$\approx C\sqrt{\frac{\pi}{\mu n}} \mathrm{e}^{-\mathrm{i}m_0\theta} \mathrm{e}^{-n\sigma x^2} \mathrm{e}^{-\mathrm{i}nq'x(\theta-p_0)} \xi(\psi, \hat{p}, \theta) \,. \tag{6.36}$$

In the steps above, ξ has been Taylor-expanded in k about $\hat{p}$, and the integral involving the odd-function in k has gone to zero. Next writing $\sigma = \sigma_r + \mathrm{i}\sigma_i$ and $\xi = |\xi|\exp(\mathrm{i}F)$ (where F is a slowly varying function of ψ, equivalently x), we derive

$$\phi = \mathcal{R}\left[\mathrm{e}^{-\mathrm{i}\Omega t} \mathrm{e}^{\mathrm{i}n\varphi} \mathrm{e}^{-\mathrm{i}m_0\theta} \mathrm{e}^{-n\sigma_r x^2} \mathrm{e}^{-\mathrm{i}n\sigma_i x^2} \mathrm{e}^{-\mathrm{i}nq'x(\theta-p_0)} |\xi| \mathrm{e}^{\mathrm{i}F}\right] \tag{6.37}$$

$$= \mathrm{e}^{-n\sigma_r x^2} |\xi| \cos\left[n\varphi - m_0\theta - n\sigma_i x^2 - nq'x(\theta-p_0) + F - \Omega t\right] \tag{6.38}$$

$$= \mathrm{e}^{-n\sigma_r x^2} |\xi| \cos\lambda \,. \tag{6.39}$$

Here we have dropped the constant factors. We are interested in calculating the terms of eqn. 6.15. Towards this we evaluate:

$$\frac{\partial \phi}{\partial \varphi} = -n\mathrm{e}^{-n\sigma_r x^2} |\xi| \sin\lambda \tag{6.40}$$

$$\frac{\partial \phi}{\partial \psi} = \mathrm{e}^{-n\sigma_r x^2}\left[\cos\lambda \frac{\partial |\xi|}{\partial \psi} - 2n\sigma_r x|\xi|\cos\lambda - |\xi|\sin\lambda\left(-nq'(\theta-p_0) - 2n\sigma_i x + \frac{\partial F}{\partial \psi}\right)\right] \tag{6.41}$$

Noting that

$$\int_0^{2\pi} \sin(\alpha x + \beta)\cos(\alpha x + \beta)\,\mathrm{d}x = 0 \quad \text{and} \quad \int_0^{2\pi} \sin^2(\alpha x + \beta)\mathrm{d}x = \frac{\pi}{\alpha} \tag{6.42}$$

for any integer α, we derive

$$\oint \frac{\partial \phi}{\partial \psi}\frac{\partial \phi}{\partial \varphi}\,\mathrm{d}\varphi = -\pi \mathrm{e}^{-2n\sigma_r x^2} |\xi|^2 \left[nq'(\theta-p_0) + 2n\sigma_i x - \frac{\partial F}{\partial \psi}\right] . \tag{6.43}$$

The flux-average of a quantity Ψ in our coordinate system is expressed as

$$\langle\Psi\rangle = \frac{\oint \mathrm{d}\varphi \oint \mathrm{d}\chi RJB_p\Psi}{\oint \mathrm{d}\varphi \oint \mathrm{d}\chi RJB_p} \,. \tag{6.44}$$

For a circular cross-section, noting $|\nabla\chi| = 1/r$, it is seen that $J\mathrm{d}\chi = (r/B_p)\mathrm{d}\theta$. This implies $RJB_p\mathrm{d}\chi = (R^3B_pq/f)\mathrm{d}\theta$. The surface-averaged torque is therefore

$$\langle T_q\rangle = G\left[\oint \mathrm{d}\theta \oint \mathrm{d}\varphi R^3B_p\frac{\partial}{\partial\psi}\left\{\frac{f^2}{RB^2}\left(1+\frac{B_p^2}{B_\phi^2}\right)\frac{\partial\phi}{\partial\psi}\frac{\partial\phi}{\partial\varphi}\right\}\right]\left[2\pi\oint R^3B_p\mathrm{d}\theta\right]^{-1} \,. \tag{6.45}$$

The parameter G is a scale factor that sets the saturation amplitude for ϕ. Using eqn. 6.43 and only taking radial derivatives of terms with the large parameter n upfront:

$$\begin{aligned}
\frac{\partial\langle\hat{V}_\varphi\rangle}{\partial t} &= -G\pi\left[\oint \mathrm{d}\theta\, R^3B_p\frac{f^2}{RB^2}\left(1+\frac{B_p^2}{B_\phi^2}\right)\frac{\partial}{\partial\psi}\left\{\mathrm{e}^{-2n\sigma_r x^2}|\xi|^2\left[nq'(\theta-p_0)+\right.\right.\right.\\
&\qquad \left.\left.\left. 2n\sigma_i x-\frac{\partial F}{\partial\psi}\right]\right\}\right]\left[2\pi\oint R^3B_p\mathrm{d}\theta\right]^{-1}\\
&= -G\pi\left[\oint \mathrm{d}\theta\,\frac{f^2B_pR^2}{B^2}\left(1+\frac{B_p^2}{B_\phi^2}\right)|\xi|^2\mathrm{e}^{-2n\sigma_r x^2}\left\{2n\sigma_i-4n\sigma_r x\left[nq'(\theta-p_0)+\right.\right.\right.\\
&\qquad \left.\left.\left. 2n\sigma_i x-\frac{\partial F}{\partial\psi}\right]\right\}\right]\left[2\pi\oint R^3B_p\mathrm{d}\theta\right]^{-1}\\
&\approx +G\pi\left[\oint \mathrm{d}\theta\,\frac{f^2B_pR^2}{B^2}\left(1+\frac{B_p^2}{B_\phi^2}\right)|\xi|^2\mathrm{e}^{-2n\sigma_r x^2}4n^2q'\sigma_r x(\theta-p_0)\right]\left[2\pi\oint R^3B_p\mathrm{d}\theta\right]^{-1}
\end{aligned}$$

In the last step we only keep the term with the highest power in n. Note that $8n^2\sigma_r\sigma_i x^2$ has been neglected since, across the mode width, $x \sim \mathcal{O}(1/\sqrt{n})$. Next, defining a new flux-function $Q(\psi)$ that excludes all but equilibrium scale radial variations

$$Q(\psi) = \left[\oint \mathrm{d}\theta\,\frac{f^2B_pR^2}{B^2}\left(1+\frac{B_p^2}{B_\phi^2}\right)|\xi|^2(\theta-p_0)\right]\left[2\pi\oint R^3B_p\mathrm{d}\theta\right]^{-1} \,, \tag{6.46}$$

we arrive at the equation

$$\frac{\partial\langle\hat{V}_\varphi\rangle}{\partial t} = \hat{G}q'\sigma_r x\mathrm{e}^{-2n\sigma_r x^2}Q(\psi) \,. \tag{6.47}$$

Here G has been rescaled to $\hat{G}$ to absorb all constants (including n). Noting that $\sigma_r = \mathcal{I}(\tilde{\Omega}_p)(q'\Omega_x)(2|\tilde{\Omega}_p|^2)^{-1}$, where $\mathcal{I}$ denotes the imaginary part of a complex quantity,

we see

$$\frac{\partial\langle\hat{V}_\varphi\rangle}{\partial t} = \frac{\hat{G}q'^2}{2|\tilde{\Omega}_p|^2}\mathcal{I}(\tilde{\Omega}_p)x\Omega_x \mathrm{e}^{-2n\sigma_r x^2}Q(\psi) \tag{6.48}$$

$$= \hat{H}\mathcal{I}(\tilde{\Omega}_p)Q(\psi)\hat{V}_\varphi \, . \tag{6.49}$$

We have written $x\Omega_x = \hat{V}_\varphi/R$ and defined $\hat{H}$ to absorb all the positive factors. This has the solution

$$\langle\hat{V}_\varphi\rangle = \langle\hat{V}_{\varphi,0}\rangle \, \mathrm{e}^{\kappa t} \, , \tag{6.50}$$

where $\kappa = \hat{H}\mathcal{I}(\tilde{\Omega}_p)Q(\psi)$. Recall that $\mathcal{I}(\tilde{\Omega}_p) > 0$. Then, depending on the sign of $Q(\psi)$, two situations may arise:

(a) For arbitrary flow-shear and general profiles, only the GM is expected to exist. But the associated Reynolds stress as the plasma tries to establish this mode, would damp the flow and drive $\Omega_x \to 0$ (provided $Q(\psi) < 0$), triggering the IM.

(b) If the sign is opposite, or the Isolated Mode is associated with non-zero Reynolds stress, this is likely to spin up the plasma. However, this cannot happen without bound, and it is reasonable to speculate that some physical mechanism eventually constrains $\kappa \leq 0$.

6.3 A model for Reynolds stress and flow diffusion

To derive a model for the effect of Reynolds stress on the background flow, we start with the Navier-Stokes equation

$$\rho\left[\frac{\partial\mathbf{u}}{\partial t} + (\mathbf{u}.\nabla)\mathbf{u}\right] = -\nabla p + \mu\nabla^2\mathbf{u} + \mathbf{F} \, . \tag{6.51}$$

Here, ρ is the mass density, $\mathbf{u}$ is the fluid velocity and μ the viscosity. The term $\mathbf{F}$ describes 'body forces', i.e. forces acting on the fluid particles at a distance (e.g. gravity, magnetic field)[1]. Making use of the Einstein notation,

$$\rho\left[\partial_t u_i + u_j\partial_j u_i\right] = -\partial_i p + \mu\nabla^2 u_i + F_i \, . \tag{6.52}$$

Noting $u_j\partial_j u_i = \partial_j(u_i u_j) - u_i\partial_j u_j$ and assuming incompressibility, i.e. $\partial_j u_j = 0$:

$$\rho\left[\partial_t u_i + \partial_j(u_i u_j)\right] = -\partial_i p + \mu\nabla^2 u_i + F_i \, . \tag{6.53}$$

Next, each instantaneous component, such as the velocity u_i, is written as a sum of its time-averaged ($\bar{u}_i$) and fluctuating ($\tilde{u}_i$) parts. By definition, the time average of

[1]Contrast this to 'surface forces', which are due to direct contact with other fluid particles.

a random fluctuation is zero. For the quantities $a = \bar{a} + \tilde{a}$, $b = \bar{b} + \tilde{b}$ and the constant c, Reynolds' rules of averages imply:

$$\overline{a+b} = \bar{a} + \bar{b}\,; \qquad \overline{ca} = c\bar{a}\,; \qquad \overline{ab} = \bar{a}\bar{b} + \overline{\tilde{a}\tilde{b}}\,; \qquad \overline{\frac{\partial a}{\partial x}} = \frac{\partial \bar{a}}{\partial x}\,. \tag{6.54}$$

Decomposing each term in eqn. 6.53 into its mean and fluctuating components, and averaging over time:

$$\rho\left[\partial_t \bar{u}_i + \partial_j\left(\overline{\tilde{u}_i\tilde{u}_j}\right) + \partial_j\left(\bar{u}_i\bar{u}_j\right)\right] = -\partial_i\bar{p} + \mu\nabla^2\bar{u}_i + \bar{F}_i\,.$$

Defining the slab coordinates (x is radial, y is poloidal and z toroidal) and averaging over the periodic y direction $\langle\ \rangle$:

$$\rho\left[\partial_t\langle\bar{u}_i\rangle + \partial_j\left\langle\overline{\tilde{u}_i\tilde{u}_j}\right\rangle + \partial_j\left\langle\bar{u}_i\bar{u}_j\right\rangle\right] = -\partial_i\langle\bar{p}\rangle + \mu\nabla^2\langle\bar{u}_i\rangle + \langle\bar{F}_i\rangle. \tag{6.55}$$

The incompressibility condition yields $\partial_x\langle\bar{u}_x\rangle + \partial_y\langle\bar{u}_y\rangle + \partial_z\langle\bar{u}_z\rangle = 0$. Assuming axisymmetry, $\partial_z \to 0$, and noting $\partial_y\langle\ \rangle = 0$, we have $\bar{u}_x = 0$ (charge conservation implies that $\overline{u}_x$ cannot be a non-zero constant). Now consider the radial variation (i.e. $j \to x$) to the Reynolds stress in eqn. 6.55:

$$\rho\left[\partial_t\langle\bar{u}_i\rangle + \partial_x\left\langle\overline{\tilde{u}_i\tilde{u}_x}\right\rangle\right] = -\partial_i\langle\bar{p}\rangle + \mu\partial_x^2\langle\bar{u}_i\rangle + \langle\bar{F}_i\rangle. \tag{6.56}$$

In a plasma, the dominant body-force is $\mathbf{J}\times\mathbf{B}$. Noting that the time-averaged radial current density $\bar{J}_x = 0$ and $\mathbf{B} = B_y\hat{y} + B_z\hat{z}$, we find $\bar{F}_x = \bar{J}_y B_z - \bar{J}_z B_y$ and $\bar{F}_y = \bar{F}_z = 0$. Equation 6.56 can now be written for the x, y and z components:

$$\begin{aligned}
\hat{x}\ :&\quad \rho\left[\partial_x\left\langle\bar{\tilde{u}}_x^2\right\rangle\right] = -\partial_x\langle\bar{p}\rangle + \langle\bar{F}_x\rangle \quad ,\\
\hat{y}\ :&\quad \rho\left[\partial_x\left\langle\overline{\tilde{u}_y\tilde{u}_x}\right\rangle\right] = 0 \quad ,\\
\hat{z}\ :&\quad \rho\left[\partial_t\langle\bar{u}_z\rangle + \partial_x\left\langle\overline{\tilde{u}_z\tilde{u}_x}\right\rangle\right] = \mu\partial_x^2\langle\bar{u}_z\rangle \quad .
\end{aligned}$$

Here we have treated $\bar{u}_y \approx 0$ due to neoclassical magnetic damping (as discussed in section 4.2.1, this provides a relationship between the predominant toroidal and perpendicular flows). The x component provides a small correction to the radial pressure-balance, whereas the z component provides an equation for the evolution of the toroidal velocity. Considering again the dominant $E\times B$ drift:

$$\tilde{u}_x = -\frac{\partial_y\phi}{B} \quad \text{and} \qquad \tilde{u}_z = -\frac{B_y\partial_x\phi}{B^2}$$

(assuming $B_z \approx B$). Finally, in the slab/toroidal coordinate, the evolution equation for the toroidal velocity due to the fluctuation induced Reynolds stress is:

$$\frac{\partial\langle\bar{u}_z\rangle}{\partial t} + \frac{B_y}{B^3}\frac{\partial}{\partial x}\left\langle\overline{\frac{\partial\phi}{\partial x}\frac{\partial\phi}{\partial y}}\right\rangle = \nu\frac{\partial^2\langle\bar{u}_z\rangle}{\partial x^2}$$
$$\frac{\partial\langle\bar{u}_\phi\rangle}{\partial t} + \frac{B_\theta}{B^3}\frac{\partial}{\partial \psi}\left\langle\overline{\frac{1}{\psi_s}\frac{\partial\phi}{\partial\psi}\frac{\partial\phi}{\partial\theta}}\right\rangle = \nu\frac{\partial^2\langle\bar{u}_\phi\rangle}{\partial\psi^2}$$

(here $\nu = \mu/\rho$ is the momentum diffusivity and ψ_s is a reference flux surface). Finally, with $u_\phi \approx R_0\Omega_\phi$, where R_0 is the major radius, we obtain an equation describing the evolution of the toroidal rotation frequency Ω_ϕ in the presence of fluctuation-induced flows:

$$\frac{\partial\langle\Omega_\phi\rangle}{\partial t} + \frac{B_\theta}{RB^3}\frac{\partial}{\partial\psi}\left\langle\frac{1}{\psi_s}\frac{\partial\phi}{\partial\psi}\frac{\partial\phi}{\partial\theta}\right\rangle = \nu\frac{\partial^2\langle\Omega_\phi\rangle}{\partial\psi^2}\ . \tag{6.57}$$

Since $\mathbf{B}.\nabla\phi \approx 0$, this implies $(\partial\phi/\partial\theta) \approx -q(\partial\phi/\partial\varphi)$. The above equation then resembles eqn. 6.15, except for a geometrical factor, plus a viscous-drag term which balances the Reynolds stress-induced torque in the steady state. An equation of the form 6.57 has also been used in ref. [209] to treat parallel momentum transport.

6.3.1 Normalisation

Incorporating eqn. 6.57 into the new fluid-ITG would benefit from the equation being in the same normalised units (variables in space and time are normalised by the rational surface spacing and electron diamagnetic frequency, respectively). We define new dimensionless variables $\hat{\Omega}_\phi = \Omega_\phi/\omega_{*e}$ and $\hat{t} = t\omega_{*e}$, allowing us to express the first term in eqn. 6.57 as

$$\frac{\partial\langle\Omega_\phi\rangle}{\partial t} = \omega_{*e}^2\frac{\partial\langle\hat{\Omega}_\phi\rangle}{\partial\hat{t}}\ .$$

In tokamak plasmas, the ratio of the ion momentum diffusivity ν to the ion thermal conductivity χ_i (the Prandtl number) is close to unity [210]. Since $\chi_i \sim 1$ m^2/s for ITG turbulence, and further anticipating fine-scale flows, we normalise ν by $\rho_s^2 c_s/r_s$ (an $\mathcal{O}(1)$ factor). Of course in these simulations, the underlying assumption is that the linear fluctuations would drive nonlinear turbulence (not treated in this work), which in turn determines ν and relaxes the flow-profile to influence the linear fluctuation characteristics. Strictly, the 'self-consistent interaction' is described within this scope. Noting $k_\theta\hat{s} = nq'$, $\omega_{*e} = k_\theta\rho_s c_s/L_n$ and $nq'(\psi - \psi_s) = y$ (henceforth, y labels the integer rational surface spacing and not the poloidal angle as was introduced for

the slab coordinate):

$$\nu\frac{\partial^2\langle\Omega_\phi\rangle}{\partial\psi^2} = \left[\frac{\omega_{*e}(nq')^2\rho_s^2c_s}{\psi_s}\right]\hat{\nu}\frac{\partial^2\langle\hat{\Omega}_\phi\rangle}{\partial^2 y} = \omega_{*e}^2\hat{\mu}\frac{\partial^2\langle\hat{\Omega}_\phi\rangle}{\partial^2 y} ,$$

where $\hat{\mu} = \hat{\nu}(k_\theta\rho_s s^2 L_n/\psi_s)$. In normalising the Reynolds stress term, we define the dimensionless potential $\tilde{\phi} = e\phi/T_e$ and note $\rho_s c_s = T_e(eB)^{-1}$. This allows us to write

$$\frac{B_\theta}{RB^3}\frac{\partial}{\partial\psi}\left\langle\frac{1}{\psi_s}\frac{\partial\phi}{\partial\psi}\frac{\partial\phi}{\partial\theta}\right\rangle = \frac{B_\theta}{\psi_s RB}\frac{\partial}{\partial y}\left\langle\frac{\partial\tilde{\phi}}{\partial y}\frac{\partial\tilde{\phi}}{\partial\theta}\right\rangle(nq'\rho_s c_s)^2 = \omega_{*e}^2\hat{\lambda}\frac{\partial}{\partial y}\left\langle\frac{\partial\tilde{\phi}}{\partial y}\frac{\partial\tilde{\phi}}{\partial\theta}\right\rangle ,$$

with $\hat{\lambda} = \hat{s}^2\epsilon_n^2/q$. Gathering all the terms, we arrive at the normalised evolution equation for the toroidal rotation frequency (dropping the hat on Ω_ϕ for convenience):

$$\frac{\partial\langle\Omega_\phi\rangle}{\partial t} + \hat{\lambda}\frac{\partial}{\partial y}\left\langle\frac{\partial\tilde{\phi}}{\partial y}\frac{\partial\tilde{\phi}}{\partial\theta}\right\rangle = \hat{\mu}\frac{\partial^2\langle\Omega_\phi\rangle}{\partial^2 y} . \tag{6.58}$$

6.4 Numerical solution to the coupled problem

To summarise, in order to study the self-consistent interaction between the flow (fluctuation-induced and background) and the global mode structure, the following equations must be simultaneously solved (poloidal average is implicit):

$$\frac{\partial\Omega_\phi}{\partial t} + \hat{\lambda}T_y(\tilde{\phi}) = \hat{\mu}\frac{\partial^2\Omega_\phi}{\partial^2 y} \quad , \tag{6.59}$$

$$\mathcal{L}\left(\frac{\partial}{\partial t} - \mathrm{i}n\Omega_\phi, \frac{\partial}{\partial y}, \frac{\partial}{\partial\theta}, y, \theta\right)\tilde{\phi} = 0 \quad . \tag{6.60}$$

Here $\tilde{\phi} = \sum_m \phi_m(y)\exp(-\mathrm{i}m\theta)$, $\mathcal{L}\tilde{\phi} = 0$ is described by the fluid-ITG equation 4.1, and following ref. [211], we define the intrinsic torque $T_y = \partial_y R_y$, where

$$R_y = \left\langle\frac{\partial\tilde{\phi}^*}{\partial y}\frac{\partial\tilde{\phi}}{\partial\theta} + \frac{\partial\tilde{\phi}}{\partial y}\frac{\partial\tilde{\phi}^*}{\partial\theta}\right\rangle_\theta \tag{6.61}$$

is the poloidally-averaged Reynolds stress. A further simplification is possible by noting

$$\frac{\partial\tilde{\phi}}{\partial y}\frac{\partial\tilde{\phi}^*}{\partial\theta} = \mathrm{i}\sum_m\left(\phi_m^*\frac{\partial\phi_m}{\partial y}m\right) + \mathrm{i}\sum_m\sum_{k\neq m}\left(\phi_k^*\frac{\partial\phi_m}{\partial y}ke^{-\mathrm{i}(m-k)\theta}\right) , \tag{6.62}$$

allowing us to reduce

$$\left\langle\frac{\partial\tilde{\phi}}{\partial y}\frac{\partial\tilde{\phi}^*}{\partial\theta}\right\rangle_\theta = \mathrm{i}\sum_m\left(\phi_m^*\frac{\partial\phi_m}{\partial y}m\right). \tag{6.63}$$

Finally, the Reynolds stress is expressed as

$$\begin{aligned} R_y &= \mathrm{i}\sum_m \left(\phi_m^* \frac{\partial \phi_m}{\partial y} - \phi_m \frac{\partial \phi_m^*}{\partial y}\right) m \\ &= -2\sum_m \mathcal{I}\left(\phi_m^* \frac{\partial \phi_m}{\partial y}\right) m \end{aligned}$$

6.4.1 Parameters

The principal motivation behind the choice of $\hat{\lambda}$ and $\hat{\mu}$ are as follows (other equilibrium parameters, unless stated otherwise, are defined in table 4.3):

(a) It is desirable that the forced diffusion equation 6.59 achieves steady state quickly. This requires a high $\hat{\mu} = 5 \times 10^{-2}$ - this choice is only limited by the numerical time-stepping of our explicit RK4 solver. Note that the long time behaviour of eqn. 6.59 is only dependent upon the ratio $\hat{\lambda}/\hat{\mu}$. Therefore, the absolute value of $\hat{\mu}$ is not as important provided the temporal characteristics are qualitatively described.

(b) The external and self-generated flows should be comparable, and sufficient to influence the GM-IM dynamics. Based on this we set $\hat{\lambda} \sim 1.0 \times 10^{-4}$.

Realistically, of course, $\hat{\lambda}$ is determined by the saturation amplitude of the instability and $\hat{\mu}$ is typically set by the turbulent diffusivity. The former is indeterminate in our linear model for $\tilde{\phi}$ (eqn. 6.60). However, assuming

$$q \sim \hat{\nu} \sim \mathcal{O}(1) \qquad \text{and} \qquad \frac{\psi_s}{R} \sim k_\theta \rho_s \ll 1 \,, \tag{6.64}$$

it is found that $\hat{\lambda}/\hat{\mu} \sim L_n/R$. We take the major radius $R \sim 1$ m. Further, in the core, $L_n \sim 1$ m and $|\tilde{\phi}|^2 \sim 10^{-4}$, whereas $L_n \sim 10^{-2}$ m and $|\tilde{\phi}|^2 \sim 10^{-2}$ at the edge (Table 2.2). In steady state, the ratio of the Reynolds stress and diffusive term is $|\tilde{\phi}|^2\hat{\lambda}/\hat{\mu} \sim 10^{-4}$. Our numerically motivated choice of $\hat{\lambda}/\hat{\mu} = 2 \times 10^{-3}$ is therefore not entirely unreasonable. In these simulations, the linearly growing perturbation is normalised at every time-step ($|\tilde{\phi}|^2 \sim \mathcal{O}(1)$), so as to retain only the effect of the mode structure on the stress-driven flow.

6.5 Stability characteristics of eigenmodes

Normalising the amplitude of the linearly growing mode allows the coupled system to achieve steady state for a $\tilde{\phi}$ structure that does not change with time (cf. eqn. 6.59). This is seen in Fig. 6.3. We now focus on the dynamics of the IM and GM within this coupled system.

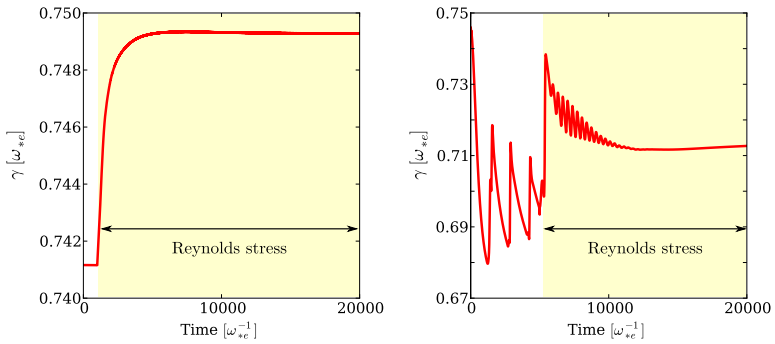

Figure 6.3: (a) shows the evolution of the growth rate of a mode, slightly perturbed from the IM, when the coupled system is solved; the highlighted region indicates the switching on of the Reynolds stress term. (b) shows the corresponding behaviour for the GM.

6.5.1 Perturbed IM

When the simulation is initiated with a background linear flow profile (Fig. 6.4a), which would give a mode structure (Fig. 6.4b) slightly perturbed from the IM, the torque associated with the mode subsequently creates a stationary point in the flow profile, driving the mode back towards the IM (Fig. 6.4d). There is an accompanying increase in the growth rate (Fig. 6.3a) and the overall flow profile is pushed downwards as the flow peaks locally (Fig. 6.4c). Also observe that, while the flow-shear remains unchanged (except locally where the mode sits), the difference between the initial and final flow, on either side of the mode, is asymmetric (Fig. 6.4c).

6.5.2 Perturbed GM

In this case, the initialising background flow (Fig. 6.5a) is such that the mode sets off to perform Floquet cycles (see Fig. 6.3b). The choice of initial mode structure (Fig. 6.5b) is therefore arbitrary. With time of course, the poloidally precessing mode would settle down as a GM (section 5.3.3). Here, instead, as the intrinsic flow is switched on while the mode is performing Floquet cycles, the peak in the flow profile traps the mode, preventing further Floquet oscillations (Fig. 6.3b). The initialisation described here is analogous to starting off with the parameters of section 6.5.1 and increasing the boundary shear. Since the steady state solution to eqn. 6.59 is a straight line, far away from the mode, we impose Neumann boundary conditions. Observe that in this situation, the mode does not balloon at the bottom of the poloidal cross section (Fig. 6.5d). However, as the magnitude of the intrinsic torque is reduced in comparison to the background flow-shear, the mode rotates to settle down at the bottom of the plasma cross-section.

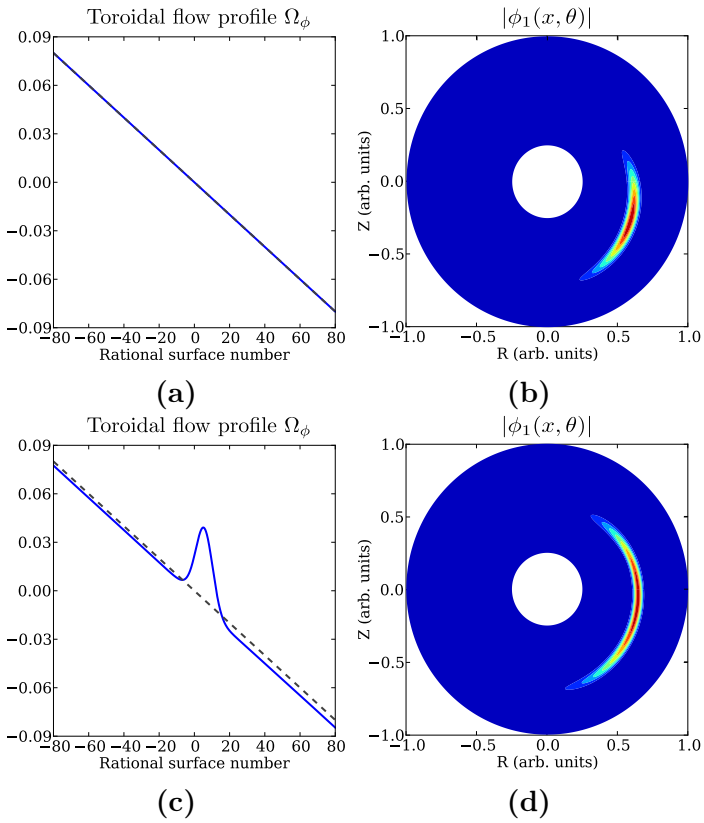

Figure 6.4: (a) shows the initial flow profile (γ_E = −0.001) and (b) the corresponding structure of a mode perturbed about the IM, whereas (c) and (d) show the final states. In (c), the dashed line indicates the initial profile.

6.6 Summary

In this chapter, our fluid-ITG initial-value code has been extended to allow for a feedback of the mode structure on the flow profile. For solutions weakly perturbed from the IM structure, the intrinsic torque creates a stationary point in the flow profile, driving the mode back towards an IM solution. When strong equilibrium flow-shears dominate over the intrinsic flow, the GM solution is possible. Further, the trapping of the eigenmode by the intrinsic flow profile, which would have otherwise undergone $\mathcal{O}(n)$ Floquet rotations in the presence of a high background flow-shear before settling down (section 5.3.3), could reduce the GM formation time. The balance of the intrinsic and external torques ultimately determine the poloidal angle where the global mode balloons. The quantification of these effects, influenced significantly by the saturated mode amplitude, require nonlinear simulations which are beyond the scope of this thesis.

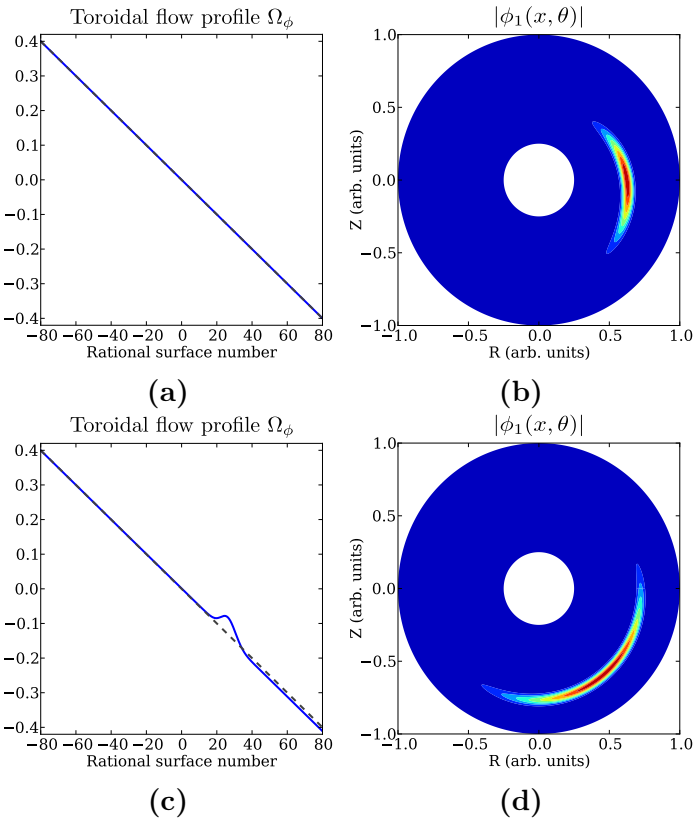

Figure 6.5: (a) and (b) show the flow profile ($\gamma_E = -0.005$) and structure of a mode initialised to perform Floquet precessions. (c) and (d) are the converged states.

Chapter 7

Conclusions and future work

7.1 Conclusions

The success of ITER will help ensure the timely delivery of fusion energy to the power grid, but for this to happen, a range of physics, engineering and materials challenges must be overcome. A key physics challenge is to understand the edge pedestal dynamics, dictated primarily through the balance between MHD stability and turbulent transport. Suppression of edge turbulence improves confinement and raises the edge current and pressure towards the MHD stability limit imposed by the peeling-ballooning (PB) boundary - breaching this makes the tokamak susceptible to damage by energetic edge plasma eruptions. The PB boundary is widely accepted as a robust stability condition on the pedestal, but there remains much less confidence about the edge transport physics.

The ballooning theory is a powerful mathematical framework that can be used to analyse both MHD ballooning and toroidal drift modes (the latter thought to be responsible for turbulence in tokamak plasmas in their nonlinearly saturated states). Central to this theory is the separation between the equilibrium length-scale and spacing of rational flux surfaces (in the vicinity of which such modes are strongly localised). Adjacent flux surfaces are then approximately equivalent, and this allows the simplification of a linearised 2D partial differential equation for fluctuations in radial and poloidal coordinates, to two 1D ordinary differential equations along the magnetic field line (local solution) and radius (providing the global mode envelope).

The formalism predicts two distinct classes for all linear toroidal microinstabilities (e.g. ITG, KBM): the strongly growing but usually inaccessible Isolated Mode (IM), and the relatively benign yet more readily accessible General Mode (GM). Specifically, the IM exists when the maxima in the frequency and growth rate of the radially varying local complex mode frequency coincide. The IM typically peaks at the outboard-midplane, while the GM peaks away from it. Analytic theory and numerical modelling have previously established that the plasma profiles affect the accessibility of these eigenmode branches, with the radially-varying toroidal plasma

flow of particular interest due to a Doppler shift it can introduce in the mode frequency. Indeed, in the presence of a critical radial flow-shear, a transition between the two branches is possible.

This research has involved the development of a new time-dependent code to study the dynamics of the IM and GM for an electrostatic fluid-ITG model. A number of questions were raised in Section 3.6, the answers to which are now summarised.

7.1.1 Eigenmode formation dynamics

When initialised with random noise, the IM is seen to form more rapidly ($\mathcal{O}(300)$ e-foldings) than the GM ($\mathcal{O}(1300)$ e-foldings) (section 5.4.3). Our numerical simulations indicate that, for a peaked ITG drive profile with a background flow-shear, at first, the individual Fourier modes rapidly adjust their amplitudes to establish the IM at the outboard-midplane. Then, the flow-shear causes the phase between the adjacent Fourier modes to change, convecting the radial eigenmode in the poloidal plane to establish the GM at the top/bottom of the plasma. The appearance of Floquet transients for high flow-shears, before their eventual decay into the GM on an $\mathcal{O}(n)$ time-scale, further delays the GM formation time (section 5.3.3).

These time-scales indicate that, at least for our situation, the system is very likely to enter the nonlinear phase before the linear structures can establish. For our fluid-ITG model, the high instability growth rate implies that the radial eigenmodes are strongly driven in the linear phase. Doubling the ITG drive roughly doubles the growth rate, whereas the eigenmode formation time T_{eig} is almost unaffected. Close to marginal stability, this could imply that the factor $\exp(\gamma T_{eig})$ is small. In such a situation, the radial eigenmode may form before the linearly growing Fourier modes (that constitute the radial eigenmode) begin to drive the nonlinear terms. Addressing this topic clearly necessitates a more complete physics model that allows marginally stable situations.

7.1.2 A model for small-ELMs?

Next, with profiles held such that the GM is accessible, the flow-shear is changed to access the more unstable IM. For our parameters, this dynamic can in fact occur at a small-ELM relevant time-scale (Section 5.4). The appearance of Floquet Modes at high flow-shears as the GM tries to establish, and the associated transient bursts in the linear growth rate, could provide an alternative trigger mechanism. Again, nonlinear modelling is needed to correlate these linear triggers with any abrupt increase in transport.

The observation of certain robust features could guide experimental efforts to verify the small-ELM model of section 3.6.2 (provided of course that these global

modes affect the structure of turbulence in the saturated phase). Starting with an initial GM, even when the profiles are varied too rapidly ($\mathrm{d}/\mathrm{d}t \to \infty$), the perturbation structure is seen to remain coherent (Fig. 5.9), with an accompanying strong growth as it passes through the outboard-midplane. Diagnostics that are able to resolve fluctuations over a wide poloidal angle with good temporal resolution, should therefore observe poloidally shifting structures between successive small-ELM bursts.

7.1.3 Towards intrinsic rotation modelling

The global mode structures are themselves expected to generate a torque and modify the equilibrium flow-shear. For a given saturated mode amplitude, in the presence of a weak background shear that moves the IM slightly away from the outboard-midplane, the self-generated torque creates a stationary point in the flow profile and drives the mode back towards the IM again. As the background flow-shear is driven more strongly, due to edge electric fields setting up flows for instance, the intrinsic torque gets dominated and the mode moves away from the outboard-midplane. In summary, our quasi-linear modelling indicates that both the IM and GM can be stable solutions. Again, nonlinear simulations must be performed to quantify these effects for realistic cases.

7.2 Future work

The current investigation presents many new questions, which can only be answered by moving to more accurate gyrokinetic (e.g. [212]) or gyrofluid (e.g. [213]) plasma models. Firstly, it is important to explore these self-consistent dynamics in a realistic situation where profiles are held close to marginal stability (e.g. for the kinetic ballooning mode). Ultimately, nonlinear simulations are needed to test the interaction of turbulence with flows as the GM-IM-GM transition is triggered linearly. These ideas are summarised in Table 7.1 (extensions marked with an asterisk are not necessary for answering the most immediate questions).

While gyrokinetic models are typically much slower to run than gyrofluid models, the latter are unable to accurately describe the dynamics of the $n = 0$ Zonal modes [214]. Zonal flows are large-scale, nonlinearly generated, sheared $E \times B$ flows which play a crucial role in turbulence saturation [101]. These modes are collisionally damped; gyrofluid models on the other hand employ linear collisionless (Landau) rotation damping, which completely suppresses the Zonal mode [214]. A method that captures the benefits of both approaches is one adopted by GryfX [215]. Within this framework, the gyrokinetic code GS2 is used to treat the response of the linear zonal mode, whereas a gyrofluid model is used to evolve all other modes[1] (i.e. the

[1] A spectral representation makes this decomposition trivial for the linear terms.

Table 7.1: Extensions to the present work

Present model	Extension	Motivation
Linear	Nonlinear	To quantify change in transport fluxes associated with the linear GM-IM-GM transition
Fluid	Kinetic	Studying global mode dynamics close to marginal stability
Circular cross-section	*Shaped	Effect on eigenmode structure for scenario optimisation
Electrostatic	*Electromagnetic	Important for high β plasmas

small-scale turbulent structures). One may envisage a similar approach, but using the BOUT++ framework [216] to simulate a gyrofluid model[2], whereas a global GK code (e.g. ORB5 [217, 218]) could be used to capture the Zonal mode. The successful implementation of such a framework could contribute greatly towards addressing some key open questions in fusion research:

(a) There is evidence of shaping influencing the intrinsic toroidal rotation [190]. Could this be mediated by the global mode structures? If such a correlation exists, this could provide a handle on the intrinsic torque profile control, through tailoring the plasma shape and background profiles to influence the global modes (see section 3.6.3).

(b) Can the GM-IM-GM transition in the nonlinear phase allow the profiles to partially collapse and re-build in a cyclic manner? This could be achieved by coupling the fluxes from nonlinear BOUT++ simulations (for example) to a transport code which can evolve the background plasma profiles. This may be an important step in moving towards the first self-consistent small-ELM simulations.

[2]The benefit of this approach is that the modular nature of BOUT++ enables the users to quickly implement and test various physics models.

Appendix A

Flux-surfaces

Begin by considering the divergence of the magnetic field in a cylindrical coordinate system axisymmetric in ϕ (i.e. $\partial/\partial\phi \to 0$):

$$\nabla . B = \frac{1}{R}\frac{\partial (RB_R)}{\partial R} + \frac{\partial B_Z}{\partial z} = 0 \, . \tag{A.1}$$

This is satisfied by the functions $B_R = (1/R)(\partial\psi/\partial Z)$ and $B_Z = (-1/R)(\partial\psi/\partial R)$, where $\psi = \psi(R, Z)$ is a poloidal flux function[1]. Note that $\mathbf{B}.\nabla\psi = 0$, and from the force balance $\mathbf{J} \times \mathbf{B} = \nabla p$, we see that $\mathbf{B}.\nabla p = 0$. This implies that magnetic field lines lie on constant ψ surfaces, which are also surfaces of constant pressure p. Using these definitions of B_R and B_Z, we can write

$$\mathbf{B} = B_\varphi \hat{e}_\varphi + B_R \hat{e}_R + B_Z \hat{e}_Z \tag{A.2}$$

$$= RB_\varphi \nabla\varphi + \frac{1}{R}\frac{\partial\psi}{\partial Z}\hat{e}_R - \frac{1}{R}\frac{\partial\psi}{\partial R}\hat{e}_Z \tag{A.3}$$

$$= \underbrace{RB_\varphi \nabla\varphi}_{\text{Toroidal field}} + \underbrace{\nabla\varphi \times \nabla\psi}_{\text{Poloidal field}} \, . \tag{A.4}$$

We introduce a new flux function f similar to ψ, and define $J_R = (-1/\mu_0 R)(\partial f/\partial Z)$ and $J_Z = (1/\mu_0 R)(\partial f/\partial R)$ to give $\nabla . \mathbf{J} = 0$. Using Ampère's law $\nabla \times \mathbf{B} = \mu_0 \mathbf{J}$, we straightforwardly see that $f(R, Z) = RB_\varphi$. In a tokamak, $B_\varphi \propto 1/R$, implying that the 'toroidal field function' f is typically constant. Next from $\mathbf{J}.\nabla p = 0$ we note $(\nabla f \times \nabla p) . \hat{e}_\varphi = 0$. This condition is satisfied if $f = f(p)$, as then $\nabla f = (\mathrm{d}f/\mathrm{d}p)\nabla p$, implying $RB_\varphi = f(\psi)$.

For completeness, we derive a similar form for the current density by noting $B_\varphi \to J_\varphi$ and $\psi \to -f/\mu_0$. Then

$$\mathbf{J} = RJ_\varphi \nabla\varphi - \frac{1}{\mu_0}\frac{\mathrm{d}f}{\mathrm{d}\psi}\nabla\varphi \times \nabla\psi \, , \tag{A.5}$$

$$\mathbf{B} = f(\psi)\nabla\varphi + \nabla\varphi \times \nabla\psi \, . \tag{A.6}$$

[1] $B_p^2 = B_R^2 + B_Z^2 = |\nabla\psi|^2/R^2$, so ψ describes the poloidal field B_p.

Then using the force balance equation, we can relate the current, field and pressure as

$$J_\varphi = -R\frac{\mathrm{d}p}{\mathrm{d}\psi} - \frac{f}{\mu_0 R}\frac{\mathrm{d}f}{\mathrm{d}\psi} \,. \tag{A.7}$$

Eliminating J_φ using Ampère's law gives the Grad-Shafranov equation for ψ:

$$R\frac{\partial}{\partial R}\left(\frac{1}{R}\frac{\partial \psi}{\partial R}\right) + \frac{\partial^2 \psi}{\partial Z^2} = -\mu_0 R^2 \frac{\mathrm{d}p}{\mathrm{d}\psi} - f\frac{\mathrm{d}f}{\mathrm{d}\psi} \,. \tag{A.8}$$

The Grad-Shafranov equation can be solved iteratively upon specifying the boundary conditions on $p(\psi)$ and $f(\psi)$. Its solution, equilibrium ψ surfaces, form a set of nested tori (Fig. 2.5a).

Appendix B

Mathematical tools

B.1 Hermite polynomials

Differential equations of the form

$$\frac{\mathrm{d}^2y}{\mathrm{d}x^2} - 2x\frac{\mathrm{d}y}{\mathrm{d}x} + 2ny = 0 \tag{B.1}$$

are solved by Hermite polynomials of order n, $H_n(x)$. Now consider $\phi = \mathrm{e}^{-\mu x^2} H_n(x)$. It is then possible to write

$$\begin{aligned} H_n(x) &= \mathrm{e}^{\mu x^2}\phi\,, \quad H_n'(x) = \mathrm{e}^{\mu x^2}\left[\phi' + 2\mu x\phi\right]\,, \\ H_n''(x) &= \mathrm{e}^{\mu x^2}\left[\phi'' + 4\mu x\phi' + (4\mu^2x^2 + 2\mu)\phi\right]\,. \end{aligned}$$

Substituting the above set of equations into B.1, we derive

$$\left[\phi'' + \phi'(4\mu x - 2x) + \phi(4\mu^2x^2 + 2\mu - 4\mu x^2 + 2n)\right]\mathrm{e}^{\mu x^2} = 0\,. \tag{B.2}$$

Noting that $\exp(\mu x^2) \neq 0$ and setting $\mu = 1/2$:

$$\phi'' + \left[(2n+1) - x^2\right]\phi = 0 \quad . \tag{B.3}$$

Therefore, equations of the form B.3 are solved by the polynomials

$$\phi(x) = \mathrm{e}^{-x^2/2} H_n(x)\,. \tag{B.4}$$

B.2 Dirac comb

The Dirac-comb or the Shah function is defined as

$$\text{Ш}(x) = \sum_{k=-\infty}^{+\infty} \delta(x-k)\,, \tag{B.5}$$

where $\delta(x)$ is the Dirac-delta function and k defines integers. If $g(x)$ is a continuous function, $g(x).\text{Ш}(x)$ has the property of sampling $g(x)$ at integer values. If instead we wish to sample with a period $T = 2\pi$, the Shah function may be suitably modified:

$$\text{Ш}(x) = \sum_{k=-\infty}^{+\infty} \delta(x - 2\pi k) \, . \tag{B.6}$$

Now any function $f(x)$, with a periodicity 2π, may be Fourier expanded as

$$f(x) = \sum_{m=-\infty}^{+\infty} c_m \mathrm{e}^{\mathrm{i}mx} \, , \tag{B.7}$$

where

$$c_m = \frac{1}{2\pi} \int_{-\pi}^{\pi} f(x) \mathrm{e}^{-\mathrm{i}mx} \, \mathrm{d}x \, . \tag{B.8}$$

With $f(x) = \text{Ш}(x)$, we have

$$\begin{aligned} c_m &= \frac{1}{2\pi} \int_{-\pi}^{\pi} \left(\sum_{k=-\infty}^{+\infty} \delta(x - 2\pi k) \right) \mathrm{e}^{-\mathrm{i}mx} \, \mathrm{d}x \\ &= \frac{1}{2\pi} \sum_{k=-\infty}^{+\infty} \int_{-\pi}^{\pi} \delta(x - 2\pi k) \mathrm{e}^{-\mathrm{i}mx} \, \mathrm{d}x \\ &= \frac{1}{2\pi} \sum_{k=-\infty}^{+\infty} \int_{-\pi-2\pi k}^{\pi-2\pi k} \delta(t) \mathrm{e}^{-\mathrm{i}mt} \mathrm{e}^{-\mathrm{i}m2\pi k} \, \mathrm{d}t \, ; \end{aligned}$$

where we have used the coordinate transform $x - 2\pi k = t$. Observe that $\forall k \neq 0$, the integration domain excludes the point $t = 0$. Properties of the Dirac-delta function reduce the above equation to $c_m = (2\pi)^{-1}$. This yields the useful form:

$$2\pi \sum_{k=-\infty}^{+\infty} \delta(x - 2\pi k) = \sum_{m=-\infty}^{+\infty} \mathrm{e}^{\mathrm{i}mx} \, . \tag{B.9}$$

Appendix C

Numerically solving second order ODE

We begin by discretising a second order ordinary differential equation (ODE)

$$a(x)\frac{\mathrm{d}^2 f}{\mathrm{d}x^2} + b(x)\frac{\mathrm{d}f}{\mathrm{d}x} + c(x)f = d(x) \tag{C.1}$$

at a grid point i as

$$a_i\left(\frac{f_{i+1} - 2f_i + f_{i-1}}{h^2}\right) + b_i\left(\frac{f_{i+1} - f_{i-1}}{2h}\right) + c_i f_i = d_i \ . \tag{C.2}$$

This can be rewritten in the form

$$A_i f_{i-1} + B_i f_i + C_i f_{i+1} = d_i \ , \tag{C.3}$$

where

$$A_i = \left(\frac{a_i}{h^2} - \frac{b_i}{2h}\right) \qquad B_i = \left(\frac{-2a_i}{h^2} + c_i\right) \qquad C_i = \left(\frac{a_i}{h^2} + \frac{b_i}{2h}\right) \ . \tag{C.4}$$

Note than A_1 and C_N are not defined for the first and last grid points respectively. With x discretised into N grid points, the ODE represented by eqn. C.3 can be cast into the $N \times N$ tridiagonal matrix form:

$$\begin{bmatrix} B_1 & C_1 & 0 & \cdots & 0 \\ A_2 & B_2 & C_2 & \cdots & 0 \\ \vdots & \vdots & \ddots & \ddots & \vdots \\ 0 & 0 & \cdots & A_N & B_N \end{bmatrix} \begin{bmatrix} f_1 \\ f_2 \\ \vdots \\ f_N \end{bmatrix} = \begin{bmatrix} d_1 \\ d_2 \\ \vdots \\ d_N \end{bmatrix} \ . \tag{C.5}$$

Next we specify the boundary conditions. A Dirichlet (fixed value) boundary is specified on f_1 by noting

$$B_1 f_1 + C_1 f_2 = d_1 \ , \tag{C.6}$$

which upon setting $B_1 = 1$ and $C_1 = 0$ allows us to specify $f_1 = d_1$. We can similarly impose a Neumann (fixed gradient) boundary condition by setting $C_1 = 1/h$ and $B_1 = -1/h$ such that

$$\frac{f_2 - f_1}{h} = d_1 \ . \tag{C.7}$$

It is important to note that, in specifying the boundary gradients, an $\mathcal{O}(h)$ finite-difference scheme would only allow the solution $f(x_i)$ to be accurate to $\mathcal{O}(h)$. Matrix equations of the form $\mathrm{M}f = \mathrm{D}$, given by C.5, are efficiently solved for f with the help of routines available in LAPACK [219], or using other methods described in ref. [220].

Bibliography

[1] A. Bokshi et al. Response of toroidal drift modes to profile evolution: a small-ELM model? http://ocs.ciemat.es/EPS2015PAP/pdf/P2.192.pdf, 2015. [Online; accessed 09-Sep-2016].

[2] A. Bokshi et al. The self-consistent response of linear microinstabilities to profile evolution. http://ocs.ciemat.es/EPS2016PAP/pdf/P2.043.pdf, 2016. [Online; accessed 09-Sep-2016].

[3] A Bokshi et al. The response of toroidal drift modes to profile evolution: a model for small-ELMs in tokamak plasmas? *Plasma Physics and Controlled Fusion*, 58(7):075011, 2016.

[4] International Energy Agency. World Energy Outlook 2014: Executive Summary. https://www.iea.org/publications/freepublications/publication/WEO_2014_ES_English_WEB.pdf, 2014. [Online; accessed 09-May-2016].

[5] U.S. Energy Information Administration. Frequently asked questions. https://www.eia.gov/tools/faqs/faq.cfm?id=73&t=11, 2015. [Online; accessed 09-June-2016].

[6] British Petroleum. BP Energy Outlook 2035. http://www.bp.com/content/dam/bp/pdf/energy-economics/energy-outlook-2015/bp-energy-outlook-2035-booklet.pdf, 2015. [Online; accessed 10-May-2016].

[7] S Cornot-Gandolphe. LNG cost reductions and flexibility in LNG trade add to security of gas supply. *IEA (2005): Energy Prices and Taxes, Quarterly Statistics. First Quarter*, 2005.

[8] World Resources Institute. The Carbon Budget. http://www.wri.org/ipcc-infographics. [Online; accessed 10-May-2016].

[9] CO_2.Earth. Global Carbon Emissions. https://www.co2.earth/global-co2-emissions?itemid=1, 2016. [Online; accessed 10-May-2016].

[10] NASA Goddard Institute for Space Studies. Surface Temperatures. http://data.giss.nasa.gov/gistemp/graphs_v3/Fig.A2.txt. [Online; accessed 08-May-2016].

[11] NASA Goddard Institute for Space Studies. Greenhouse Gases. http://data.giss.nasa.gov/modelforce/ghgases/Fig1A.ext.txt. [Online; accessed 08-May-2016].

[12] M Huber and R Knutti. Anthropogenic and natural warming inferred from changes in earth's energy balance. *Nature Geoscience*, 5(1):31–36, 2012.

[13] U.S. National Climate Assessment. Cause of Climate Change. http://nca2014.globalchange.gov/highlights/overview/overview, 2014. [Online; accessed 11-May-2016].

[14] U.S. Environmental Protection Agency. Overview of Greenhouse Gases. https://www3.epa.gov/climatechange/ghgemissions/gases.html, 2014. [Online; accessed 11-May-2016].

[15] Brian Wang. Deaths per TWH by energy source. http://www.nextbigfuture.com/2011/03/deaths-per-twh-by-energy-source.html, 2011. [Online; accessed 19-Feb-2017].

[16] United Nations. Chernobyl: The True Scale of the Accident. http://www.un.org/press/en/2005/dev2539.doc.htm, 2005. [Online; accessed 11-May-2016].

[17] World Health Organization. Household air pollution and health. http://www.who.int/mediacentre/factsheets/fs292/en/, 2016. [Online; accessed 11-May-2016].

[18] M Brauer et al. Ambient air pollution exposure estimation for the global burden of disease 2013. *Environmental Science & Technology*, 50(1):79–88, 2016.

[19] M H Forouzanfar et al. Global, regional, and national comparative risk assessment of 79 behavioural, environmental and occupational, and metabolic risks or clusters of risks in 188 countries, 1990-2013: a systematic analysis for the global burden of disease study 2013. *The Lancet*, 386(10010):2287 – 2323, 2015.

[20] R A Silva et al. Global premature mortality due to anthropogenic outdoor air pollution and the contribution of past climate change. *Environmental Research Letters*, 8(3):034005, 2013.

[21] Kerry Emanuel and Dennis Whyte. The climate problem: Solutions and opportunities. Private communication, 2016.

[22] Renee Cho. Is Biomass Really Renewable? http://blogs.ei.columbia.edu/2011/08/18/is-biomass-really-renewable/, 2011. [Online; accessed 12-May-2016].

[23] Chris Llewellyn Smith. Meeting future energy demand. Frontiers of Fusion Workshop, 2013.

[24] IAEA Division of Public Information. Fast reactors provide sustainable nuclear power for "thousands of years". https://www.iaea.org/newscenter/news/fast-reactors-provide-sustainable-nuclear-power-thousands-years, 2013. [Online; accessed 19-Feb-2017].

[25] U.S. Energy Information Administration. Annual Energy Review. http://www.eia.gov/totalenergy/data/annual/showtext.cfm?t=ptb0902, 2012. [Online; accessed 08-May-2016].

[26] Greenpeace. Chernobyl death toll grossly underestimated. http://www.greenpeace.org/international/en/news/features/chernobyl-deaths-180406/, 2006. [Online; accessed 10-June-2016].

[27] C Norman and D Dickson. The aftermath of chernobyl. *Science*, 233:1141–1143, 1986.

[28] Crystal Lombardo. Nuclear Fission Advantages and Disadvantages List. http://thenextgalaxy.com/nuclear-fission-advantages-and-disadvantages-list/. [Online; accessed 13-May-2016].

[29] S D Sagan. The causes of nuclear weapons proliferation. *Annual Review of Political Science*, 14:225–244, 2011.

[30] International Atomic Energy Agency. IAEA incident and trafficking database (ITDB). http://www-ns.iaea.org/downloads/security/itdb-fact-sheet.pdf, 2016. [Online; accessed 03-Aug-2016].

[31] International Atomic Energy Agency. Technological challenges to safe disposal of radioactive waste. https://www.iaea.org/newscenter/news/technological-challenges-safe-disposal-radioactive-waste, 2012. [Online; accessed 03-Aug-2016].

[32] World Nuclear Association. Radioactive Waste Management. http://www.world-nuclear.org/information-library/nuclear-fuel-cycle/nuclear-wastes/radioactive-waste-management.aspx, 2015. [Online; accessed 12-May-2016].

[33] Ipsos MORI. Strong global opposition towards nuclear power. https://www.ipsos-mori.com/researchpublications/researcharchive/2817/, 2011. [Online; accessed 10-June-2016].

[34] M Piera. Sustainability issues in the development of nuclear fission energy. *Energy Conversion and Management*, 51(5):938 – 946, 2010.

[35] John Wesson. *Tokamaks*. Oxford University Press, Oxford, UK, 2011.

[36] Tom Murphy. Nuclear Fusion. http://physics.ucsd.edu/do-the-math/2012/01/nuclear-fusion/, 2012. [Online; accessed 16-May-2016].

[37] USGS Mineral Resources Program. Lithium - For Harnessing Renewable Energy. http://pubs.usgs.gov/fs/2014/3035/, 2014. [Online; accessed 16-May-2016].

[38] Culham Centre for Fusion Energy. Introduction to Fusion. http://www.ccfe.ac.uk/introduction.aspx. [Online; accessed 16-May-2016].

[39] S J Zinkle. Advanced materials for fusion technology. *Fusion Engineering and Design*, 74:31 – 40, 2005.

[40] A Glaser and R J Goldston. Proliferation risks of magnetic fusion energy: clandestine production, covert production and breakout. *Nuclear Fusion*, 52(4):043004, 2012.

[41] Energy consumption and GDP in developing countries: A cointegrated panel analysis. *Energy Economics*, 27(3):415 – 427, 2005.

[42] J D Lindl et al. Progress toward ignition and burn propagation in inertial confinement fusion. *Physics Today*, 45(9):32, 1992.

[43] J Lindl. Development of the indirect-drive approach to inertial confinement fusion and the target physics basis for ignition and gain. *Physics of Plasmas*, 2(11):3933–4024, 1995.

[44] O A Hurricane et al. Fuel gain exceeding unity in an inertially confined fusion implosion. *Nature*, 506(7488):343, 2014.

[45] Howard Wilson. Particle orbits and drifts. Plasma Physics for Fusion Lectures, University of York, 2011.

[46] R Aymar et al. The ITER design. *Plasma Physics and Controlled Fusion*, 44(5):519, 2002.

[47] EUROfusion. Figures database. http://figures.euro-fusion.org/.

[48] M Kruskal and M Schwarzschild. Some instabilities of a completely ionized plasma. *Proceedings of the Royal Society of London A: Mathematical, Physical and Engineering Sciences*, 223(1154):348–360, 1954.

[49] V D Shafranov. The stability of a cylindrical gaseous conductor in a magnetic field. *The Soviet Journal of Atomic Energy*, 1(5):709–713, 1956.

[50] S von Goeler et al. Studies of internal disruptions and $m = 1$ oscillations in tokamak discharges with soft—X-Ray techniques. *Phys. Rev. Lett.*, 33:1201–1203, 1974.

[51] G H Miley A A Harms, K F Schoepf and D R Kingdon. *Principles of Fusion Energy*. World Scientific, Singapore, 2008.

[52] Swiss Plasma Center. TCV tokamak. `http://spc.epfl.ch/research_TCV_Tokamak`, 2012. [Online; accessed 30-June-2016].

[53] F Hofmann et al. Creation and control of variably shaped plasmas in TCV. *Plasma Physics and Controlled Fusion*, 36(12B):B277, 1994.

[54] T Ozeki et al. Plasma shaping, edge ballooning stability and ELM behaviour in DIII-D. *Nuclear Fusion*, 30(8):1425, 1990.

[55] F Piras et al. Snowflake divertor plasmas on TCV. *Plasma Physics and Controlled Fusion*, 51(5):055009, 2009.

[56] N J Fisch. Theory of current drive in plasmas. *Rev. Mod. Phys.*, 59:175–234, Jan 1987.

[57] P Helander et al. Stellarator and tokamak plasmas: a comparison. *Plasma Physics and Controlled Fusion*, 54(12):124009, 2012.

[58] M Greenwald et al. A new look at density limits in tokamaks. *Nuclear Fusion*, 28(12):2199, 1988.

[59] M Greenwald. Density limits in toroidal plasmas. *Plasma Physics and Controlled Fusion*, 44(8):R27, 2002.

[60] M Keilhacker et al. High fusion performance from deuterium-tritium plasmas in JET. *Nuclear Fusion*, 39(2):209, 1999.

[61] Y Koide and JT-60 Team. Progress in confinement and stability with plasma shape and profile control for steady-state operation in the japan atomic energy research institute tokamak-60 upgrade. *Physics of Plasmas*, 4(5):1623–1631, 1997.

[62] Steve Cowley. Hot fusion. `http://physicsworld.com/cws/article/print/2010/oct/01/hot-fusion`, 2010. [Online; accessed 18-May-2016].

[63] Dennis Whyte. Magnetic fusion reactor design and the role of technology. Frontiers of Fusion Workshop, 2016.

[64] S Yoon et al. 26 t 35 mm all-gdba$_2$cu$_3$o$_{7-x}$ multi-width no-insulation superconducting magnet. *Superconductor Science and Technology*, 29(4):04LT04, 2016.

[65] B N Sorbom et al. ARC: A compact, high-field, fusion nuclear science facility and demonstration power plant with demountable magnets. *Fusion Engineering and Design*, 100:378 – 405, 2015.

[66] ITER Newsline 86. How Fritz Wagner "discovered" the H-Mode. `https://www.iter.org/newsline/86/659`, 2009. [Online; accessed 17-May-2016].

[67] Francis F Chen. *Introduction to Plasma Physics and Controlled Fusion*. Springer, New York, USA, 2008.

[68] Raghuveer Parthasarathy. Diffusion and brownian motion. `http://pages.uoregon.edu/raghu/TeachingFiles/Winter07Phys352/Notes_Diffusion.pdf`, 2008. [Online; accessed 11-July-2016].

[69] Benjamin Dudson. Magnetic confinement fusion. Lectures, University of York, 2012.

[70] G R Tynan et al. A review of experimental drift turbulence studies. *Plasma Physics and Controlled Fusion*, 51(11):113001, 2009.

[71] David Dickinson. PhD Thesis. University of York, 2012.

[72] B D Scott. Tokamak edge turbulence: background theory and computation. *Plasma Physics and Controlled Fusion*, 49(7):S25, 2007.

[73] C M Surko. *Turbulence and Anomalous Transport in Magnetised Plasmas; p93.* Cargese Workshop, edited by D. Gresillon and M. Dubois, 1986.

[74] G F Matthews. Tokamak plasma diagnosis by electrical probes. *Plasma Physics and Controlled Fusion*, 36(10):1595, 1994.

[75] D C Robinson and K McGuire. Magnetic islands and disruptions in the tosca tokamak. *Nuclear Fusion*, 19(1):115, 1979.

[76] P M Schoch et al. Heavy-ion beam probe diagnostic systems (invited). *Review of Scientific Instruments*, 59(8):1646–1651, 1988.

[77] T S Green and G A Proca. A parallel plate electrostatic spectrograph. *Review of Scientific Instruments*, 41(10):1409–1414, 1970.

[78] R P Seraydarian et al. Multichordal visible/near-uv spectroscopy on the DIII-D tokamak. *Review of Scientific Instruments*, 59(8):1530–1532, 1988.

[79] R J Fonck et al. Plasma fluctuation measurements in tokamaks using beam-plasma interactions. *Review of Scientific Instruments*, 61(11):3487–3495, 1990.

[80] H Park et al. Multimixer far-infrared laser thomson scattering apparatus. *Review of Scientific Instruments*, 53(10):1535–1540, 1982.

[81] S Sattler and H J Hartfuss. Intensity interferometry for measurement of electron temperature fluctuations in fusion plasmas. *Plasma Physics and Controlled Fusion*, 35(9):1285, 1993.

[82] S J Freethy et al. Measurement of turbulent electron temperature fluctuations on the asdex upgrade tokamak using correlated electron cyclotron emission. *Review of Scientific Instruments*, 87(11):11E102, 2016.

[83] T Lehner et al. Linear mode conversion by magnetic fluctuations in inhomogeneous magnetized plasmas. *EPL (Europhysics Letters)*, 8(8):759, 1989.

[84] T Lehecka et al. Reflectometry systems for the DIII-D tokamak. *Review of Scientific Instruments*, 59(8):1620–1622, 1988.

[85] A J Wootton et al. Fluctuations and anomalous transport in tokamaks. *Physics of Fluids B*, 2(12):2879–2903, 1990.

[86] J W Connor. Tokamak turbulence-electrostatic or magnetic? *Plasma Physics and Controlled Fusion*, 35(SB):B293, 1993.

[87] D L Brower et al. Multichannel scattering studies of the spectra and spatial distribution of tokamak microturbulence. *Phys. Rev. Lett.*, 54:689–692, Feb 1985.

[88] L Colas et al. Internal magnetic fluctuations and electron heat transport in the tore supra tokamak: Observation by cross-polarization scattering. *Nuclear Fusion*, 38(6):903, 1998.

[89] V J Simcic et al. Internal magnetic and electrostatic fluctuation measurements of magnetohydrodynamic modes in the texas experimental tokamak (TEXT). *Physics of Fluids B*, 5(5):1576–1580, 1993.

[90] E J Doyle et al. *Plasma Physics and Controlled Nuclear Fusion Research*, Vol. I:235, IAEA Vienna, 1993.

[91] J Candy and R E Waltz. Anomalous transport scaling in the DIII-D tokamak matched by supercomputer simulation. *Phys. Rev. Lett.*, 91:045001, Jul 2003.

[92] E J Doyle et al. Chapter 2: Plasma confinement and transport. *Nuclear Fusion*, 47(6):S18, 2007.

[93] K Itoh et al. *Transport and Structural Formation in Plasmas*. IOP Publishing, Bristol, UK, 1999.

[94] I Shesterikov et al. Direct evidence of eddy breaking and tilting by edge sheared flows observed in the TEXTOR tokamak. *Nuclear Fusion*, 52(4):042004, 2012.

[95] J W Connor and H R Wilson. Survey of theories of anomalous transport. *Plasma Physics and Controlled Fusion*, 36(5):719, 1994.

[96] G M Staebler. Theory of internal and edge transport barriers. *Plasma Physics and Controlled Fusion*, 40(5):569, 1998.

[97] C M Greenfield et al. Transport and performance in DIII-D discharges with weak or negative central magnetic shear. *Physics of Plasmas*, 4(5):1596–1604, 1997.

[98] L L Lao et al. Rotational and magnetic shear stabilization of magnetohydrodynamic modes and turbulence in DIII-D high performance discharges. *Physics of Plasmas*, 3(5):1951–1958, 1996.

[99] Z Lin et al. Turbulent transport reduction by zonal flows: Massively parallel simulations. 281(5384):1835–1837, 1998.

[100] A M Dimits et al. Comparisons and physics basis of tokamak transport models and turbulence simulations. *Physics of Plasmas*, 7(3):969–983, 2000.

[101] P H Diamond et al. Zonal flows in plasma - a review. *Plasma Physics and Controlled Fusion*, 47(5):R35, 2005.

[102] B B Kadomtsev and O P Pogutse. Trapped particles in toroidal magnetic systems. *Nuclear Fusion*, 11(1):67, 1971.

[103] G Rewoldt et al. Microinstability properties of small-aspect-ratio tokamaks. *Physics of Plasmas*, 3(5):1667–1672, 1996.

[104] M A Beer et al. Gyrofluid simulations of turbulence suppression in reversed-shear experiments on the tokamak fusion test reactor. *Physics of Plasmas*, 4(5):1792–1799, 1997.

[105] T M Antonsen et al. Physical mechanism of enhanced stability from negative shear in tokamaks: Implications for edge transport and the L-H transition. *Physics of Plasmas*, 3(6):2221–2223, 1996.

[106] F Jenko et al. Critical gradient formula for toroidal electron temperature gradient modes. *Physics of Plasmas*, 8(9):4096–4104, 2001.

[107] F Jenko et al. Electron temperature gradient driven turbulence. *Physics of Plasmas*, 7(5):1904–1910, 2000.

[108] W Dorland et al. Electron temperature gradient turbulence. *Phys. Rev. Lett.*, 85:5579–5582, Dec 2000.

[109] F Jenko and W Dorland. Prediction of significant tokamak turbulence at electron gyroradius scales. *Phys. Rev. Lett.*, 89:225001, Nov 2002.

[110] J D Callen. Drift-wave turbulence effects on magnetic structure and plasma transport in tokamaks. *Phys. Rev. Lett.*, 39:1540–1543, Dec 1977.

[111] D Dickinson et al. Kinetic instabilities that limit β in the edge of a tokamak plasma: A picture of an H-mode pedestal. *Phys. Rev. Lett.*, 108:135002, 2012.

[112] W M Tang et al. Kinetic-ballooning-mode theory in general geometry. *Nuclear Fusion*, 20(11):1439, 1980.

[113] P B Snyder et al. A first-principles predictive model of the pedestal height and width: development, testing and iter optimization with the EPED model. *Nuclear Fusion*, 51(10):103016, 2011.

[114] H Biglari and L Chen. Unified theory of resonant excitation of kinetic ballooning modes by energetic ions and alpha particles in tokamaks. *Phys. Rev. Lett.*, 67:3681–3684, Dec 1991.

[115] W M Tang et al. Finite-gyroradius stabilization of ballooning modes in a toroidal geometry. *Nuclear Fusion*, 21(7):891, 1981.

[116] P B Snyder and G W Hammett. Electromagnetic effects on plasma microturbulence and transport. *Physics of Plasmas*, 8(3):744–749, 2001.

[117] J Candy. Beta scaling of transport in microturbulence simulations. *Physics of Plasmas*, 12(7), 2005.

[118] E A Belli and J Candy. Fully electromagnetic gyrokinetic eigenmode analysis of high-beta shaped plasmas. *Physics of Plasmas*, 17(11), 2010.

[119] H Biglari et al. Toroidal ion-pressure-gradient-driven drift instabilities and transport revisited. *Physics of Fluids B*, 1(1):109–118, 1989.

[120] F Romanelli. Ion temperature-gradient-driven modes and anomalous ion transport in tokamaks. *Physics of Fluids B*, 1(5):1018–1025, 1989.

[121] P Mantica et al. Experimental study of the ion critical-gradient length and stiffness level and the impact of rotation in the JET tokamak. *Phys. Rev. Lett.*, 102:175002, 2009.

[122] W Suttrop et al. Identification of plasma-edge-related operational regime boundaries and the effect of edge instability on confinement in ASDEX upgrade. *Plasma Physics and Controlled Fusion*, 39(12):2051, 1997.

[123] K H Burrell. Effects of E×B velocity shear and magnetic shear on turbulence and transport in magnetic confinement devices. *Physics of Plasmas*, 4(5):1499–1518, 1997.

[124] E J Synakowski et al. Local transport barrier formation and relaxation in reverse-shear plasmas on the tokamak fusion test reactor. *Physics of Plasmas*, 4(5):1736–1744, 1997.

[125] R J Goldston. Energy confinement scaling in tokamaks: some implications of recent experiments with ohmic and strong auxiliary heating. *Plasma Physics and Controlled Fusion*, 26(1A):87, 1984.

[126] ITER Physics Expert Group on Confinement, Transport, ITER Physics Expert Group on Confinement Modelling, Database, and ITER Physics Basis Editors. Chapter 2: Plasma confinement and transport. *Nuclear Fusion*, 39(12):2175, 1999.

[127] M Sugihara et al. Examinations on various scalings for the H-mode edge pedestal width. *Plasma Physics and Controlled Fusion*, 44(5A):A299, 2002.

[128] R J Groebner. An emerging understanding of h-mode discharges in tokamaks. *Physics of Fluids B*, 5(7):2343–2354, 1993.

[129] P B Snyder et al. ELMs and constraints on the H-mode pedestal: peeling-ballooning stability calculation and comparison with experiment. *Nuclear Fusion*, 44(2):320, 2004.

[130] J W Connor et al. A review of internal transport barrier physics for steady-state operation of tokamaks. *Nuclear Fusion*, 44(4):R1, 2004.

[131] Y Sakamoto and the JT-60 Team. Enhanced performance and control issues in JT-60U long pulse discharges. *Plasma Physics and Controlled Fusion*, 47(12B):B337, 2005.

[132] J W Connor et al. Magnetohydrodynamic stability of tokamak edge plasmas. *Physics of Plasmas*, 5(7):2687–2700, 1998.

[133] H R Wilson and S C Cowley. Theory for explosive ideal magnetohydrodynamic instabilities in plasmas. *Phys. Rev. Lett.*, 92:175006, Apr 2004.

[134] A Kirk et al. Evolution of filament structures during edge-localized modes in the MAST tokamak. *Phys. Rev. Lett.*, 96:185001, May 2006.

[135] EUROfusion. ELMs - friend or foe? `https://www.euro-fusion.org/2013/08/elms/`, 2013. [Online; accessed 19-Aug-2016].

[136] G Federici et al. Assessment of erosion of the ITER divertor targets during type I ELMs. *Plasma Physics and Controlled Fusion*, 45(9):1523, 2003.

[137] N Oyama et al. Pedestal conditions for small ELM regimes in tokamaks. *Plasma Physics and Controlled Fusion*, 48(5A):A171, 2006.

[138] A Kirk et al. Effect of resonant magnetic perturbations on low collisionality discharges in MAST and a comparison with ASDEX upgrade. *Nuclear Fusion*, 55(4):043011, 2015.

[139] T E Evans et al. Suppression of large edge localized modes with edge resonant magnetic fields in high confinement DIII-D plasmas. *Nuclear Fusion*, 45(7):595, 2005.

[140] O Schmitz et al. Aspects of three dimensional transport for ELM control experiments in ITER-similar shape plasmas at low collisionality in DIII-D. *Plasma Physics and Controlled Fusion*, 50(12):124029, 2008.

[141] C J Ham et al. Non-axisymmetric ideal equilibrium and stability of ITER plasmas with rotating RMPs. *Nuclear Fusion*, 56(8):086005, 2016.

[142] P T Lang et al. ELM pace making and mitigation by pellet injection in ASDEX upgrade. *Nuclear Fusion*, 44(5):665, 2004.

[143] P T Lang et al. ELM control strategies and tools: status and potential for ITER. *Nuclear Fusion*, 53(4):043004, 2013.

[144] N Oyama. Progress and issues in understanding the physics of ELM dynamics, ELM mitigation, and ELM control. *Journal of Physics: Conference Series*, 123(1):012002, 2008.

[145] H R Wilson et al. Magneto-hydrodynamic stability of the H-mode transport barrier as a model for edge localized modes: an overview. *Plasma Physics and Controlled Fusion*, 48(5A):A71, 2006.

[146] W Suttrop. The physics of large and small edge localized modes. *Plasma Physics and Controlled Fusion*, 42(5A):A1, 2000.

[147] K H Burrell et al. Quiescent H-mode plasmas in the DIII-D tokamak. *Plasma Physics and Controlled Fusion*, 44(5A):A253, 2002.

[148] P B Snyder et al. Stability and dynamics of the edge pedestal in the low collisionality regime: physics mechanisms for steady-state ELM-free operation. *Nuclear Fusion*, 47(8):961.

[149] ITER. ITPA PEP topical group. `http://www.iter.org/org/team/fst/itpa/pep`. [Online; accessed 19-Aug-2016].

[150] Ö D Gürcan et al. A simple model of intrinsic rotation in high confinement regime tokamak plasmas. *Physics of Plasmas*, 17(3), 2010.

[151] J E Rice et al. Observations of anomalous momentum transport in Alcator C-Mod plasmas with no momentum input. *Nuclear Fusion*, 44(3):379, 2004.

[152] K Ida et al. Spontaneous toroidal rotation driven by the off-diagonal term of momentum and heat transport in the plasma with the ion internal transport barrier in LHD. *Nuclear Fusion*, 50(6):064007, 2010.

[153] J E Rice et al. Edge temperature gradient as intrinsic rotation drive in Alcator C-Mod tokamak plasmas. *Phys. Rev. Lett.*, 106:215001, May 2011.

[154] J E Rice et al. Observations of impurity toroidal rotation suppression with ITB formation in ICRF and ohmic H mode Alcator C-Mod plasmas. *Nuclear Fusion*, 41(3):277, 2001.

[155] J E Rice et al. Inter-machine comparison of intrinsic toroidal rotation in tokamaks. *Nuclear Fusion*, 47(11):1618, 2007.

[156] G R McKee et al. Dependence of the L- to H-mode power threshold on toroidal rotation and the link to edge turbulence dynamics. *Nuclear Fusion*, 49(11):115016, 2009.

[157] F L Waelbroeck. Gyroscopic stabilization of the internal kink mode. *Physics of Plasmas*, 3(3):1047–1053, 1996.

[158] A M Garofalo et al. Sustained stabilization of the resistive-wall mode by plasma rotation in the DIII-D tokamak. *Phys. Rev. Lett.*, 89:235001, Nov 2002.

[159] F D Halpern et al. Predictive simulations of ITER including neutral beam driven toroidal rotation. *Physics of Plasmas*, 15(6), 2008.

[160] P H Diamond et al. Physics of non-diffusive turbulent transport of momentum and the origins of spontaneous rotation in tokamaks. *Nuclear Fusion*, 49(4):045002, 2009.

[161] P H Diamond et al. An overview of intrinsic torque and momentum transport bifurcations in toroidal plasmas. *Nuclear Fusion*, 53(10):104019, 2013.

[162] Y Kosuga et al. On the efficiency of intrinsic rotation generation in tokamaks. *Physics of Plasmas*, 17(10), 2010.

[163] S Ku et al. Physics of intrinsic rotation in flux-driven itg turbulence. *Nuclear Fusion*, 52(6):063013, 2012.

[164] W X Wang et al. Trapped electron mode turbulence driven intrinsic rotation in tokamak plasmas. *Phys. Rev. Lett.*, 106:085001, Feb 2011.

[165] W X Wang et al. Characteristics of turbulence-driven plasma flow and origin of experimental empirical scalings of intrinsic rotation. *Physics of Plasmas*, 18(4), 2011.

[166] W M Solomon et al. Momentum confinement at low torque. *Plasma Physics and Controlled Fusion*, 49(12B):B313, 2007.

[167] Y J Shi et al. ECH effects on toroidal rotation: KSTAR experiments, intrinsic torque modelling and gyrokinetic stability analyses. *Nuclear Fusion*, 53(11):113031, 2013.

[168] Y J Shi et al. Toroidal rotation profile structure in KSTAR L-mode plasmas with mixed heating by NBI and ECH. *Nuclear Fusion*, 56(1):016014, 2016.

[169] R J Buttery et al. The influence of rotation on the β_n threshold for the 2/1 neoclassical tearing mode in DIII-D. *Physics of Plasmas*, 15(5), 2008.

[170] ITER. ITPA transport and confinement topical group. `http://www.iter.org/org/team/fst/itpa/tc`. [Online; accessed 21-Aug-2016].

[171] R J Groebner et al. Improved understanding of physics processes in pedestal structure, leading to improved predictive capability for ITER. *Nuclear Fusion*, 53(9):093024, 2013.

[172] J W Connor et al. High mode number stability of an axisymmetric toroidal plasma. *Proceedings of the Royal Society of London A: Mathematical, Physical and Engineering Sciences*, 365(1720):1–17, 1979.

[173] P B Snyder et al. Edge localized modes and the pedestal: A model based on coupled peeling-ballooning modes. *Physics of Plasmas*, 9(5):2037–2043, 2002.

[174] Mitsuru Kikuchi. *Frontiers in Fusion Research*. Springer, London, UK, 2011.

[175] J W Connor et al. Shear damping of drift waves in toroidal plasmas. *Phys. Rev. Lett.*, 70:1803–1805, Mar 1993.

[176] J B Taylor et al. Structure and damping of toroidal drift waves (and their implications for anomalous transport). *Plasma Phys. Control. Fusion*, 35(8):1063, 1993.

[177] R L Dewar. Spectrum of the ballooning schrödinger equation. *Plasma Physics and Controlled Fusion*, 39(3):453, 1997.

[178] D Dickinson et al. Structure of micro-instabilities in tokamak plasmas: Stiff transport or plasma eruptions? *Physics of Plasmas*, 21(1):010702, 2014.

[179] F L Waelbroeck and L Chen. Ballooning instabilities in tokamaks with sheared toroidal flows. *Physics of Fluids B*, 3(3):601–610, 1991.

[180] R L Miller et al. Stabilization of ballooning modes with sheared toroidal rotation. *Physics of Plasmas*, 2(10):3676–3684, 1995.

[181] P A Abdoul et al. Using a local gyrokinetic code to study global ITG modes in tokamaks. *Plasma Phys. Control. Fusion*, 57:065004, 2015.

[182] N Oyama et al. Energy loss for grassy ELMs and effects of plasma rotation on the ELM characteristics in JT-60U. *Nuclear Fusion*, 45(8):871, 2005.

[183] L L Lao et al. Dependence of edge stability on plasma shape and local pressure gradients in the DIII-D and JT-60U tokamaks. *Nuclear Fusion*, 41(3):295, 2001.

[184] P H Diamond and Y B Kim. Theory of mean poloidal flow generation by turbulence. *Physics of Fluids B*, 3(7):1626–1633, 1991.

[185] A B Hassam and J F Drake. Spontaneous poloidal spin-up of tokamak plasmas: Reduced equations, physical mechanism, and sonic regimes. *Physics of Fluids B*, 5(11):4022–4029, 1993.

[186] A B Hassam and R M Kulsrud. Time evolution of mass flows in a collisional tokamak. *Physics of Fluids*, 21(12):2271–2279, 1978.

[187] A B Hassam and T M Antonsen. Poloidal spin-up of tokamak plasmas from poloidal asymmetry of particle and momentum sources. *Physics of Plasmas*, 1(2):337–344, 1994.

[188] Y Z Zhang and S M Mahajan. Reynolds stress of localized toroidal modes. *Physics of Plasmas*, 2(11):4236–4245, 1995.

[189] Y Camenen et al. Consequences of profile shearing on toroidal momentum transport. *Nuclear Fusion*, 51(7):073039, 2011.

[190] B P Duval et al. Bulk plasma rotation in the TCV tokamak in the absence of external momentum input. *Plasma Physics and Controlled Fusion*, 49(12B):B195, 2007.

[191] J W Connor and J B Taylor. Ballooning modes or fourier modes in a toroidal plasma? *Physics of Fluids*, 30(10):3180–3185, 1987.

[192] J B Taylor et al. Structure of short-wavelength drift modes and transport in a toroidal plasma. *Plasma Physics and Controlled Fusion*, 38(2):243, 1996.

[193] P W Terry et al. Radial fluctuation scale of ion temperature gradient driven turbulence. *Physics of Fluids*, 31(10):2920–2927, 1988.

[194] P W Terry. Suppression of turbulence and transport by sheared flow. *Rev. Mod. Phys.*, 72:109–165, 2000.

[195] R E Waltz et al. Theory and simulation of rotational shear stabilization of turbulence. *Physics of Plasmas*, 5(5):1784–1792, 1998.

[196] C M Roach et al. Gyrokinetic simulations of spherical tokamaks. *Plasma Physics and Controlled Fusion*, 51(12):124020, 2009.

[197] J W Connor and T J Martin. Rotation shear and drift wave stability. *Plasma Phys. Control. Fusion*, 49(9):1497, 2007.

[198] Arkaprava Bokshi. Initial-value fluid-ITG code. `http://dx.doi.org/10.15124/b3b40ad0-152a-4b04-90e5-3460e7d5a487`, 2016. [Created 18-May-2016].

[199] H R Wilson et al. The effect of flow on ideal magnetohydrodynamic ballooning instabilities: a tutorial. *Rotation and Momentum Transport in Magnetized Plasmas*, 2:137, 2014.

[200] F Romanelli and F Zonca. The radial structure of the ion-temperature-gradient-driven mode. *Physics of Fluids B: Plasma Physics*, 5(11):4081–4089, 1993.

[201] Jonathan Skipp. MSc Thesis. University of York, 2012.

[202] Y Z Zhang and S M Mahajan. On broken ballooning symmetry. *Physics Letters A*, 157(2):133 – 136, 1991.

[203] P Hill et al. Perpendicular wavenumber dependence of the linear stability of global ion temperature gradient modes on E x B flows. *Plasma Phys. Control. Fusion*, 54(6):065011, 2012.

[204] W A Cooper. Ballooning instabilities in tokamaks with sheared toroidal flows. *Plasma Physics and Controlled Fusion*, 30(13):1805, 1988.

[205] J B Taylor and H R Wilson. Plasma rotation and toroidal drift modes. *Plasma Phys. Control. Fusion*, 38:1999, 1996.

[206] J Q Dong et al. Momentum-energy transport from turbulence driven by parallel flow shear. *Physics of Plasmas*, 1(10):3250–3261, 1994.

[207] B Coppi. Accretion theory of 'spontaneous' rotation in toroidal plasmas. *Nuclear Fusion*, 42(1):1, 2002.

[208] A G Peeters et al. Toroidal momentum pinch velocity due to the coriolis drift effect on small scale instabilities in a toroidal plasma. *Phys. Rev. Lett.*, 98:265003, 2007.

[209] Ö D Gürcan et al. Intrinsic rotation and electric field shear. *Physics of Plasmas*, 14(4), 2007.

[210] M Barnes et al. Turbulent transport in tokamak plasmas with rotational shear. *Phys. Rev. Lett.*, 106:175004, Apr 2011.

[211] H R Wilson et al. Influence of the plasma edge on tokamak performance. *Nuclear Fusion*, 40(3Y):713, 2000.

[212] T S Hahm et al. Fully electromagnetic nonlinear gyrokinetic equations for tokamak edge turbulence. *Physics of Plasmas*, 16(2), 2009.

[213] B D Scott. Free-energy conservation in local gyrofluid models. *Physics of Plasmas*, 12(10), 2005.

[214] M N Rosenbluth and F L Hinton. Poloidal flow driven by ion-temperature-gradient turbulence in tokamaks. *Phys. Rev. Lett.*, 80:724–727, Jan 1998.

[215] N Mandell and W Dorland. Hybrid Gyrokinetic / Gyrofluid Simulation of ITG Turbulence. http://adsabs.harvard.edu/abs/2014APS..DPPCP8039M, October 2014.

[216] B D Dudson et al. BOUT++: A framework for parallel plasma fluid simulations. *Computer Physics Communications*, 180(9):1467 – 1480, 2009.

[217] S Jolliet et al. A global collisionless PIC code in magnetic coordinates. *Computer Physics Communications*, 177(5):409 – 425, 2007.

[218] T Görler et al. Intercode comparison of gyrokinetic global electromagnetic modes. *Physics of Plasmas*, 23(7), 2016.

[219] E Anderson et al. *LAPACK Users' Guide*. Society for Industrial and Applied Mathematics, Philadelphia, PA, third edition, 1999.

[220] Benjamin Dudson. Computational techniques in plasma physics. Computational Lab, University of York, 2012.